Order Number 9218266

Mode interaction models in near-wall turbulence

Sanghi, Sanjeev, Ph.D.

City University of New York, 1992

U·M·I
300 N. Zeeb Rd.
Ann Arbor, MI 48106

MODE INTERACTION MODELS IN NEAR-WALL TURBULENCE

by

SANJEEV SANGHI

A dissertation submitted to the Graduate Faculty in
Engineering in partial fulfillment of the
requirements for the degree of Doctor of Philosophy,
The City University of New York.

1992

This manuscript has been read and accepted for the Graduate Faculty in Engineering in satisfaction of the dissertation requirement for the degree of Doctor of Philosophy.

11/6/91
Date

Nadine Aubry
Chair of Examining Committee

11/6/91
Date

Gerard J. Iooss
Executive Officer

Professor Andreas Acrivos

Professor Yiannis Andreopoulos

Professor Stephen Cowin

Supervisory Committee

The City University of New York

Abstract

MODE INTERACTION MODELS IN NEAR-WALL TURBULENCE

by

Sanjeev Sanghi

Adviser: Professor Nadine Aubry

The dynamics of near wall turbulence is characterized by intermittent bursts during which fine scale turbulence is produced. Bursting events have been observed in low dimensional dynamical models built from empirical eigenfunctions of the proper orthogonal decomposition (POD). Severely truncated models, which did not account for streamwise variations in an explicit way, have been derived and studied by Aubry *et al.* (1988). In the present work, the persistency of intermittent behavior in higher dimensional models is investigated. First, the new truncations account for streamwise variations. Intermittent behavior persists in ***all*** the models, but exhibits additional complexities. In particular, the non zero streamwise modes become excited during the bursts so that the infinitely long streamwise rolls burst in the streamwise direction into smaller scales. In all cases, intermittency seems to be due to homoclinic cycles connecting hyperbolic fixed points or complicated limit sets. The triggering of the higher order streamwise modes by nonlinear interactions is also analyzed. The influence of another proper orthogonal mode (i.e. smaller structures in the normal direction) is also investigated: bursts still occur in the same way, the second mode participating along with the first. A coherent structure study is

performed in these models in order to connect the findings of this investigation to those of the other researchers. Most experimentally observed structures, i.e. streaks, streamwise rolls, horseshoe vortical structures and shear layers, are clearly identified and it is proposed that they are a part of the same structure.

The POD technique is used to expand the vorticity field into 'coherent vortical structures'. To calculate the POD modes for any vector, its autocorrelation tensor is needed. It is, however, shown in this work that the POD modes and eigenvalues of the vorticity vector can be calculated from the POD modes and the eigenvalues of the velocity vector. This method is applied to the turbulent wall layer and the spectrum of eigenvalues of the vorticity modes is compared with the velocity modes. As expected, the peak shifts towards the right for the vorticity spectrum. As a trial case the first two vortical structures are evaluated for one realization.

Finally a dynamic eddy viscosity model based on the application of the approximate inertial manifold technique to the POD modes is proposed.

Dedicated

to

Krishna Gopal Vyasji Maharaj,

Swami Chinmayananda,

Shri Mataji Nirmala Devi,

and

my parents

Acknowledgements

I am grateful to my mentor Professor Nadine Aubry, for introducing me to this problem and helping me to develop my research skills, and to the other members of my advisory committee: Professors Andreas Acrivos, Yiannis Andreopoulos and Stephen Cowin. In particular I would like to acknowledge the supportive role of Professor Acrivos, who is also the director of the Levich Institute, the place where this research was conducted. I would also like to thank Professor George Karniadakis (Princeton University) for acting as the external examiner for the final examination of this dissertation. Thanks are also due to Professors John Lumley and Zellman Warhaft (Cornell University) and Professors Sanjay Dhande and Vijay Kumar Garg (Indian Institute of Technology, Kanpur) for their support, advice and encouragement.

I am indebted to my parents, brother and sister whose love, guidance and encouragement have played a major role in all my achievements. I would like to express my sincere gratitude to all my teachers and would like to mention some excellent teachers I have come across: Mr. Dinesh Kumar Joshi (St. Xavier School, Jaipur), Professors Santosh Kumar Gupta, Vijay Gupta and Vijay Kumar Garg, (Indian Institute of Technology, Kanpur), Professor S. B. Pope (Cornell University, Ithaca) and Professors Andreas Acrivos and David Rumschitzki (City College, New York).

I would like to thank my friends: Devdatt, Rakesh, Samir and Shyam (from Cornell) and Anurag, Bir, Cao, Fan, Kai, Kate, Lian and Said (from the Levich Institute).

Special thanks are due to Mary and Tammy for providing a pleasant atmosphere (and making lots of good coffee!) at the Institute.

This work was partially supported by the Petroleum Research Fund (Grant No. ACS-PRF 23009-G7), National Science Foundation (Grant No. CTS-8957462) and PSC-City University of New York (Grant Nos. 661356, 662308 and 669317). Computer resources were provided by the City University of New York, University Computer Center.

Contents

List of Tables

List of Figures

Chapter 1

Introduction

Despite the contribution of many researchers the mechanism of turbulence production in the boundary layer flows is still poorly understood. It is, however, well established that the production is concentrated in the regions very near to the wall. Thus, the knowledge of the turbulence structure in this region is of key importance.

The wall region of the turbulent boundary layer has generally been divided into three zones - the viscous sublayer, the buffer layer and the log region. The zone adjacent to the wall, where the flow is directly affected by the latter, is termed as the viscous sublayer. In the older literature this has been referred to as the laminar sublayer. This name is, however, misleading because unsteady, three dimensional velocity fluctuations are present there. The relevant flow scales in this layer, the friction velocity, u_τ, the kinematic viscosity, ν, and others derived from these two, are termed as the wall or inner variables. The mean velocity in this layer varies linearly with the distance from the wall. The log region is the zone where viscosity no longer dominates the flow. The only relevant length scale in this layer is the normal distance from the wall and the mean velocity is a logarithmic function of this quantity. The transition region in between the viscous sublayer and the log region is referred to as the buffer layer. The peak production and dissipation of turbulent energy occur approximately in the middle of this region. The approximate dimensions of these zones (in terms of wall variables) are as follows. The viscous sublayer extends from

the wall to 5 units, the buffer layer from 5 to 30 units and the log region from 30 to 100 units.

The first person to report the presence of large scale structures in pipe flows was Reynolds (1883) who visualized the flow by injecting a dye in the center of the pipe. He was able to observe the instantaneous picture of the flow by viewing it in the light of an electric spark. He described the flow as "...a mass of more or less distinct curls, showing eddies ". However, most of the studies in the first few decades of this century stressed on the statistical theories of turbulence and neglected the importance of the coherent structures in the turbulent flows. In the 1950s researchers in the field started to realize that the turbulent boundary layers consisted of patterns of organized structures which played an important part in the turbulence production (Townsend 1956). Theodorsen (1952) proposed a model for the instantaneous description of the near-wall turbulence dynamics in which he suggested the formation of hairpin shaped vortical structures with heads inclined at 45 degrees. Streamwise streaks were first revealed by the experiment of Hama (Corrsin 1957). A series of flow visualization experiments, in which the major focus was on the buffer layer and the viscous sublayer, carried out by Kline and co-workers (Runstadler *et al.*1963, Kline *et al.* 1967, Kim *et al.*1971) and by Corino and Brodkey (1969) fully established the importance of organized structures in the turbulence production. Along with the visualization experiments, methods were also being developed to measure the flow quantities close to the wall. The techniques used in the measurement experiments included the hot wire probes (to measure flow velocities) and the electrochemical method (to determine wall shear stress: Mitchell and Hanratty 1966). Around this time, Lumley (1967) introduced the proper orthogonal decomposition (POD), a tool known to the people working in the probability theory (Loeve, 1955), to the turbulence community with the objective of giving a physical definition of a large eddy. Since this technique required detailed input data (autocorrelation tensor for the velocity field), it had to await the results of the detailed experiments and numerical simulations to establish itself. In the early 1970s

inexpensive digital computers became easily available and this led to, in Robinson's (1991) terms, the conditional sampling era. The conditional sampling methods consist of statistical techniques designed to obtain the average structure that satisfies a prescribed condition, usually at a given point. One of the first methods which became very popular was the quadrant splitting; the plane formed by u_1 and u_2 (the streamwise and normal velocity fluctuations) was split in four parts depending on their signs (Wallace *et al.* 1972 and Lu and Willmarth 1973). Another widely used tool was the VITA (variable interval time averaging) technique of Blackwelder and Kaplan (1976). Blackwelder and Eckelmann (1979) used the conditional sampling analysis to deduce the presence of organized structures - pairs of counter-rotating streamwise vortices- in the wall region of bounded turbulent shear flow. The major difficulty with these methods is the ad-hoc nature of the prescribed condition. With the increase in the capabilities of the computer, direct numerical simulations (DNS) started gaining popularity in the 1980s. The objective of these simulations is to solve the three dimensional, time dependent Navier-Stokes equations to compute the evolution of the significant scales of motion without using any turbulence models. These methods have been used to evaluate the flow field in the boundary layer (Moin and Kim 1982, Spalart 1988) and highly detailed data have been generated. The complexity of the data, however, has made their interpretation extremely difficult in terms of the coherent structures and their dynamics. Thus, there is a need for simplified numerical simulations and models.

In spite of the fact that a large number of studies have been conducted on the organized structures, there is no consensus on the definition and role of the coherent structures. The state of research in this area has been described similar to the well-known story of blind men trying to describe an elephant (Bridges *et al.* 1990, George 1989). Loosely speaking, the coherent structures have been defined as large-scale organized motions in a flow.

One of the most detailed studies of the coherent motions in the turbulent boundary layer is that of Robinson *et al.* (1989) who analyzed the numerical data of Spalart (1988). They classify eight types of structures, which include the low speed streaks near the wall, the ejections of low-speed fluid away from the wall, the sweeps of high-speed fluid towards the wall, the vortical structures and the near-wall shear layers. They suggest some relationships among these structures. However, an analysis of their instabilities is rather absent there because they are not well described by the numerical simulations. Streak formation as an instability mechanism is the object of many investigations (for example Jang *et al.* 1986) and is not the primary goal of this investigation, although the relationship between the various structures in this work strongly suggests such a mechanism. Instead, the focus of this study is on the streak breaking or 'secondary instability' and the streak reformation as a cyclic sequence of events. It has been postulated that the streak breaking is generated by an inflectional instability of the streamwise velocity profile observed in the visualization experiments (Kline *et al.* 1967) and the numerical data (Moin and Kim 1982). Jimenez *et al.* (1988) proposed a mechanism based on the ejection of the shear layer (spanwise vorticity) in two-dimensional flows.

Amidst the variety of definitions and techniques of detecting the coherent structures, the POD method posed by Lumley provides an attractive definition of these structures and a statistical method for their extraction from the turbulent flow fields. The method consists of extracting structures from the velocity fluctuations by calculating the eigenvalues and eigenfunctions of its two point correlation tensor. The dominant eddy is defined as the eigenfunction with the largest eigenvalue. Thus, one tries to optimally represent a random field by a set of deterministic functions which are determined by the field itself. The representation is optimal in the sense that the functions are extracted so that the most possible energy is contained in the dominant eddy, and the most possible of the remaining energy in the next one, and so on. This definition of the coherent structures (optimal representation of the field) is clearly different from the taxonomy of structures (streaks,

sweeps, vortices etc.) of Kline and Robinson (1989) and Robinson (1991), in which each type of structure is classified on the basis of a few aspects of the observed coherent motions.

As stated earlier, most of the work using POD started about twenty years after Lumley first proposed it, because the complete two point correlation in at least one direction of the probe separation is required. For this, one needs to take simultaneous measurements at many locations using multi-point probes. Two experimental programs, designed with the aim of applying the decomposition to the flow, were completed in the mid 1980s. In the first of these, Herzog (1986) carried out the measurements in the near-wall region of the turbulent pipe flow with glycerine as the working fluid. The measurements were obtained at 882 point pairs, using the hot-film anemometery. The second experiment was carried out by Glauser (1987) in the mixing layer of an axisymmetric air jet. The streamwise and radial components of the velocity vector were measured on a grid with 7 points across the layer and 25 azimuthal positions. With the advent of the numerical simulations, researchers started to calculate the POD from the numerical data. Moin (1984) used the correlation tensor obtained from the LES (large eddy simulation) data of the turbulent channel flow. Later, Moin and Moser (1989) used the DNS results to calculate the eigenfunctions in the channel flow.

It is appropriate to mention here that with the generation of the numerical simulation data, the POD has become quite a popular tool to study different types of flows. Sirovich and co-workers at Brown University have studied Rayleigh Benard convection (Sirovich *et al.* 1987, Sirovich and Park 1990) and Ginzburg-Landau equations (Sirovich and Rodriguez 1987) using this method. The other flows for which this tool has been used include the periodically forced mixing layer (Glezer *et al.* 1989), Burgers equation (Chambers *et al.* 1988), grooved channels and circular cylinders (Deane *et al.* 1991), and Kuramoto-Sivashinsky equation (Aubry and Lian 1991, Kirby and Armbruster 1991).

The main difficulty in the application of the POD to the experimental data was that in the absence of data at many points in time, one could obtain only the spatial eigenfunctions. Using these, the contribution of each structure to the second order statistical quantities can be calculated but the instantaneous evolution and dynamics of the structures cannot be followed. This problem was resolved by the work of Aubry *et al.* (1988) who derived a set of ten ordinary differential equations (ODEs) by taking a Galerkin projection of the Navier-Stokes equations onto the eigenfunctions obtained by Herzog (1986). The set of ODEs represents a dynamical system which traces the time evolution of the spatial eigenfunctions. Thus, this method is a bridge between the Navier-Stokes equations and the dynamical systems theory. The point worth noting is that the building blocks of this bridge are the coherent structures obtained by the POD. The eigenfunctions used by Aubry *et al.* (1988) represent infinitely long streamwise rolls close to a wall. These rolls exhibit intermittency whose nature is clearly identified: it is due to the presence of a heteroclinic cycle connecting hyperbolic fixed points. The solution spends a relatively long time near a fixed point where it stays quasi-steady, oscillates in a growing oscillatory motion and suddenly bursts through a brief jump along a heteroclinic orbit to another fixed point (only translated in the cross-stream direction). In physical space, the streamwise rolls, quiescent for a long time, start to oscillate, suddenly burst into other structures in the cross-stream direction and get reformed. This strongly intermittent dynamics repeats itself an infinite number of times. It thus explains the "bursting event" as a cycle, i.e. the secondary instability mechanism as well as the roll reformation. The influence of noise of any kind has been clearly identified: it triggers the eruption event earlier and the time between two events, which otherwise keeps increasing, reaches an equilibrium. Stone and Holmes (1989) have shown that the presence of noise is responsible for the exponential tails in the distributions of violent events due to saddle-saddle connections. Exponential tails have, indeed, been experimentally observed for the distribution of the bursting events (Kim *et al.* 1971 and Bogard and Tiederman 1986).

The intermittent solutions are a direct consequence of the symmetries of the equation. There has been a great deal of work on the system of equations which show homoclinic and heteroclinic connections. Nicolaenko *et al.* (1985, 1986) have reported the presence of such behavior in the numerical solutions of the Kuramoto-Sivashinsky equation with free periodic boundary conditions. A bursting mechanism based on the SO(2) $\times$ D_k-equivariant cycles in the two-dimensional Kolmogrov flows has been proposed by Nicolaenko and She (1990). Leibovich and Mahalov (1990) show the numerical evidence of the heteroclinic connections in several SO(2)-equivariant systems modelling the wave interactions among the invariant subspaces of the Navier-Stokes equations in the circular and plane geometries with implications for the transition in the pipe flows and the boundary layers. Mullin and Darbyshire (1990) demonstrate the presence of heteroclinic and homoclinic cycles in an SO(2)-equivariant, Taylor-Couette apparatus with rotating endplates. In a recent work, Champneys (1991) shows the existence of homoclinic orbits in the dynamics of the articulated pipes conveying fluid. These are only a few of the works which indicate the presence of these intermittent mechanisms and the list is by no means complete. The point being made here is that these connections, where one finds periods of relative calm with few excited modes interrupted by irregular storms of activity involving more spatial modes, may represent the intermittent turbulence production events and instability mechanisms.

In a review of the approach taken in Aubry *et al.* (1988), a paradox, regarding the existence of fixed point solutions in a flow with no streamwise variations, has been pointed out by Moffatt (1990). This question is addressed briefly in chapter 3 and the reader is referred to Berkooz *et al.* (1991) and Berkooz (1991) for a detailed analysis. Finally, Moffatt concludes: 'Aubry *et al.* (1988) provides a valuable starting point, and the computations and analysis initiated by these authors now need to be further developed and extended'. This thesis is a step in this direction.

Perhaps, the most important issue of Aubry *et al.*'s model is the robustness of the proposed intermittency mechanism to the order of the truncation. One knows that in many cases the behavior of a finite or low dimensional dynamical system is a consequence of the low order of the truncation. For example, an extension of the three dimensional Lorenz model was first derived (Curry 1978) in which the two-dimensional Boussinesq equations were projected on a 14-variable subspace. Later, it became clear that as the order of the truncation increases from three to the full Boussinesq system, the degree of chaos increases at first and suddenly decreases (Curry *et al.* 1984). At high resolution, no strong chaos is observed. This is a typical example in which the qualitative dynamics is a product of the inadequate spatial resolution. It is thus imperative to check that the kind of intermittency displayed by the 10D model for the wall region of the turbulent boundary layer and described above survives as more streamwise and normal modes are included. In a certain sense this is also the point raised by Moffatt (1990).

Another issue which is focussed upon in this work is the relationship between the different types of coherent structures which have been observed in the near-wall region of the boundary layer. The results of the simulations are used to detect and identify these patterns (streaks, ejections, streamwise vortices, horseshoe vortices and shear layers) and to find the relationships between them.

In most of the works, where the POD modes have been applied, the structures have been derived such that they maximize the energy i.e. the random vector field which is expanded in terms of the POD modes is the velocity vector. The expansion of vorticity into the POD modes, so that the resulting structures would maximize enstrophy (rather than energy), is also investigated. The motivation behind such an expansion is that vorticity is considered to be an important quantity in turbulence. In fact, the presence of three dimensional vorticity fluctuations is considered to be a characteristic of the turbulent flows and the coherent vortical structures are believed to play an important role in their dynamics (Hussain 1986). From the generating equation of the POD modes it follows that the

autocorrelation matrix of the vorticity field is needed to obtain the vortical structures. It is shown that given the POD modes which maximize the energy, the optimal modes which maximize the enstrophy can be derived, thus avoiding the need for the autocorrelation matrix of vorticity. The method is illustrated by studying the vortical POD structures in the near wall region of the turbulent boundary layer.

This thesis is organized as follows. In chapter 2, the POD and its application to the turbulent boundary layer are reviewed. The derivation of a truncated set of the ordinary differential equations from the Navier-Stokes equations and the results from the 10D model of Aubry *et al.* (1988) are recalled. The shortcomings of the 10D model and the necessity of adding the non-zero streamwise modes are also discussed. The properties of the set of ODEs (which includes an arbitrary number of modes in any direction) are discussed in chapter 3. The set of equations is analyzed in terms of the invariant subspaces and their relation to the physical symmetries of the flow. In chapter 4 the results of the numerical computations of the systems including one and two non-zero streamwise modes and two eigenmodes are presented. The robustness of the intermittency of the 10D model is verified and a new type of intermittency is reported. It is also shown that the streamwise modes with higher wavenumbers get activated by the modes with lower wavenumbers because of the nonlinear interactions. In chapter 5, the physical structures are extracted from the flow fields and compared with those presented by other researchers. A criterion for evaluating the eddy viscosity parameter is also presented. In chapter 6, the POD is applied to the vorticity vector. It is shown that the POD data from the velocity fluctuations is sufficient to carry out this operation. The coherent structures are defined in terms of the POD based on the vorticity expansion. The results from the computations of chapter 4 are used to compute the vortical structures at one instant of time. A dynamic eddy viscosity model based on the approximate inertial manifolds technique is developed in chapter 7. Finally, in chapter 8 the conclusions are presented.

Chapter 2

Background Review

In this chapter the proper orthogonal decomposition (Lumley 1967) and its application to the wall region of the turbulent boundary layer are reviewed. The derivation of a set of ordinary differential equations, by taking a Galerkin projection of the POD modes on the Navier-Stokes equations, is recalled from Aubry *et al.* (1988) and Aubry (1987), and the results obtained in these works are analyzed. Finally, the deficiencies which arise because of the severity of the truncations in these preliminary models are discussed.

2.1. The Proper Orthogonal Decomposition

As stated in Chapter 1, the POD was introduced to the turbulence community by Lumley (1967) to identify the coherent structures in a random flow. Given an ensemble of realizations of an inhomogeneous, energy integrable vector field, u_i, the method consists of projecting it onto a candidate structure, ϕ_i. The projection, γ, is defined by

$$\gamma = \frac{(\phi_i, u_i)}{\sqrt{(\phi_j, \phi_j)}}, \tag{2.1}$$

where the inner product operating on two vector fields, a_i and b_i, is defined by $(a_i,b_i) = \int a_i(x)b_i^*(x)\,dx$. The structure, ϕ_i, is chosen to be the one which is best correlated to all the elements of the ensemble of the random field, namely that which maximizes $<|\gamma|^2>$ (< > represents the ensemble average). The calculus of variations reduces this maximization problem to a Fredholm integral equation of the first kind:

$$\int \langle u_i(x)u_j(x')\rangle \phi_j(x')dx' = \lambda\phi_i(x). \tag{2.2}$$

Hilbert-Schmidt theory gives the following properties of this integral equation. There is a discrete set of eigenfunctions, $\phi_i^{(n)}$, satisfying (2.2). These form a complete orthogonal set which can be normalized such that

$$\int \phi_i^{(m)}(x)\phi_i^{(n)*}(x)dx = \delta_{mn}. \tag{2.3}$$

The random vector field can be reconstructed as

$$u_i(x) = \sum a^{(n)}\phi_i^{(n)}(x). \tag{2.4}$$

The coefficients in (2.4) are uncorrelated:

$$\langle a^{(m)}a^{(n)}\rangle = \lambda^{(n)}\delta_{mn}, \tag{2.5}$$

and are related to the vector field by the expression:

$$a^{(n)} = \int u_i(x)\phi_i^{(n)*}(x)dx. \tag{2.6}$$

The "kinetic energy", E, contained in the signal is given by the sum of the eigenvalues,

$$E = \int \langle u_i(x) u_i(x) \rangle dx = \sum \lambda^{(n)}. \tag{2.7}$$

Thus, every structure makes a finite contribution to E. The expansion is optimal in the sense that at any level of truncation these modes provide the maximum E.

This decomposition is for a general inhomogeneous flow field. If the random field is homogeneous in any direction, the spectrum of eigenvalues becomes continuous and the eigenfunctions become Fourier modes, so that the POD reduces to a harmonic decomposition in these directions.

The shear flow of the wall region is three dimensional, homogeneous in the streamwise (x_1) and spanwise (x_3) directions, stationary in time and inhomogeneous and energy integrable in the normal direction (x_2). Thus, the velocity field is expanded in the Fourier modes in the two spatial homogeneous directions (assuming periodic boundary conditions in x_1 and x_3) and the POD modes in the normal direction. This leads to a box of size $L_1 \times L_3$ with doubly periodic boundary conditions. L_1 and L_3 are determined from the first non-zero wavenumbers in the streamwise and spanwise directions respectively. The information in time is carried by the coefficients $a^{(n)}$ of the expansion. The velocity field fluctuation is expressed in the following way:

$$u_i(x_1, x_2, x_3, t) = \frac{1}{\sqrt{L_1 L_3}} \sum_{lkn} a_k^{(n)}(t) e^{2\pi i(lx_1 + kx_3)} \phi_{i_k}^{(n)}(x_2), \tag{2.8}$$

where l, k are the streamwise and spanwise wavenumbers and $\mathbf{k}$ the vector (l, k) and a 'structure' is defined as:

$$u_i^{(n)}(x_1,x_2,x_3,t) = \frac{1}{\sqrt{L_1L_3}} \sum_{lk} a_k^{(n)}(t) e^{2\pi i(lx_1+kx_3)} \phi_{i_k}^{(n)}(x_2). \qquad (2.8a)$$

The eigenfunctions are extracted from the equation:

$$\int \Phi_{ij_k}(x_2,x_2') \, \phi_{j_k}^{(n)}(x_2') \, dx_2' = \lambda_k^{(n)} \, \phi_{i_k}^{(n)}(x_2), \qquad (2.9)$$

where Φ_{ij} denotes the Fourier transform of the autocorrelation tensor in the x_1, x_3 directions at zero time lag: $R_{ij}(x_1-x'_1, x_2, x'_2, x_3-x'_3)_{t-t'=0}$ and is related to the Fourier transform of the velocity fluctuations, $\hat{u}_{i_k}$, by the following relation:

$$\Phi_{ij_k}(x_2,x_2') = \frac{1}{L_1L_3} \left\langle \hat{u}_{i_k}(x_2) \hat{u}_{j_k}^*(x_2') \right\rangle. \qquad (2.9a)$$

This eigenvalue problem is solved for each **k**. It follows from the properties (2.3 and 2.5) of the POD that the eigenfunctions are orthogonal and the coefficients $a_k^{(n)}(t)$ are uncorrelated. These are expressed as follows:

$$\int \phi_{i_k}^{(n)} \phi_{ik'}^{(m)*} \, dx_2 = \delta_{nm}\delta_{kk'}, \qquad (2.10)$$

and

$$\langle a_k^{(n)} a_{k'}^{(m)*} \rangle = \lambda_k^n \delta_{mn}\delta_{kk'}. \qquad (2.11)$$

The velocity fluctuations satisfy the continuity equation ($u_{i,i} = 0$) which can be rewritten in terms of the eigenfunctions (using 2.8 and 2.11) as

$$2\pi i \left(l\phi_{1_k}^{(n)} + k\phi_{3_k}^{(n)} \right) + \frac{d\phi_{2_k}^{(n)}}{dx_2} = 0 . \qquad (2.12)$$

It is clear from (2.8) and (2.11) that in order to calculate any second order statistical quantity involving the velocity fluctuations or their spatial derivatives, one needs to know only the eigenvalues and the eigenvectors. A specific example of this will be given in Chapter 6, where an expression for the autocorrelation of the vorticity fluctuations is derived. The contribution to a second order statistical quantity from a specific set of truncations can also be evaluated.

The eigenvalue problem was solved numerically using the experimental data from the wall region ($0 < x_2^+ < 40$) of a pipe flow, with glycerine as the working fluid, by Herzog (1986). The Reynolds number computed from the centerline mean velocity and the diameter of the pipe was 8750. The corresponding Reynolds number based on the friction velocity u_τ was 531. Figure 2.1 shows the variation of the first three eigenvalues, $\lambda_{l,k}^{(n)}$, as a function of the spanwise wavenumber, k, at the zero streamwise wavenumber, l. Figure 2.2 shows the variation of the first three eigenvalues, $\lambda_{l,k}^{(n)}$, as a function of l at $k = 0$. The convergence of the kinetic energy content in successive eigenfunctions is quite rapid. While, the first structure captures about 60 percent of the kinetic energy, the first 3 modes capture 90 percent or more. The three components of the eigenfunctions, for a set of wavenumbers, as a function of the normal distance from the wall, x_2, are shown in figure 2.3. The eigenfunctions are evaluated for each wavenumber (l,k) such that each l and k is either greater than or equal to zero. The relationships among $\phi_{l,k}$, $\phi_{-l,k}$, $\phi_{l,-k}$ and $\phi_{-l,-k}$ are derived using the statistical properties of the autocorrelation tensor. These relationships and some other properties of the eigenfunctions are discussed in Aubry (1987). Of these,

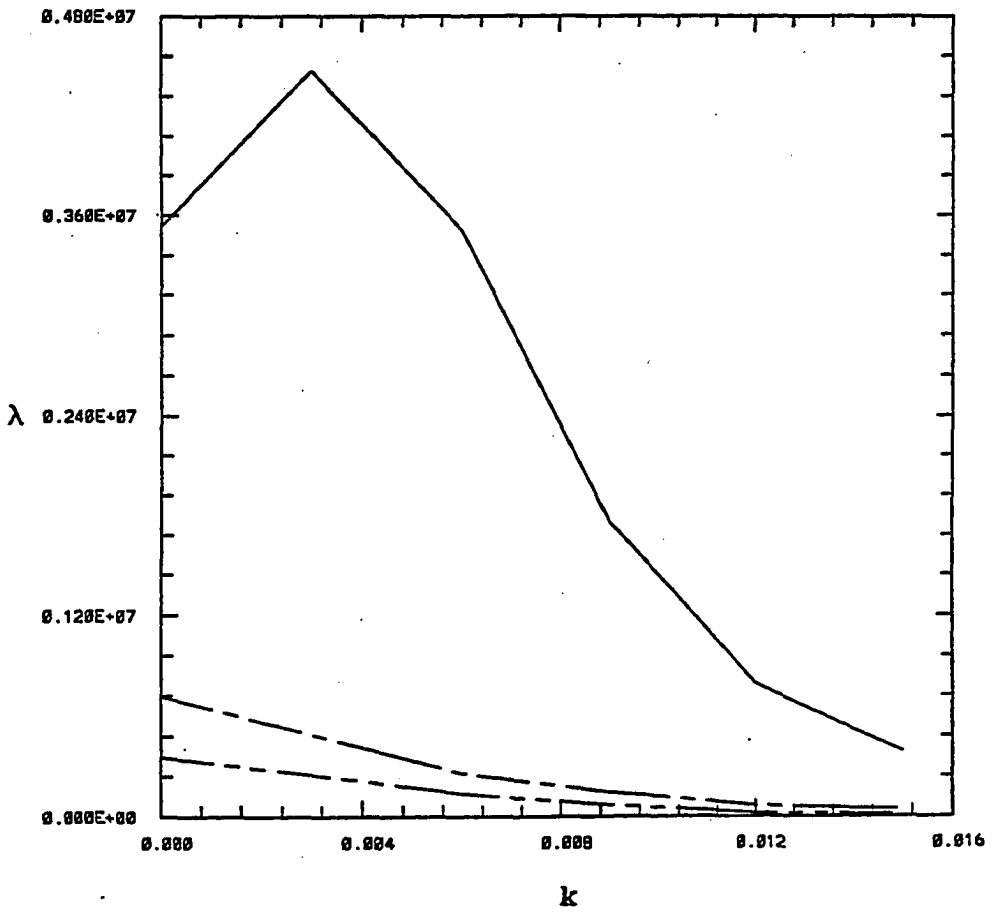

Figure 2.1. Distribution of the eigenvalues, $\lambda_{0,k}^{(n)}$, as a function of the spanwise wavenumber, k (from the experimental data of Herzog, 1986): n = 1 ------, n = 2 ---- -- ---- and n = 3 ---- -- -- ----.

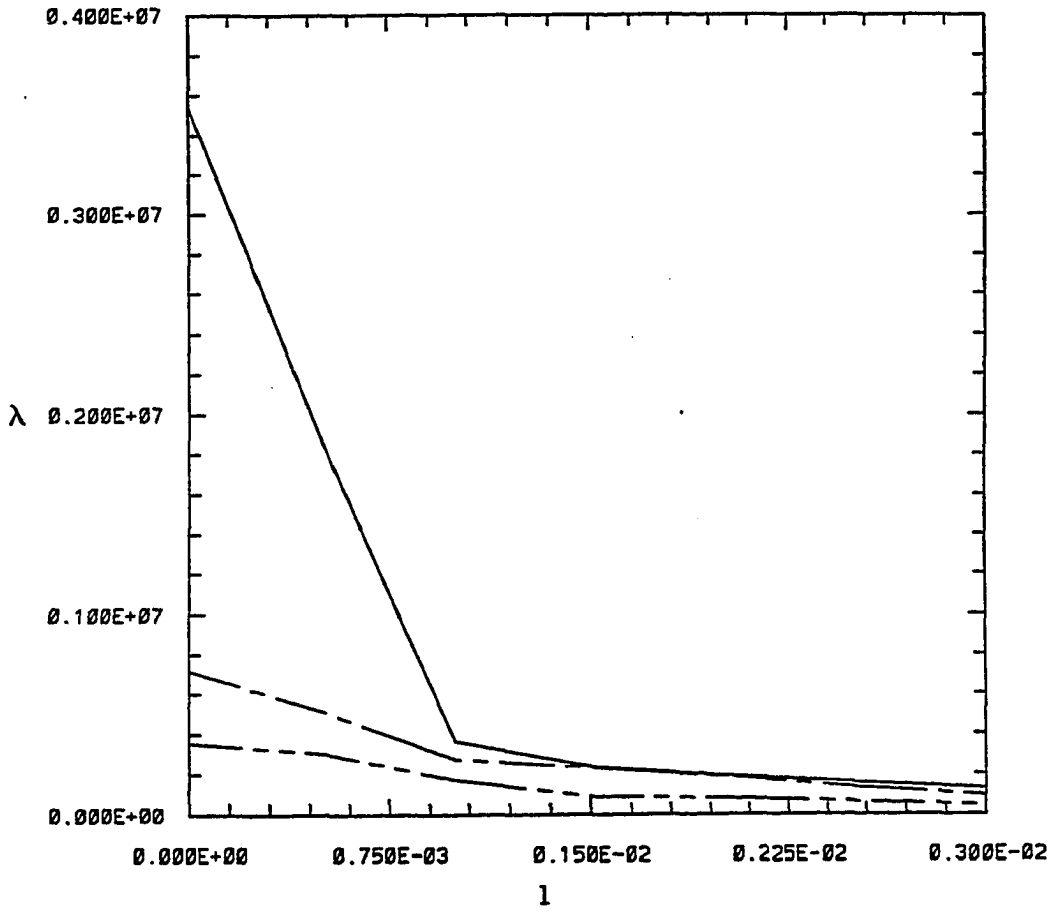

Figure 2.2. Distribution of the eigenvalues, $\lambda_{l,0}^{(n)}$, as a function of the streamwise wavenumber, l (from the experimental data of Herzog, 1986): n = 1 -------, n = 2 ---- -- ---- and n = 3 ---- -- -- ----.

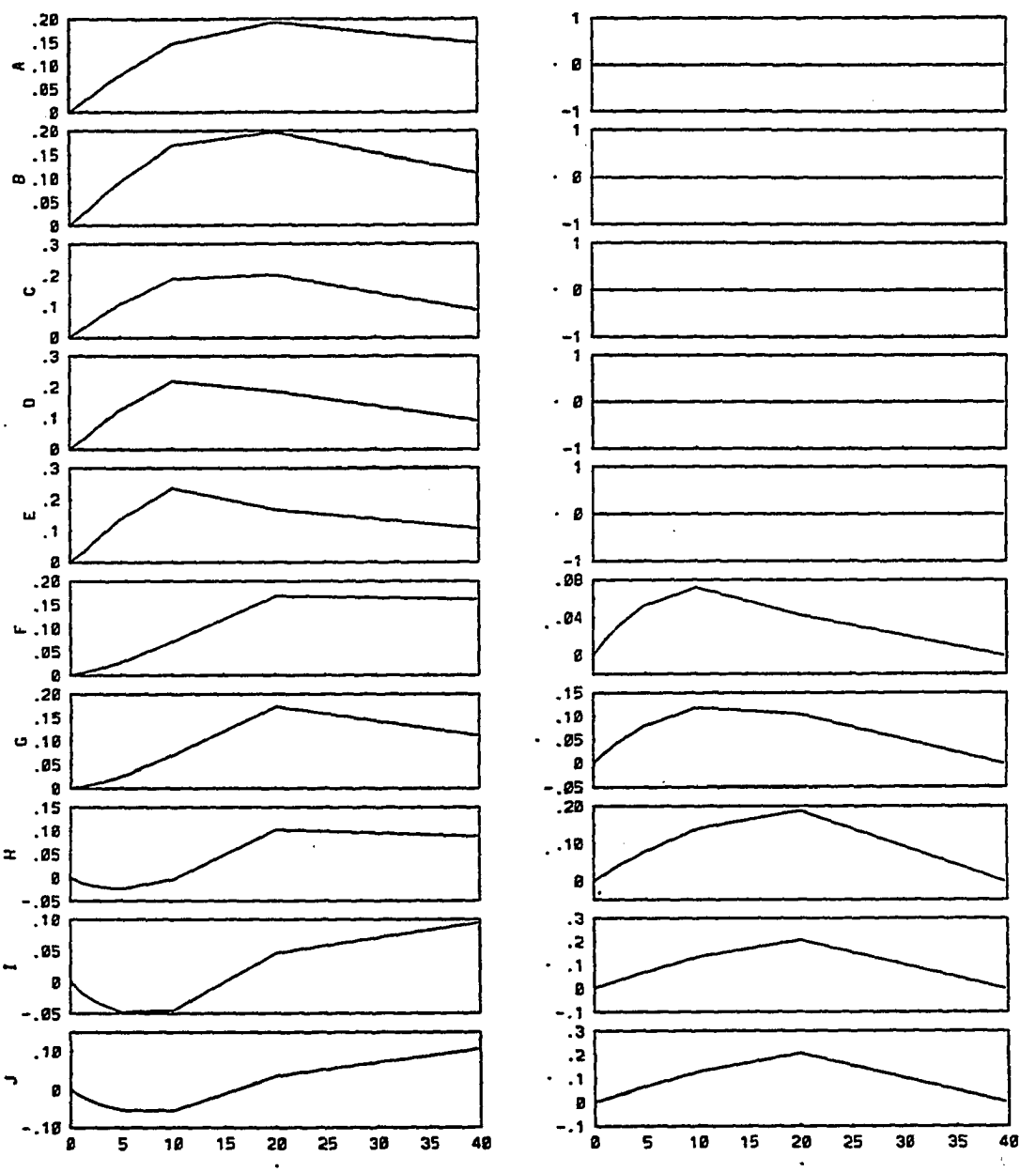

Figure 2.3(a). Real (left) and imaginary (right) parts of the x_1 component of the first eigenfunctions as a function of x_2 for different wave vectors k: (A) $(0, 3\times10^{-3})$; (B) $(0, 6\times10^{-3})$; (C) $(0, 9\times10^{-3})$; (D) $(0, 1.2\times10^{-2})$; (E) $(0, 1.5\times10^{-2})$; (F) $(1.5\times10^{-3}, 3\times10^{-3})$; (G) $(1.5\times10^{-3}, 6\times10^{-3})$; (H) $(1.5\times10^{-3}, 9\times10^{-3})$; (I) $(1.5\times10^{-3}, 1.2\times10^{-2})$; (J) $(1.5\times10^{-3}, 1.5\times10^{-2})$ from the experimental data of Herzog (1986).

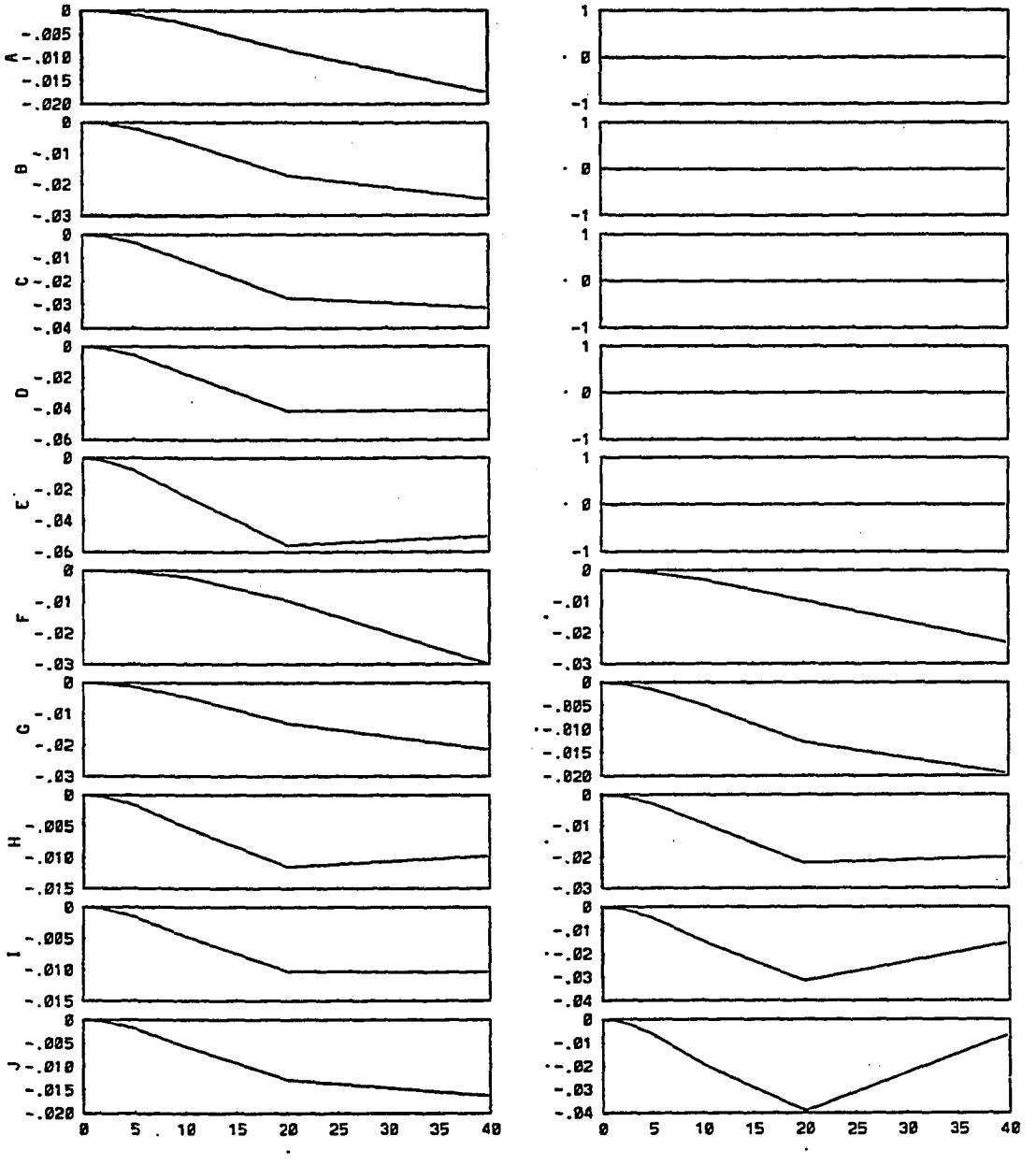

Figure 2.3(b). Real (left) and imaginary (right) parts of the x_2 component of the first eigenfunctions as a function of x_2 for different wave vectors **k**: (A) $(0, 3\times10^{-3})$; (B) $(0, 6\times10^{-3})$; (C) $(0, 9\times10^{-3})$; (D) $(0, 1.2\times10^{-2})$; (E) $(0, 1.5\times10^{-2})$; (F) $(1.5\times10^{-3}, 3\times10^{-3})$; (G) $(1.5\times10^{-3}, 6\times10^{-3})$; (H) $(1.5\times10^{-3}, 9\times10^{-3})$; (I) $(1.5\times10^{-3}, 1.2\times10^{-2})$; (J) $(1.5\times10^{-3}, 1.5\times10^{-2})$ from the experimental data of Herzog (1986).

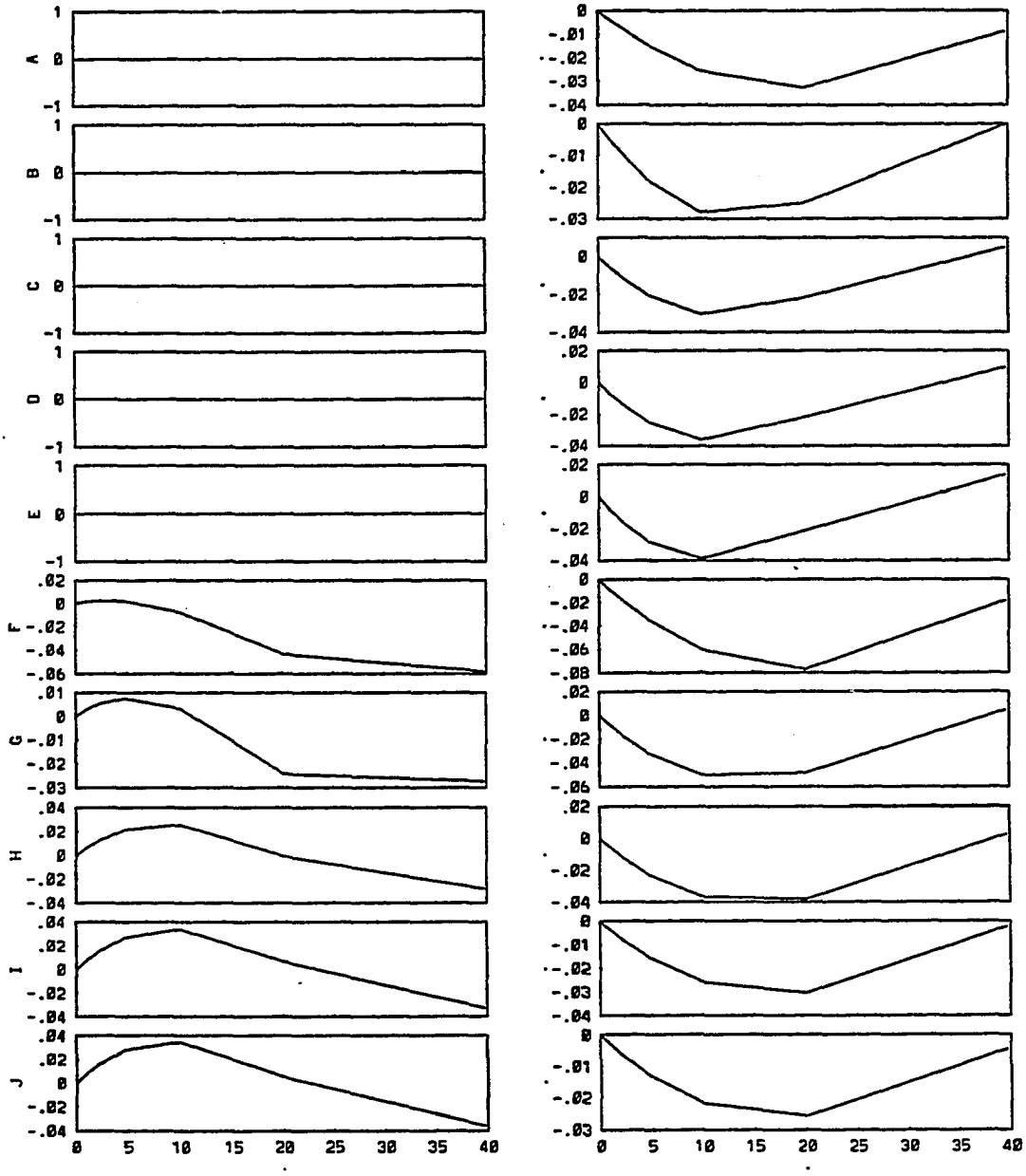

Figure 2.3(c). Real (left) and imaginary (right) parts of the x_3 component of the first eigenfunctions as a function of x_2 for different wave vectors k: (A) $(0, 3\times10^{-3})$; (B) $(0, 6\times10^{-3})$; (C) $(0, 9\times10^{-3})$; (D) $(0, 1.2\times10^{-2})$; (E) $(0, 1.5\times10^{-2})$; (F) $(1.5\times10^{-3}, 3\times10^{-3})$; (G) $(1.5\times10^{-3}, 6\times10^{-3})$; (H) $(1.5\times10^{-3}, 9\times10^{-3})$; (I) $(1.5\times10^{-3}, 1.2\times10^{-2})$; (J) $(1.5\times10^{-3}, 1.5\times10^{-2})$ from the experimental data of Herzog (1986).

two properties are particularly worth noting: a) for the zero streamwise wavenumber (l = 0), the eigenfunctions are either real or imaginary; b) for the zero spanwise wavenumber (k = 0), either ϕ_1 and ϕ_2 are both zero or ϕ_3 is zero. In the study by Aubry *et al.* (1988) and in the present study, only two components of eigenfunctions obtained from Herzog's results are used; the third is derived from equation (2.12) - thus ensuring that the continuity equation is exactly satisfied. Herzog (1986) reconstructed a 'typical eddy' in the physical space by assuming a zero phase lag between successive wavenumbers, and showed that the first eigenmode represents a pair of counter-rotating rolls in the velocity field.

Eigenfunctions have also been obtained (Moin and Moser 1989) from the database generated by the direct numerical simulations of the turbulent channel flow by Kim, Moin and Moser (1987) at a Reynolds number of 6600 (based on the mean centerline velocity and channel width). The shape of these eigenfunctions is quite similar to those obtained by Herzog (1986).

2.2. The Equations of Motion

The velocity, **v** (and the pressure, π) are decomposed into the mean, **U** (and P), -defined as average over the two homogeneous spatial directions- and the fluctuations, **u** (and p), by a classical Reynolds decomposition.

$$\mathbf{v} = \mathbf{u} + \mathbf{U} \quad \text{with} \quad \mathbf{U} = U(x_2)\,\mathbf{e}_1, \tag{2.13}$$

$$\pi = p + P. \tag{2.14}$$

Substitution of (2.13) and (2.14) in the Navier-Stokes equations leads to:

$$\frac{\partial u_i}{\partial t} + u_{i,1}U + U_{,2}u_2\delta_{i1} + u_{i,j}u_j = -\frac{1}{\rho}(p_{,i} + P_{,i}) + \nu(u_{i,jj} + U_{,jj}\delta_{i1}). \tag{2.15}$$

Taking the spatial average of (2.15) a relationship is obtained between the mean velocity, the divergence of the Reynolds stress and the mean pressure:

$$\langle u_{i,j}u_j\rangle = -\frac{1}{\rho}P_{,i} + \nu U_{,jj}\delta_{i1}. \tag{2.16}$$

Using the continuity equation and assuming homogeneity of the flow in the x_1 and x_3 directions lead to the following equations:

$$\langle u_1u_2\rangle_{,2} = -\frac{1}{\rho}P_{,1} + \nu U_{,22} \tag{2.16a}$$

$$\langle u_2^2\rangle_{,2} = -\frac{1}{\rho}P_{,2} \tag{2.16b}$$

Substituting (2.16) in (2.15) gives the following equation for the fluctuating velocity and pressure:

$$\frac{\partial u_i}{\partial t} + u_{i,1}U + U_{,2}u_2\delta_{i1} + u_{i,j}u_j - \langle u_{i,j}u_j\rangle = -\frac{1}{\rho}p_{,i} + \nu u_{i,jj}. \tag{2.17}$$

Integrating (2.16a) with respect to x_2 twice and using the boundary conditions on $\langle u_1u_2\rangle$ leads to the following expression for the mean velocity profile:

$$U = \frac{1}{\nu}\int_0^{x_2}\langle u_1u_2\rangle dx_2 + \frac{u_\tau^2}{\nu}\left(x_2 - \frac{x_2^2}{2H}\right), \tag{2.18}$$

where H is the half height of the channel and u_τ is the friction velocity.

The fluctuating velocity is expanded according to (2.8) and a Galerkin projection using the eigenfunctions as basis vectors is applied to obtain the following set of ordinary differential equations for the time dependent coefficients of the expansion:

$$\frac{da_k^{(n)}}{dt} = \sum_m b_k^{(n)(m)} a_k^{(m)} + \sum_{pqk'} c_{kk'}^{(n)(p)(q)} a_{k'}^{(p)} a_{k-k'}^{(q)} + \sum_{pqrk'} d_{kk'}^{(n)(p)(q)(r)} a_k^{(r)} a_{k'}^{(p)} a_{k'}^{(q)*} - \phi_{2k}^{(n)*} \hat{p}_k(t), \qquad (2.19)$$

where the coefficients b, c and d's are functions of the eigenfunctions (see Appendix A for their full form). The quadratic terms come from the nonlinear fluctuation - fluctuation interactions and represent energy transfer between the different eigenmodes and the Fourier modes. The cubic terms come from the Reynolds shear stress (in the mean velocity expression) - fluctuation interaction. By use of the continuity equation and the boundary conditions, it can be seen by integration by parts that the pressure term disappears if the domain of integration covers the entire flow volume. Since this is not the case (rather the domain is limited to $X_2^+ = 40$), a term containing the Fourier transform of the time dependent fluctuating pressure term evaluated at the upper edge, X_2^+, of the integration domain remains and this appears as the last term in the right hand side of (2.19).

The energy transfer to the unresolved scales is represented by a simple generalization of the Heisenberg spectral model, where the energy transfer to the wavenumbers higher than a cut-off is described by an effective transport coefficient, ν_T, which acts on the eddies of wavenumber smaller than the cut-off. In other words, the influence of the unresolved scales is averaged on the resolved scales. Such a model is fairly crude but it has been used in numerical calculations with considerable success. The

deviatoric part of the Reynolds stress tensor for the unresolved scales, $\tau_{ij>}$, is assumed proportional to the mean strain rate tensor for the resolved scales:

$$\tau_{ij>} = -\nu_T(u_{i,j} + u_{j,i}), \tag{2.20}$$

where > represents the neglected modes. ν_T, the approximate transport coefficient (eddy viscosity), is proportional to the product of the characteristic length scale, $d_>$, and the velocity scale, $u_>$, for the neglected modes and is expressed as:

$$\nu_T = \alpha u_> d_>. \tag{2.21}$$

The velocity scale, $u_>$, is given by the kinetic energy distribution of the higher modes across the layer (up to X_2) in the following way:

$$u_> = \sqrt{\frac{1}{X_2}\int_0^{X_2}\langle u_{i>}u_{i>}\rangle dx_2}\,. \tag{2.22}$$

The characteristic length scale is proportional to the ratio of the kinetic energy and the dissipation of energy and is defined as follows:

$$d_> = \sqrt{\frac{X_2 u_>^2}{\int_0^{X_2}\langle u_{i>,j}u_{i>,j}\rangle dx_2}}\,. \tag{2.23}$$

The product, $u_>d_>$, can, therefore, be expressed in terms of the eigenvalues and eigenfunctions of the neglected modes. This modeling introduces a parameter α, referred

to as the Heisenberg parameter, in the equations. α can be adjusted upward and downward to simulate greater and smaller energy loss to the unresolved modes. The representation changes the linear terms b by a modified viscosity in the following way:

$$b_k = b_k^1 + (1 + \alpha u_> d_>) b_k^2 . \tag{2.24}$$

The isotropic part of the Reynolds stress tensor for the unresolved modes is modeled by assuming that the fluctuations of the kinetic energy of the neglected scales are proportional to the rate of loss of energy by the large scales to the smaller scales. This modeling gives rise to a pseudo-pressure term which adds a term to the coefficient of the quadratic terms as follows (for details see Aubry 1987):

$$c_{k,k'} = c_{k,k'}^1 + \alpha c_{k,k'}^2 . \tag{2.25}$$

Various truncated sets of ODEs (2.19) are integrated numerically. The Heisenberg parameter, α, plays the role of the bifurcation parameter in this dynamical system and as it is varied a rich harvest of nonlinear phenomena is found. Severely truncated models (which did not include the effect of streamwise variations in an explicit way) were studied by Aubry *et al.* (1988) and are reported in the next section.

2.3 Results from the Earlier Studies

In the previous studies (Aubry 1987 and Aubry *et al.* 1988) the expansion of the velocity field was severely truncated to the first eigenmode (n=1), the zero streamwise Fourier mode and six spanwise Fourier modes (k = 0, K_3, $2K_3$, $3K_3$, $4K_3$, $5K_3$) with a periodic cross-stream box length of $L_3^+ = 333$ wall units. This leads to a set of 10 ODEs.

In this first approximation, all the streamwise variations were neglected, based on the experimental observation that the streaks are elongated streamwise patterns. The system of ODEs satisfies the O(2) symmetry which is a consequence of the invariance of the flow (in a statistical sense) with respect to translation and reflection in the spanwise direction.

Typical solutions observed in this model (hereby, referred to as the 10D model) are recalled, since similar, but more complicated, behavior will appear in higher dimensional models. For $\alpha > 2.41$, the zero fixed point is the global attractor. For $2.3 < \alpha < 2.41$ and $1.61 < \alpha < 2.3$, there is a circle of attracting fixed points in the even spanwise Fourier mode (2/4) subspace. The S^1-family (circle) is due to the translation symmetry. Each fixed point represents two pairs of counter-rotating streamwise rolls in a periodic box and corresponds to the streaks of slow fluid going away from the wall. The particle paths of this flow are these low speed streaks. For α between 1.3 and 1.61, the fixed points destabilize and the intermittent solutions appear. For this range of parameter values, there is an S^1-symmetric family of heteroclinic cycles connecting saddle points which are out of phase on the circle of fixed points by π. In the flow field, the rapid event which follows the slowly growing oscillation and the repetition of the process reminds one of the bursting events experimentally observed. A similar window of heteroclinic bursting solutions exists for values of α lying between 2.0 and 2.3, but this type of intermittency is simpler, involving no oscillatory motions in the unstable directions of the fixed points. This window of intermittency is referred to as window I and the previous one as window II. For α between 1.0 and 1.3, the system displays a complex behavior, possibly including chaotic motions. When α decreases below 1.0, modulated travelling waves and travelling waves are observed, representing the spanwise translation of the rolls.

The influence of the fluctuating pressure term has also been studied in this model. As the solutions approach the attracting heteroclinic cycle, the duration of quiescent phases (time between two events) increases. In an unperturbed system, it grows without bound, although numerical errors limit this growth. When the pressure term is introduced in the

equations, it appears as a forcing term of small amplitude. The pressure triggers the burst by preventing the solution from approaching the saddle point too closely. Because of its small amplitude, it does not influence the solution between bursts. It has the effect of randomizing and stabilizing the intervals between bursts, see Aubry *et al.*(1988). In this study, for simplicity, this term will not be included. If heteroclinic cycles persist in higher dimensional models, the effect of such a term is similar as in the 10D model.

In the previous studies, the expansion was truncated to the zero streamwise Fourier mode. Hence, the variables do not depend on x_1 in an explicit way. However, it is necessary to emphasize that this does not represent a fluid flow with no streamwise variations. If this were the case, then as pointed out by Moffatt (1990), the streamwise component of the Navier-Stokes equation would decouple from the spanwise and normal components and turbulence would simply decay. The dependence of the velocity components on x_1 comes from the fact, that the real flow from which the POD modes are derived, is three dimensional. Thus these modes are characteristic of a three dimensional velocity field. As it has been discussed in detail in Berkooz *et al.* (1991) and Berkooz (1991), the effect of such low order truncations is to constrain admissible velocity fields by coupling the cross-stream and streamwise components which causes the ratio of the Reynolds stress and the turbulent kinetic energy to be bounded by a minimum value. Thus, this provides a way by which the cross-stream velocity components can extract energy from the mean flow. It is also appropriate to point out that in the past Hanratty and co-workers (Fortuna and Hanratty 1972, Hatziavramidis and Hanratty 1979) have used two and a half dimensional models, where all the three velocity fluctuations are present but they are assumed to depend on x_2 and x_3 but not on x_1. These models also show a realistic flow behavior.

2.4 Deficiencies of the 10 Dimensional Model

Although the 10D model could reproduce many of the qualitative phenomena experimentally observed in the dynamics of the coherent structures in the wall region, the representation was rudimentary and limited in several ways. There is no doubt that more modes than those retained in the first model are dynamically active in the real fluid flow. The question is to find out how these extra scales modify the basic intermittency due to the saddle-saddle connection and how the different spanwise and streamwise Fourier modes and normal modes destabilize the basic streamwise rolls. A priori, the crudest approximation probably comes from the ignorance of the streamwise variations. As already mentioned, this choice was based on the experimental observation that the characteristic length of the streaks (and therefore streamwise rolls) in the streamwise direction is much larger (about ten times) than that in the cross-stream direction. However, there is no doubt that there are structures in the streamwise direction as well. It is also known that, even though the streaks are elongated, they do not have an infinite length.

A shortcoming of the 10D model is that the bursting event is not characterized by a considerable increase of high wavenumber turbulent motion. It is limited in its amplitude because the transfer of energy towards the smaller scales is interrupted too early. Improvement of this result probably requires addition of the higher order modes. The spanwise cut-off may be already high enough (we cannot increase it anyway since it corresponds to the experimental cut-off) while the streamwise series - limited to the zero mode - is obviously insufficient. Consideration of higher order eigenmodes would probably also help to recover this effect.

Another deficiency inherent in the zero streamwise mode model is that the relative distribution of energy in the three velocity components is not proper. Too much energy is contained in the streamwise component. A detailed study has been performed in Aubry (1987) to examine the supply of energy as extra modes are added. It is shown that the first

eigenmode retains at least 65 percent of the energy in all three directions. This is certainly good enough in a first approximation. The issue of concern is the truncation of the Fourier series. Reduction of the spanwise series from 17 modes to 6 modes which affects the wavenumber increment of the series does not make a significant difference across the whole layer. However, matters are quite different in the streamwise direction. Addition of other streamwise wavenumbers (and even one) helps considerably in recovering the right relative amount of energy and that the best repartition of the energy is obtained when the streamwise length L_1 is 666 wall units.

In conclusion, the major limitation of the 10D model was the non existence of explicit streamwise variations. The consequences of this include the relative deficiency of the energy contained in the normal and spanwise velocity components - compared to the streamwise component - and the total exclusion of physical phenomena such as the streamwise instabilities which should lead to some interesting phenomena during the bursts. While the dynamics of ODEs cannot be controlled a priori, it is possible to control the input of energy by the choice of the number and values of the modes.

Chapter 3

Properties of the Ordinary Differential Equations

The procedure for deriving the set of dynamical equations (2.19) for the time coefficients, $a_{l,k}^{(n)}$, was explained in the last chapter. In this chapter some properties of the set of ODEs truncated with N eigenmodes, $(N_1 + 1)$ non-negative Fourier streamwise modes - 0, K_1, $2K_1$, .. N_1K_1 - and $(N_3 + 1)$ non-negative Fourier spanwise modes - 0, K_3, $2K_3$, .. N_3K_3 - are discussed. The complexities due to the addition of the non-zero streamwise modes are also analyzed.

3.1 Dimensionality of the System

The dimensionality of the system is determined by the number of independent time coefficients, $a_{l,k}^{(n)}$. In (2.8), l varies from $-N_1$ to N_1, k varies from $-N_3$ to N_3 and n varies from 1 to N. The velocity field is real and this imposes some constraints on the coefficients. Using the relationship between $\phi_{l,k}$, $\phi_{-l,k}$, $\phi_{l,-k}$ and $\phi_{-l,-k}$, it has been shown (Aubry 1987) that $a_{l,k}^{(n)}$ and $a_{-l,-k}^{(n)}$ are also related. Thus, the set of ODEs (2.19) is solved for $a_{l,k}^{(n)}$, $a_{-l,k}^{(n)}$, (with l, k positive and $l \neq 0$), $a_{0,k}^{(n)}$(k positive), and $a_{l,0}^{(n)}$ (l positive). The $a_{0,0}^{(n)}$ mode decays to zero under the influence of viscosity and hence, is not considered (a detailed discussion is given in section 2 of this chapter). This scheme is shown in a matrix

form in table 3.1, where the spanwise modes are shown by columns, the streamwise modes by rows and the blank boxes represent the coefficients determined from the relationships between $a^{(n)}_{l,k}$ and $a^{(n)}_{-l,-k}$.

Hence, the number of the equations to be solved is $N(2N_1N_3 + N_1 + N_3)$ and since the unknown quantity is a complex variable, the dimensionality of the system (the number of ODEs to be solved) is twice this number. In the system studied in Aubry *et al.* (1988), N, N_1 and N_3 were 1, 0 and 5 respectively. Thus that system had a dimensionality of 10. The addition of the streamwise modes increases the number of unknowns considerably. Every extra streamwise Fourier mode l (and of course its counterpart $-l$) adds not only the modes (l, k) (with $l > 0$) but also $(-l, k)$. The number of the new complex unknowns included in the system by the addition of each extra mode l is $2N_3+1$ (not just N_3).

$(-N_1,N_3)$	$(-2,N_3)$	$(-1,N_3)$	$(0,N_3)$	$(1,N_3)$	$(2,N_3)$	(N_1,N_3)
$(-N_1,3)$	$(-2,3)$	$(-1,3)$	$(0,3)$	$(1,3)$	$(2,3)$	$(N_1,3)$
$(-N_1,2)$	$(-2,2)$	$(-1,2)$	$(0,2)$	$(1,2)$	$(2,2)$	$(N_1,2)$
$(-N_1,1)$	$(-2,1)$	$(-1,1)$	$(0,1)$	$(1,1)$	$(2,1)$	$(N_1,1)$
				$(1,0)$	$(2,0)$	$(N_1,0)$

Table 3.1 Matrix (l,k) representing the various time coefficients for a single value of n. The marked boxes represent the modes evaluated from (2.19).

3.2 Coefficients of Various Terms

The equations for the coefficients of the linear ($b_{l,k}^{(n)(m)}$), quadratic ($c_{l,l',k,k'}^{(n)(p)(q)}$), and cubic ($d_{l,l',k,k'}^{(n)(p)(q)(r)}$) terms are given in appendix A. In this section some properties of these terms and the complexities due to the addition of the non-zero streamwise modes are recalled from Aubry (1987). The increase in the number of the terms because of the addition of the extra eigenmodes is also studied.

The contribution to the turbulence production of all the pairs of Fourier modes (l, k) of the first eigenmode is always positive according to the experimental data (except for the first non-zero streamwise wave number corresponding to a streamwise length of $L_1^+ = 2000$). This positive contribution is due to the opposite signs of the streamwise and normal components of the first eigenmode. This has two consequences: First, the real part of the coefficients b^1 of the linear term is positive and represents a supply of energy from the mean flow (more specifically the mean pressure gradient). Second, the real part of the cubic terms - which come from the Reynolds shear stress $\langle u_1 u_2 \rangle$ in the expression of the mean velocity - is negative. This guaranties the global stability of the solution and reflects that, for the most energetic coherent structure (n=1) which are streamwise elongated vortices, the mean flow, through the Reynolds shear stress, stabilizes the perturbation as it grows.

In a zero streamwise mode model, the components of the eigenfunctions are either real or imaginary which makes all the coefficients of the equations real (this was the case in the 10D model). This is due to the special property of the autocorrelation tensor at zero streamwise lag. With the inclusion of the non-zero streamwise modes, a general coefficient of the ODEs is a complex number.

Consideration of the streamwise variations introduces new terms in the equations. The source of energy in the linear terms comes from the interaction between the mean

flow and the fluctuation. It has two origins: one is a part of the term $U_{,2}u_2\delta_{i1}$, in the Navier-Stokes equations; the other a part of $u_{i,1}U$. The former was the only linear energy source term in the zero streamwise mode model since all the streamwise variations were neglected. The latter is computed in this investigation and brings energy to the system through the non-zero streamwise modes. The same phenomenon happens in the cubic terms whose origin is the same in the Navier-Stokes equations. Thus, two extra terms (linear and cubic) appear in the set of equations because of the presence of non-zero streamwise Fourier modes.

The inclusion of more normal modes leads to a considerable complexity in the system of equations. For the cases with 1 normal mode the superscripts in all the coefficients can be deleted but in the general case of any number of modes they cannot. This inclusion increases the dimensions of the matrix of quadratic coefficients by a factor of N^3 and of the cubic coefficients by N^4. Another issue, which arises because of the additional eigenmodes, is determining whether the mode $a_{0,0}^{(n)}$ decays to zero under the influence of viscosity. For the n = 1 case, the equation for this mode reduces to just one linear term, whose real part is less than zero (found computationally from the data). When n = N, then the equation for $a_{0,0}^{(n)}$ has N linear terms. In this case the decay of the $a_{0,0}^{(n)}$ mode is checked by calculating the eigenvalues of the matrix of the coefficients (b's) in the right hand side of the following equation:

$$\frac{da_{0,0}^{(n)}}{dt} = \sum_{m=1}^{N} b_{0,0}^{(n)(m)} a_{0,0}^{(m)} . \qquad (3.1)$$

For the N > 1 cases studied in this work, it is found that the $a_{0,0}^{(n)}$ modes indeed decay to zero.

3.3 Invariant Subspaces and Symmetries

The ODEs have several important invariant subspaces which are very general and come from the intrinsic nature of the equations, regardless of the number of spanwise and streamwise wavenumbers. These subspaces reflect the properties of the original fluid flow which are satisfied by the Navier-Stokes equations. An invariant subspace is a subset of the full space and has the property that a solution starting with the initial conditions belonging to this subspace stays there for all times. The existence of some of these subspaces considerably influences the behavior of the general solutions.

The first invariance is that which reflects the property of homogeneity of the flow in the spanwise and streamwise directions, that is the statistical invariance under translation in these two directions. The ODEs are invariant under the transformation:

$$a_{l,k}^{(n)} \rightarrow a_{l,k}^{(n)} e^{i(l\theta+k\gamma)}, \qquad (3.2)$$

where θ and γ are arbitrary values. As it has been shown in Stone (1989), this invariance leads to the conclusion that equilibrium solutions for (2.19), for which at least one of $a_{l,k}^{(n)} \neq 0$, do not occur singly but in circles or two dimensional tori.

Another invariant subspace is the zero streamwise wavenumber subspace: $l = 0$. If a variable $a_{l,k}^{(n)}$(for all $l \neq 0$) is initially zero, it stays zero since the triplet ($l \neq 0$, $l' = 0$, $l'' = 0$) does not constitute a resonant triad. This dimension of this subspace is $2NN_3$ (that is 10 for N =1 and $N_3 = 5$). Similarly, the same argument can be used to show that the subspace $k = 0$ is an invariant $2NN_1$ (that is 2 for N =1 and $N_1 = 1$) dimensional subspace. It should, however, be mentioned that the n = 1 subspace is not invariant.

Other important subspaces are the k-even subspace and the l-even subspace. It is easy to see this invariance by considering a resonant triad. An even mode initially zero can

be excited by the non-zero odd modes: the odd subspace is not invariant. However, if all the odd modes are initially zero, they will remain zero: the even subspace is an invariant subspace.

The last invariance is that of the subspace:

$$a^{(n)}_{-l,k} = (a^{(n)}_{l,k})^* \cdot \tag{3.3}$$

In the physical space, this subspace corresponds to the structures invariant under reflection about a plane $x_3 = 0$. This can be easily shown by expanding the equations $u_i(x_3) = \varepsilon_i u_i(-x_3)$ (where ε_i is equal to +1 if i = 1 or 2, -1 if i = 3) in terms of the expansion (2.8) and using the above relation between $a^{(n)}_{-l,k}$ and $a^{(n)}_{l,k}$. Note that integrating the set of ODEs in this subspace is equivalent to imposing the cross-stream reflection symmetry of the flow instantaneously.

The complete set of ODEs satisfies two types of symmetries with respect to the spatial coordinates, which is a result of the invariant subspaces. There is invariance with respect to translation in the streamwise direction and invariance with respect to translation and reflection in the spanwise direction. In the dynamical systems terminology the former is termed as the SO(2) equivariance and the latter as the O(2) equivariance. In the 10D model the variables do not vary with x_1 in an explicit manner and so the ODEs satisfy the O(2) equivariance only. Armbruster *et al.* (1988) proved that this symmetry group leads to structurally stable heteroclinic cycles in certain interactions. When the non-zero streamwise modes are added, the system satisfies an O(2) X SO(2) equivariance. This different symmetry requirement could lead to some new types of solutions.

In the next chapter the detailed results of integration for systems of equations with $N_1 = 1$ and $N_1 = 2$ are presented. The number of non-zero spanwise modes is restricted to 5. This leads to systems of dimension 32 (for $N_1 = 1$) and 54 (for $N_1 = 2$). One important

consequence of the symmetries listed above is that the lower order systems are invariant subspaces of the new systems. For example, the 10D model of Aubry lies in the $l = 0$ space, which is an invariant subspace. Consequently, if one starts from a 32 or 54 dimensional system with zero values for all non-zero l values of $a_k^{(n)}$ then these coefficients will remain zero. It will be interesting to observe what happens when the solutions start from the general initial conditions. Do the same intermittencies, which were present in the previous case of the 10D model, occur in the higher dimensional models? Are there any new classes of intermittent solutions which involve the newly added terms?

Chapter 4

Results of Numerical Simulations

Numerical integrations have been carried out for models which include 1 and 2 non-zero streamwise modes. A Runge-Kutta-Verner method of fifth and sixth order was used in double precision arithmetic and these computations were carried out on an IBM 3090. The algorithms were checked by computations starting from initial conditions chosen to satisfy the various invariant subspaces discussed in section 5.3. The step size used for these computations was 0.02; it was observed that a reduction in the step size did not lead to any change in the results. The initial conditions, from which these solutions were computed, were from the general space and did not satisfy any invariances. In order to compute the coefficients for the linear, quadratic and cubic terms of the ODEs, the first and second derivatives of the eigenfunctions, $\phi_{i_k}^{(n)}(x_2)$, are needed. Herzog's data was obtained only at 6 points and was, therefore, curve-fitted to evaluate the derivatives. All the quantities evaluated in this thesis are non-dimensionalized by wall units.

4.1 The 32 Dimensional Model

The first extension to the 10D model was done by adding an extra streamwise mode, which led to a 32 dimensional system with $N = 1$, $N_1 = 1$, and $N_3 = 5$. The first question which one encounters is the choice of non-zero streamwise modes. Figure 2.2

shows the variation of eigenvalues as a function of l for $k = 0$. Such a distribution is seen for all values of k. Unfortunately, this distribution is not of much help, as it shows a decay in eigenvalues after a maximum at $l = 0$. However, one can calculate the contributions to the second order statistical quantities from any set of truncations. Such a study was performed in Aubry (1987) to find the rms values of the three velocity components (as a function of x_2) for different sets of truncations. The results showed that if only one non-zero streamwise mode is added, then the mode with the streamwise wavenumber = 0.0015 (in wall units) gives the best distribution of the rms values of the velocity components. This corresponds to the streamwise dimension of the domain equal to 667 wall units. Another criterion for the selection of additional modes on the basis of vorticity is developed in Chapter 6. It is, however, sufficient to mention here that this criterion also justifies the choice of the above wavenumber. In the discussions in this section and the next one, cases with only one eigenmode (N = 1) are considered and hence the modes are specified by $a(l,k)$ or $a_{l,k}$.

The behavior of typical solutions for different values of the Heisenberg parameter α (for $L_1 = 667$) is outlined. When α is larger than 1.53, the trivial solution is the global attractor. For $1.52 \leq \alpha \leq 1.51$ a non zero fixed point is observed in the ($l = 0$, even k) subspace. As α decreases from 1.50 to 1.22, the solution becomes intermittent in the zero streamwise mode subspace. This intermittency is similar to window I of intermittency present in the 10D model of Aubry *et al.* (1988) and rather simple. For $1.22 \leq \alpha \leq 1.06$, the solution is steady again and is a combination of the modes (0,2) and (0,4) only. Another window (II) of intermittency appears for $1.05 \leq \alpha \leq 0.88$. This intermittency is of the same type as that of window II of intermittency in the 10D model. It occurs in the zero streamwise mode subspace. The non-zero streamwise modes decay very fast. As in the window II of intermittency of the 10D model, the (0,2)/(0,4) mixed modes are destabilized in the (0,1)/(0,3)/(0,5) directions. This solution encounters bursts involving growing oscillatory motions of the spanwise even and odd modes (at constant modal phases),

corresponding to cross-stream oscillations of the streamwise rolls followed by a sudden breakup. Until now, the sequence and nature of the solutions observed have been very similar to those observed in the 10D model (see Aubry *et al.* (1988) for time series), indicating that the zero streamwise mode subspace is attracting for the whole system. In these solutions, the non-zero streamwise modes are inactive after a very short transient during which they decay to zero. As α decreases further, the invariant zero streamwise subspace becomes unstable. For $0.80 \leq \alpha \leq 0.91$, a third window of intermittency is observed. Between the bursts, the solution is the same as in the first and second windows, almost steady since it stays in a neighborhood of one equilibrium in the zero streamwise/even spanwise subspace. However, it changes significantly during the bursts since all the modes then participate to the dynamics. Figure 4.1 reproduces time series for the real part of some of the coefficients $a_{l,k}$. The planar projections of the phase space for some selected coefficients are shown in figure 4.2. For $0.50 \leq \alpha \leq 0.80$, the solution is attracted to the zero streamwise subspace where it becomes much more complex, apparently chaotic. The heteroclinic cycle starts travelling and then becomes unstable. At this time, the non-zero streamwise modes collapse. For lower values of α, the $(l = 0)$-subspace is unstable again and a fourth window of intermittency arises. In the intermittent behavior previously described, the solution between the bursts was always quasi steady due to the proximity of a fixed point. The new solution is different in nature: it is very disorganized, apparently chaotic between the bursts in the zero streamwise subspace and this degree of complexity increases during each burst due to the sudden excitement of the non-zero streamwise modes of high frequency motions. This is shown in figure 4.3 where time series for the real part of some of the coefficients $a_{l,k}$ are shown for $\alpha = 0.2$. It is speculated that the cause of the intermittency is the presence of an attracting heteroclinic cycle (in a generalized sense) which connects hyperbolic, apparently chaotic, objects. The saddle is no longer a fixed point but the complicated region of the zero streamwise subspace, the attractor (perhaps strange) of the solution when the initial condition lies in the

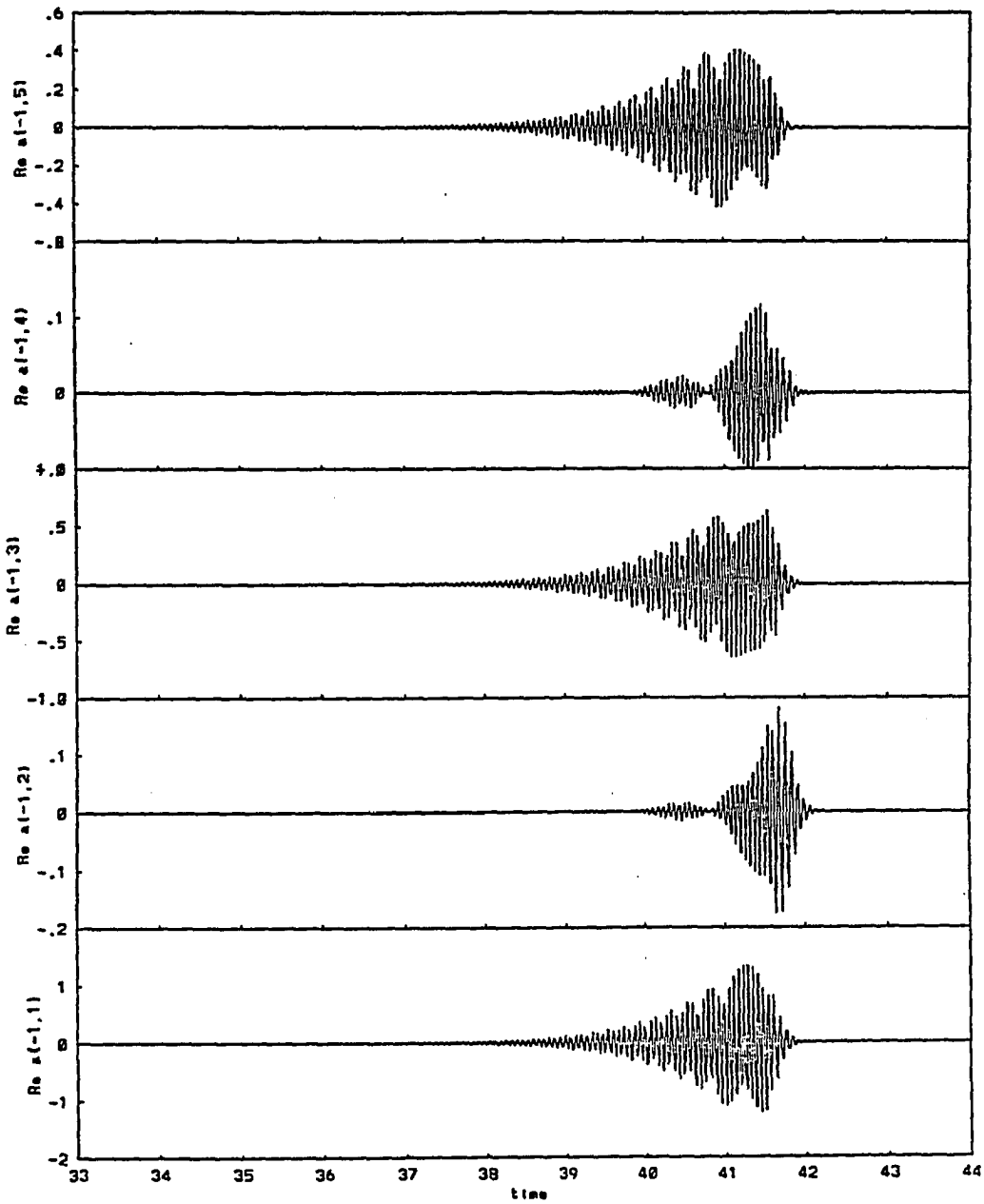

Figure 4.1. Typical solution in the window III of intermittency of the 32 dimensional system. Time series of the real parts of a_{-11}, a_{-12}, a_{-13}, a_{-14} and a_{-15} for $\alpha = 0.87$.

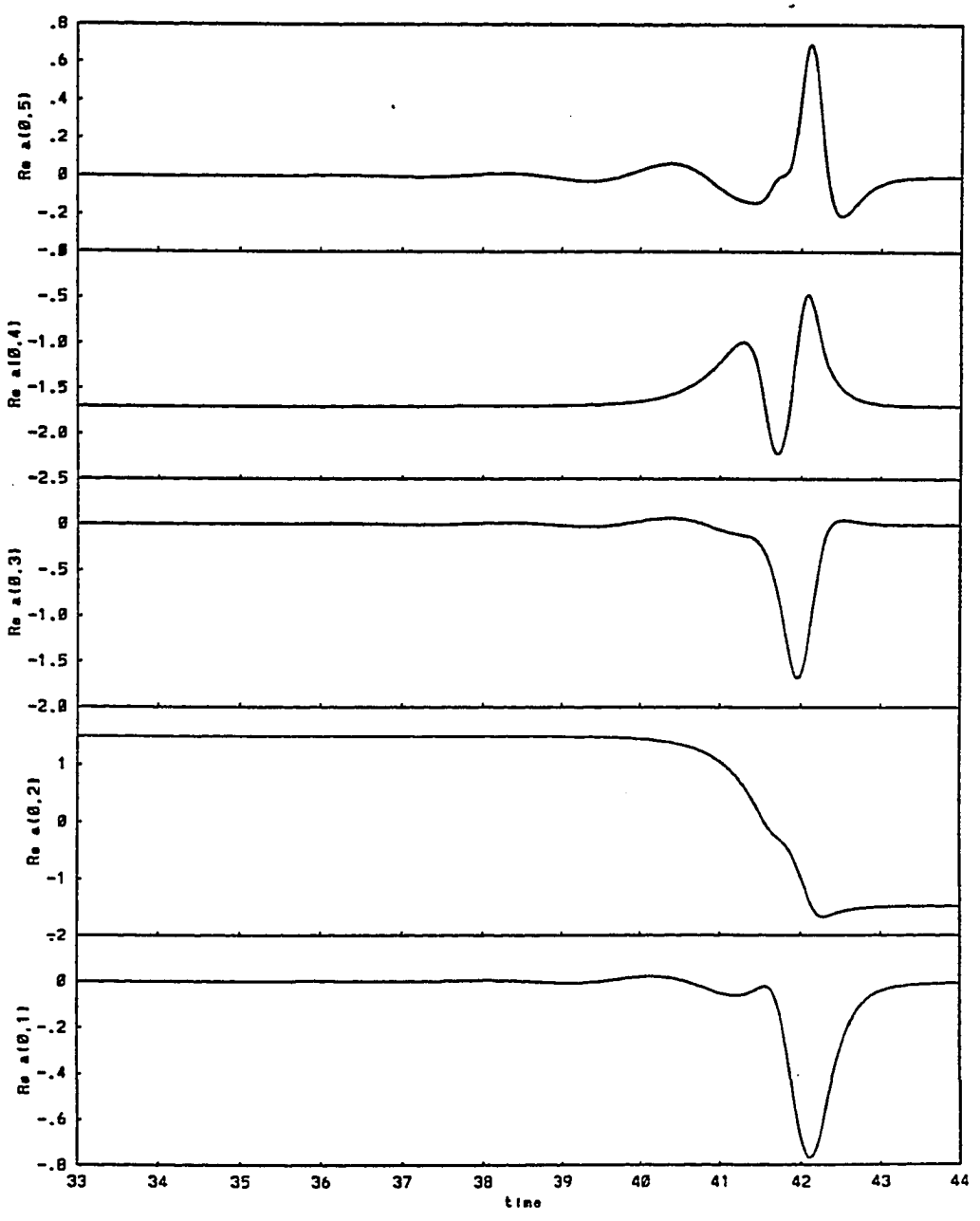

Figure 4.1 (continued). Typical solution in the window III of intermittency of the 32 dimensional system. Time series of real parts of a_{01}, a_{02}, a_{03}, a_{04} and a_{05} for $\alpha = 0.87$.

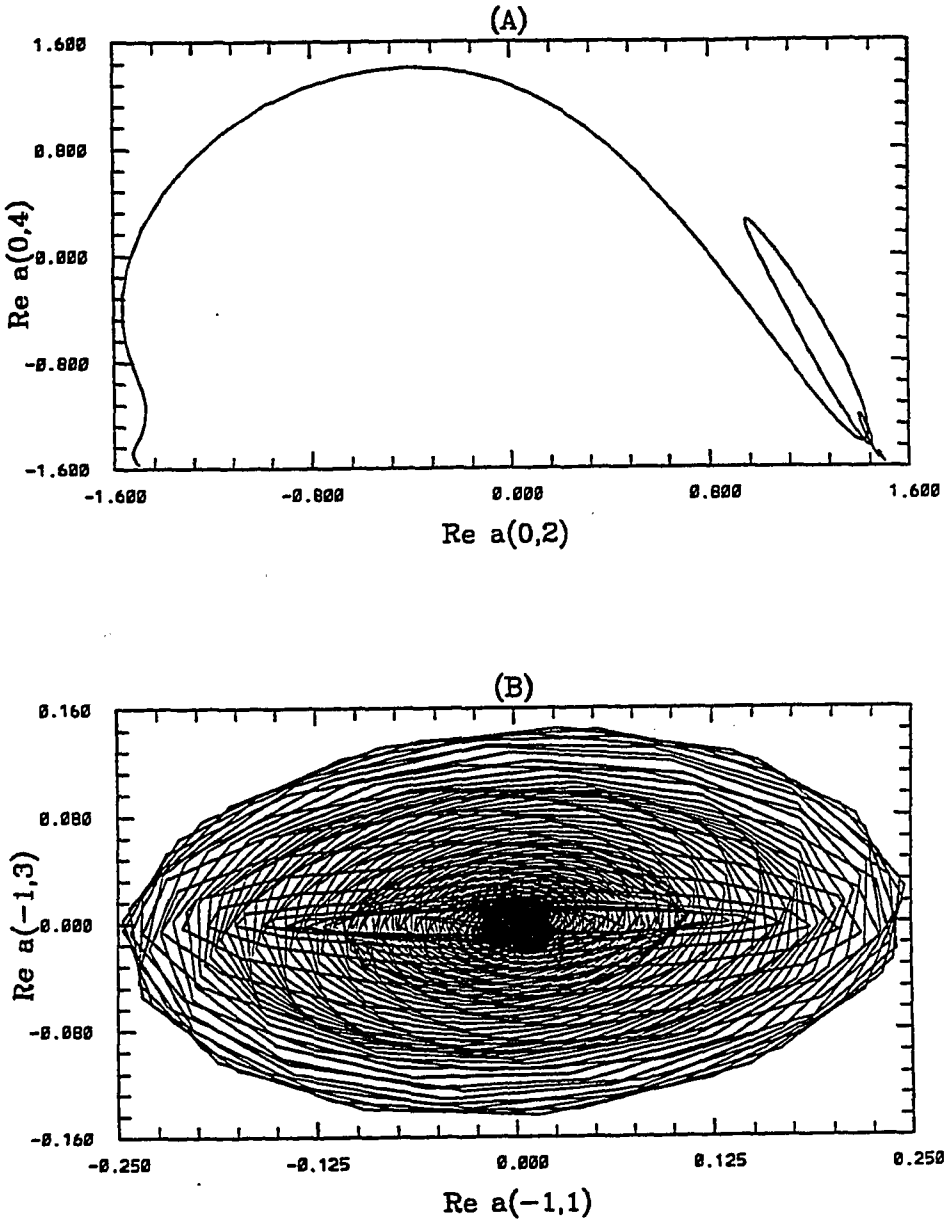

Figure 4.2. Selected projections of the phase planes in window III of intermittency of the 32 dimensional system for $\alpha = 0.87$. (A): Projection on the Re (a_{02}) - Re (a_{04}) plane of one burst event showing the passage of the solution from one fixed point to the other. (B): Projection on the Re (a_{-11}) - Re (a_{-13}) plane of one burst event showing growing linear instability near the fixed point.

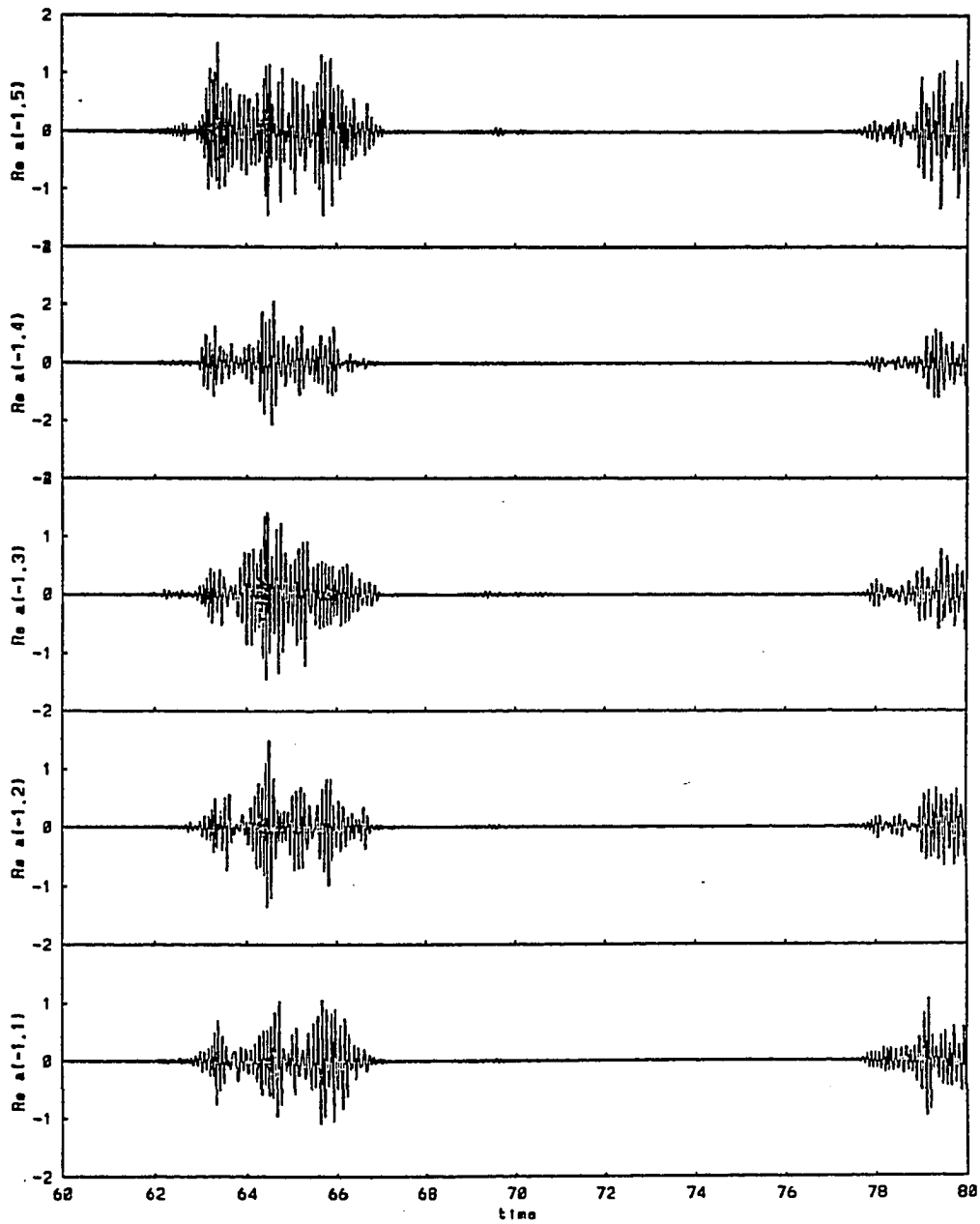

Figure 4.3. Typical solution in the window IV of intermittency of the 32 dimensional system. Time series of real parts of a_{-11}, a_{-12}, a_{-13}, a_{-14} and a_{-15} for $\alpha = 0.2$.

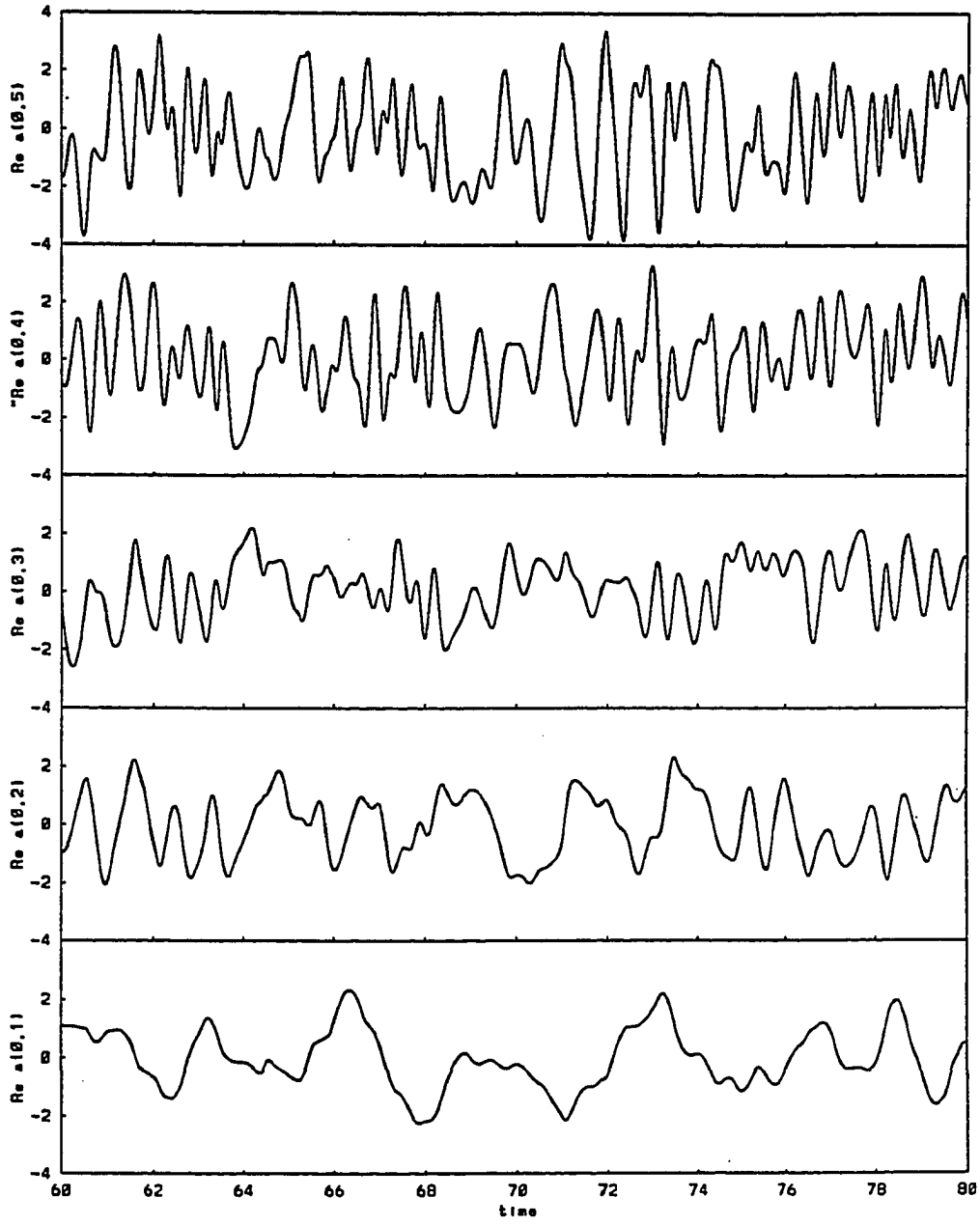

Figure 4.3 (continued). Typical solution in the window IV of intermittency of the 32 dimensional system. Time series of real parts of a_{01}, a_{02}, a_{03}, a_{04} and a_{05} for $\alpha = 0.2$.

zero streamwise subspace. For an initial condition outside of any invariant subspace, the solution leaves the ten dimensional zero streamwise subspace, starts a brief excursion in the full 32 dimensional phase space and comes back to the zero streamwise subspace. The different solutions observed are listed below in table 4.1.

Heisenberg parameter α	behavior
$\alpha \geq 1.53$	trivial solution: $a_{l,k} = 0\ \forall(l,k)$, is the global attractor.
$1.52 \geq \alpha \geq 1.51$	stable fixed point: $a_{02}, a_{04} \neq 0$, other modes are zero.
$1.50 \geq \alpha \geq 1.22$	intermittency in the $a_{0,k}$ subspace: $a_{1,k} = 0\ \forall k$, a_{02}, $a_{04} \neq 0$; $a_{0,k} = 0\ \forall k \neq 2, 4$ between bursts. $a_{0,k} \neq 0$ $\forall k$, during bursts (no oscillations).
$1.22 \geq \alpha \geq 1.06$	stable fixed point: $a_{02}, a_{04} \neq 0$, other modes are zero.
$1.05 \geq \alpha \geq 0.91$	intermittency in the $a_{0,k}$ subspace: $a_{1,k} = 0\ \forall k$, $a_{02}, a_{04} \neq 0$; $a_{0,k} = 0\ \forall k \neq 2, 4$ between bursts. $a_{0,k}$ $\neq 0\ \forall k$, during bursts (a_{01}, a_{03}, a_{05} oscillate).
$0.90 \geq \alpha \geq 0.80$	intermittency in the full space: $a_{02}, a_{04} \neq 0$; $a_{0,k} = 0$ $\forall k \neq 2, 4$, between bursts. $a_{l,k} \neq 0\ \forall(l, k)$ during bursts.
$0.80 \geq \alpha \geq 0.50$	complex behavior in the $a_{0,k}$ subspace: $a_{1,k} = 0 \forall k$; $a_{0,k} \neq 0\ \forall k$.
$0.40 \geq \alpha \geq 0.10$	intermittency in the full space: complex behavior in the $a_{0,k}$ subspace between bursts. $a_{l,k} \neq 0\ \forall(l,k)$ during bursts.
$0.10 \geq \alpha$	complex behavior in the full space: $a_{l,k} \neq 0\ \forall(l,k)$.

Table 4.1. Qualitative dynamical behavior in the 32 dimensional system ($L_1 = 667$).

Since the first three types of intermittency appear through bifurcations from the fixed points, the nature of these bifurcations is investigated. This was done in Aubry *et al.* (1988) for the 10D dynamical system in which the second window of intermittency appeared through a subcritical Hopf bifurcation. As in their study, the stability calculation can be limited to one of the two real fixed points: $a_{02} = -r_2$, $a_{04} = -r_4$ where r_2 and r_4 are strictly positive values and all other components are zero, without loss of generality. The result will be the same for any element of the symmetric S^1 circle of fixed points. Linearization of the full system at this fixed point leads to the diagonalization of the 32×32 block matrix as follows: (Re(a_{02}),Re(a_{04})), a 2×2 matrix, (Im(a_{02}),Im(a_{04})), a 2×2 matrix, (Re(a_{01}), Re(a_{03}), Re(a_{05})), a 3×3 matrix, (Im(a_{01}), Im(a_{03}), Im(a_{05})), a 3×3 matrix, (a_{-11}, a_{-13}, a_{-15}, a_{11}, a_{13}, a_{15}), a 12×12 matrix and (a_{-12},a_{-14}, a_{10}, a_{12}, a_{14}), a 10×10 matrix. One eigenvalue of the imaginary part of a_{02} and a_{04} has always zero real part (as in the 10D system) which corresponds to variations along the S^1 circle of fixed points, its eigenvector being tangent to this circle. The eigenvalues of the matrices involving the non-zero streamwise wave number are always complex conjugates. All the eigenvalues for different values of α are listed in Appendix B. For parameter values greater than 1.50, all eigenvalues have negative real parts, showing that the fixed point is stable. The first bifurcation occurs at $\alpha = 1.50$ at which an eigenvalue becomes positive in the imaginary part of zero streamwise, odd spanwise mode subspace. The fixed point becomes a saddle with one dimensional unstable manifold. This corresponds to the appearance of the first window of intermittency. The fixed point recovers its stability in a small window (all eigenvalues are negative for $\alpha = 1.10$ and 1.20). A Hopf bifurcation occurs at $\alpha = 1.06$ and the numerical integration shows that the solution becomes intermittent again. The fixed point is then a saddle with two dimensional unstable manifold in the zero streamwise, odd spanwise subspace. Another Hopf bifurcation occurs at about $\alpha = 0.91$, where an eigenvalue crosses the imaginary axis in the non-zero streamwise, odd spanwise subspace. This starts the third window of intermittency where odd spanwise

modes (in both, $l = 0$ and $l = 1$ spaces) start the burst. The fixed point is a saddle point with a four dimensional unstable manifold. At the other real fixed point , $a_{02} = +r_2$, $a_{04} = -r_4$, all the eigenvalues of the subsystems mentioned above are the same, except that those of the real and imaginary part of (a_{01},a_{03},a_{05}) are interchanged. At that point, the unstable manifolds in the first and second windows of intermittency lie in the (Re(a_{01}), Re(a_{03}), Re(a_{05})) subspace. At all other points of the circle, the unstable manifold is a rotation of one of these two manifolds and thus, all the odd spanwise modes are triggered, as seen in the numerical integrations of the system.

In this study of the linear stability of the fixed point, it has been shown that the first two windows of intermittency appear from a linear instability of the fixed points in the zero streamwise subspace while the third window of intermittency occurs through an additional linear instability of the non-zero streamwise subspaces. In all cases, the unstable manifold of the fixed points lies in the odd spanwise subspace. However, the numerical integration shows that the non-zero streamwise, even spanwise modes burst as well. The bursting of these modes occurs through quadratic terms which are of the form $a_{l'k'}a_{l-l',k-k'}$. A study of the equation of $a_{1,k}$ (where k is even) shows that all the quadratic terms have the following form:

$$a_{0,k'}\, a_{1,k-k'},$$

where both k' and $k-k'$ are either odd or even. So the set of conditions under which these modes can be excited is that either the unstable manifold lies in the odd spanwise subspace of the zero as well as the non-zero streamwise modes or it lies in the even spanwise subspace of non-zero streamwise modes. The former condition is satisfied in the third window of intermittency and hence, the even spanwise non-zero streamwise modes also get triggered by the nonlinear interactions. Moreover, once the even spanwise modes are sufficiently carried away from the fixed point values, the nonlinear even/even spanwise modes interactions also contribute to the burst. This is, thus, a nonlinear instability which is delayed in time (see time series in figure 4.1, where a_{-12} and a_{-14} start oscillating after

a_{-11}, a_{-13} and a_{-15}). The form of the quadratic terms also explains the quiescence of the l = 1 modes in the first two windows of intermittency (in which the unstable manifold lies exclusively in the l = 0 space).

Integrations have also been carried out using cells of streamwise length 1000 and 2000 wall units and such heteroclinic connections are observed in all the cases. Details of these are given in Aubry and Sanghi (1989).

4.2 The 54 Dimensional Model

The addition of a second non-zero streamwise mode to the previous system (N = 1, $N_1 = 2, N_3 = 5$) leads to a system of 54 ODEs. The properties of the equations are similar to those of the 32 dimensional system. For values of α greater than 2.1, the trivial solution (all modes equal to 0) is the globally attracting solution. For α lying between 2.05 and 2.1 a non-zero fixed point (lying in the l = 0, even k space) is observed. The first two windows of intermittency, whose nature is exactly like the 32 dimensional system, are observed as α is further reduced. The third window of intermittency is seen to occur for α lying between 1.21 and 1.18. In this window all the streamwise modes get excited during the burst. Time series of typical solutions in window III are displayed in figure 4.4. As α is reduced further (down to 0.6), the l = 0 space becomes the globally attractive space again, and the solution shows a complex behavior in the (0,k) space. All non-zero streamwise modes are inactive in this range of α. The window IV of intermittency is observed around α = 0.5 and below this value all the modes are active at all times. This bifurcation behavior is listed in table 4.2.

Similar to the stability analysis in the 32 dimensional dynamical system, the eigenvalues of the Jacobian matrix at the fixed point $a_{02} = -r_2$, $a_{04} = -r_4$ are computed. Linearization of the full system leads to the diagonalization of the 54×54 block matrix as follows: (Re(a_{02}),Re(a_{04})), a 2×2 matrix, (Im(a_{02}),Im(a_{02})), a 2×2 matrix, (Re(a_{01}),

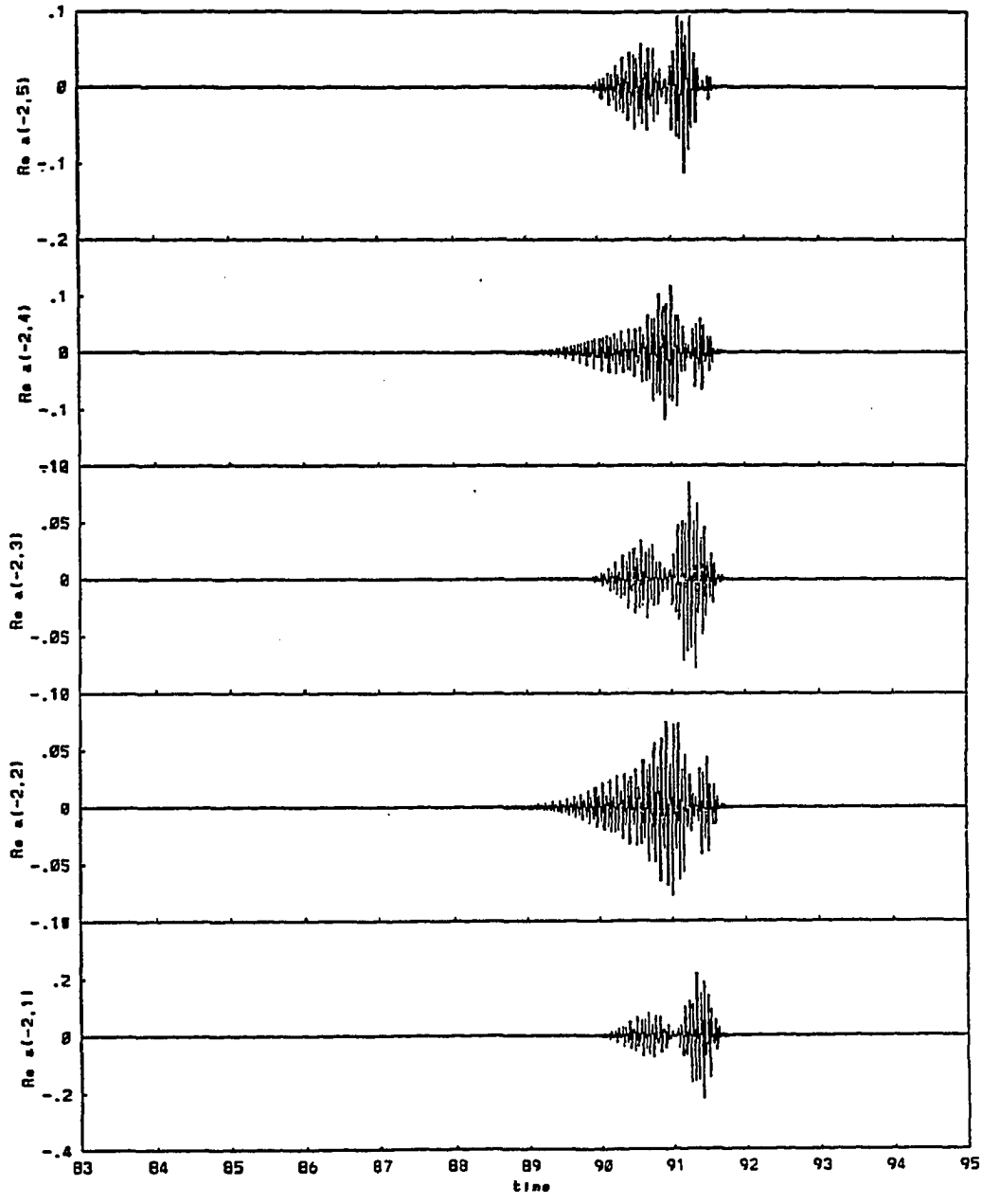

Figure 4.4. Typical solution in the window III of intermittency of the 54 dimensional system. Time series of real parts of a_{-21}, a_{-22}, a_{-23}, a_{-24} and a_{-25} for $\alpha = 1.2$.

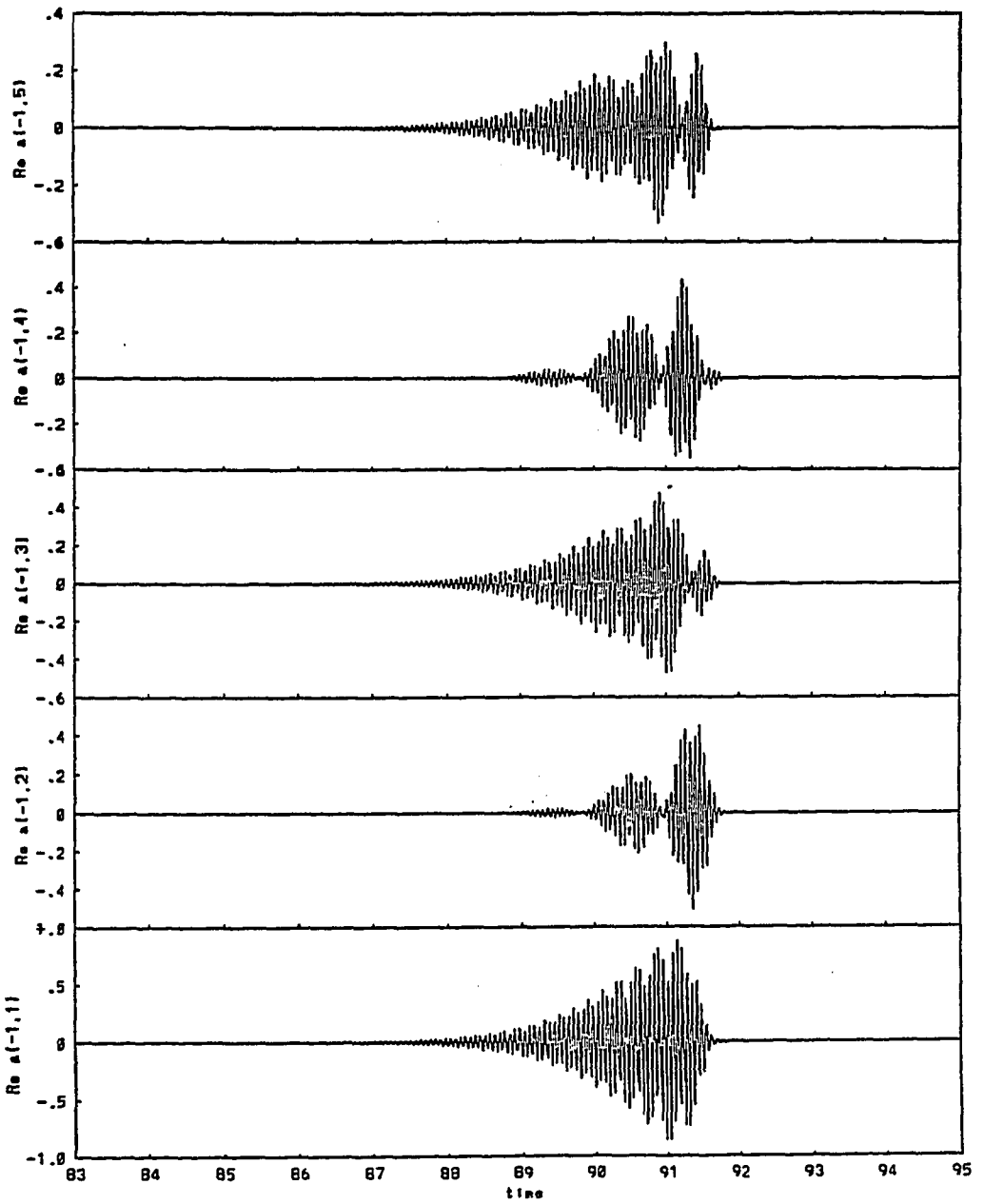

Figure 4.4 (continued). Typical solution in the window III of intermittency of the 54 dimensional system. Time series of real parts of a_{-11}, a_{-12}, a_{-13}, a_{-14} and a_{-15} for $\alpha = 1.2$.

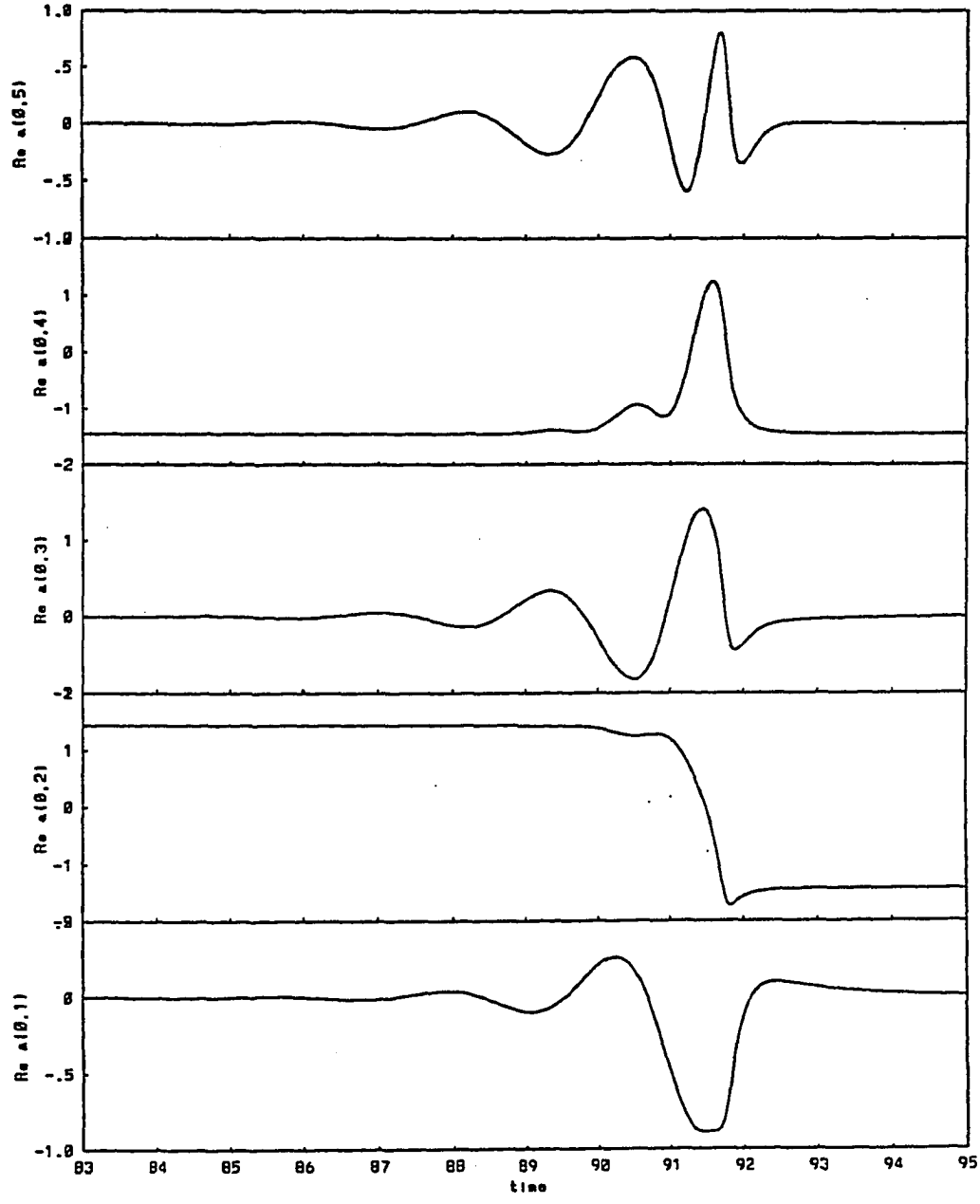

Figure 4.4 (continued). Typical solution in the window III of intermittency of the 54 dimensional system. Time series of real parts of a_{01}, a_{02}, a_{03}, a_{04} and a_{05} for $\alpha = 1.2$.

$\alpha \geq 2.1$	trivial solution: $a_{1,k} = 0\ \forall(l,k)$, is the global attractor.
$2.1 \geq \alpha \geq 2.05$	stable fixed point: $a_{02}, a_{04} \neq 0$, other modes are zero.
$2.04 \geq \alpha \geq 1.84$	intermittency (I) in the $a_{0,k}$ subspace: $a_{1,k} = 0\ \forall k$, $a_{02}, a_{04} \neq 0$; $a_{0,k} = 0$, $\forall k \neq 2, 4$ between bursts. $a_{0,k} \neq 0$, $\forall k$ during bursts (no oscillations).
$1.83 \geq \alpha \geq 1.43$	stable fixed point: $a_{02}, a_{04} \neq 0$, other modes are zero.
$1.42 \geq \alpha \geq 1.22$	intermittency (II) in the $a_{0,k}$ subspace: $a_{1,k} = 0\ \forall k$, $a_{02}, a_{04} \neq 0$; $a_{0,k} = 0$, $\forall k \neq 2, 4$ between bursts. $a_{0,k} \neq 0$, $\forall k$ during bursts (a_{01}, a_{03}, a_{05} oscillate).
$1.21 \geq \alpha \geq 1.18$	intermittency (III) in the full space: $a_{02}, a_{04} \neq 0$; $a_{0,k} = 0\ \forall\ k \neq 2, 4$, between bursts. $a_{l,k} \neq 0\ \forall\ l, k$, during bursts.
$1.15 \geq \alpha \geq 0.6$	complex behavior in the $a_{0,k}$ subspace: $a_{1,k} = 0\ \forall\ k$, $a_{0,k} \neq 0\ \forall\ k$.
$\alpha \cong 0.5$	intermittency (IV) in the full space: complex behavior in the $a_{0,k}$ subspace between bursts. $a_{l,k} \neq 0$, $\forall l, k$ during bursts.
$0.4 \geq \alpha$	complex behavior for all values of $a_{l,k}$.

Table 4.2. Qualitative dynamical behavior in the 54 dimensional system.

$Re(a_{03})$, $Re(a_{05})$), a 3×3 matrix, ($Im(a_{01})$, $Im(a_{03})$, $Im(a_{05})$), a 3×3 matrix, (a_{-12},a_{-14}, a_{10}, a_{12}, a_{14}), a 10×10 matrix, (a_{-11}, a_{-13}, a_{-15}, a_{11}, a_{13}, a_{15}), a 12×12 matrix, (a_{-21}, a_{-23}, a_{-25}, a_{21}, a_{23}, a_{25}), a 12×12 matrix and (a_{-22}, a_{-24}, a_{20}, a_{22}, a_{24}), a 10×10 matrix. As in the 32 dimensional dynamical system, it is observed that the bifurcations, in which the first and second windows of intermittency appear, have an unstable manifold in the ($Im(a_{01})$, $Im(a_{03})$, $Im(a_{05})$) subspace. The third window emerges through a (subcritical) Hopf bifurcation occurring in the (a_{-11}, a_{-13}, a_{-15}, a_{11}, a_{13}, a_{15}) subspace. The eigenvalues of the second non-zero streamwise mode subspace stay negative for all these parameter values (see appendix C for a listing of the eigenvalues). However, numerical integrations show that both the first and the second non-zero streamwise modes burst. It is shown below that the second mode gets activated by nonlinear, quadratic interactions. Let o and e denote the odd and even spanwise modes respectively. The triggering of the $a_{1,e}$ modes was explained in the last section. The quadratic terms in the equation of $a_{2,o}$ have the following combinations:

1. $a_{1,e}\, a_{1,o}$
2. $a_{2,e}\, a_{0,o}$
3. $a_{2,o}\, a_{0,e}$.

So only the first of these can trigger the $a_{2,o}$ mode. The quadratic terms in the $a_{2,e}$ occur in the forms:

1. $a_{1,o}\, a_{1,o}$
2. $a_{1,e}\, a_{1,e}$
2. $a_{2,o}\, a_{0,o}$
4. $a_{2,e}\, a_{0,e}$.

The first two of these activate the $a_{2,e}$ mode. It is then also clear that the $a_{2,e}$ modes get activated before $a_{2,o}$ because the latter require the activation of the $a_{1,o}$ as well as the $a_{1,e}$ modes. This is also seen in figure 4.4

In view of the hierarchy of the instabilities presented above, one can ask whether the higher order streamwise harmonics will burst as well. Experimental visualizations have shown that the sublayer bursting events are characterized by the generation of fine scale turbulence. It is obvious that this cascade of energy towards the finer scales is not limited to two harmonics. The study of the 54 dimensional dynamical system showed that once the first non-zero streamwise mode bursts through a subcritical Hopf bifurcation, the second non zero streamwise mode also bursts by nonlinear interactions. Would higher harmonics be triggered in the same manner? Examination of the quadratic terms shows that all the $l = 2$ modes are destabilized by the $l = 1/l = 1$ interactions for example. In the same way, the $l = 3$ modes are destabilized by the $l = 1/l = 2$ interactions, the $l = 4$ modes are destabilized by the $l = 1/l = 3$ and $l = 2/l = 2$ interactions, etc. So even for systems where N_1 greater than 2, with a fixed point solution whose unstable manifold lies in the $l = 0$ and $l = 1$ space only, all the higher streamwise Fourier modes will get activated.

4.3 Models with 2 Normal Modes

So far, the systems with a variable number of streamwise and spanwise modes but only one eigenmode have been considered. A study of the robustness of the intermittency mechanism will not be complete if systems with more than 1 normal modes are not analyzed. In the discussion below the modes are denoted by $a(n, l, k)$ or $a^{(n)}_{l,k}$.

In this investigation, detailed solutions are presented for the set of ODEs truncated with $N = 2$, $N_1 = 1$ and $N_3 = 5$. This leads to a 64 dimensional dynamical system. The non-zero streamwise mode corresponds to $L_1 = 667$. For large values of α (greater than 1.9) a zero solution is observed from which a fixed point in the (n,0,2)/(n,0,4) space bifurcates. This behavior is seen for values of α from 1.8 to 1.7. As α is reduced from 1.6 to 0.9 a fixed point is observed in the (n,0,k) space. For lower α values (between 0.8

excited and trigger the bursts. Solutions stay in the neighborhood of fixed points in the zero streamwise subspace before and after bursting. Since this intermittency resembles the third window of intermittency of the previous solutions (activated by the non-zero streamwise modes), it is referred to in the same manner. Typical solutions in this window of intermittency are shown in figure 4.5. For the values of α between 0.2 and 0.3 solutions similar to the fourth window of intermittency in the systems discussed above are found. Time series for some of the coefficients depicting this behavior are shown in figure 4.6. The details of the bifurcation behavior are given in table 4.3. Similar results were obtained from a 64 dimensional dynamical system derived from the numerical data for the channel flow (Moin and Moser, 1989).

$\alpha \geq 1.9$	trivial solution: $a_k^n = 0, \forall(n,l,k)$ is the global attractor.
$1.8 \geq \alpha \geq 1.7$	stable fixed point: $a_{0,2}^n$, $a_{0,4}^n \neq 0 \; \forall$ n, other modes are zero.
$1.6 \geq \alpha \geq 0.9$	stable fixed point: $a_{0,k}^{(n)} \neq 0 \; \forall$ (n,k), other modes are zero.
$0.8 \geq \alpha \geq 0.6$	Intermitttency (III) in the full subspace: $a_{0,k}^{(n)} \neq 0$, $\forall$ (n,k), between bursts. $a_{l,k}^{(n)} \neq 0$, $\forall(n,l,k)$ during bursts.
$0.5 \geq \alpha \geq 0.4$	complex solution: $a_{l,k}^{(n)} \neq 0$, $\forall(n,l,k)$.
$0.3 \geq \alpha \geq 0.2$	intermittency in the full space similar to IV window in the 32D model: complex behavior in the $a_{0,k}^{(n)}$ subspace $\forall$ (n,k), between bursts. $a_{l,k}^{(n)} \neq 0$, $\forall(n,l,k)$ during bursts.
$0.2 \geq \alpha$	complex solution: $a_{l,k}^{(n)} \neq 0$, $\forall(n,l,k)$.

Table 4.3. Qualitative dynamical behavior in the 64 dimensional system.

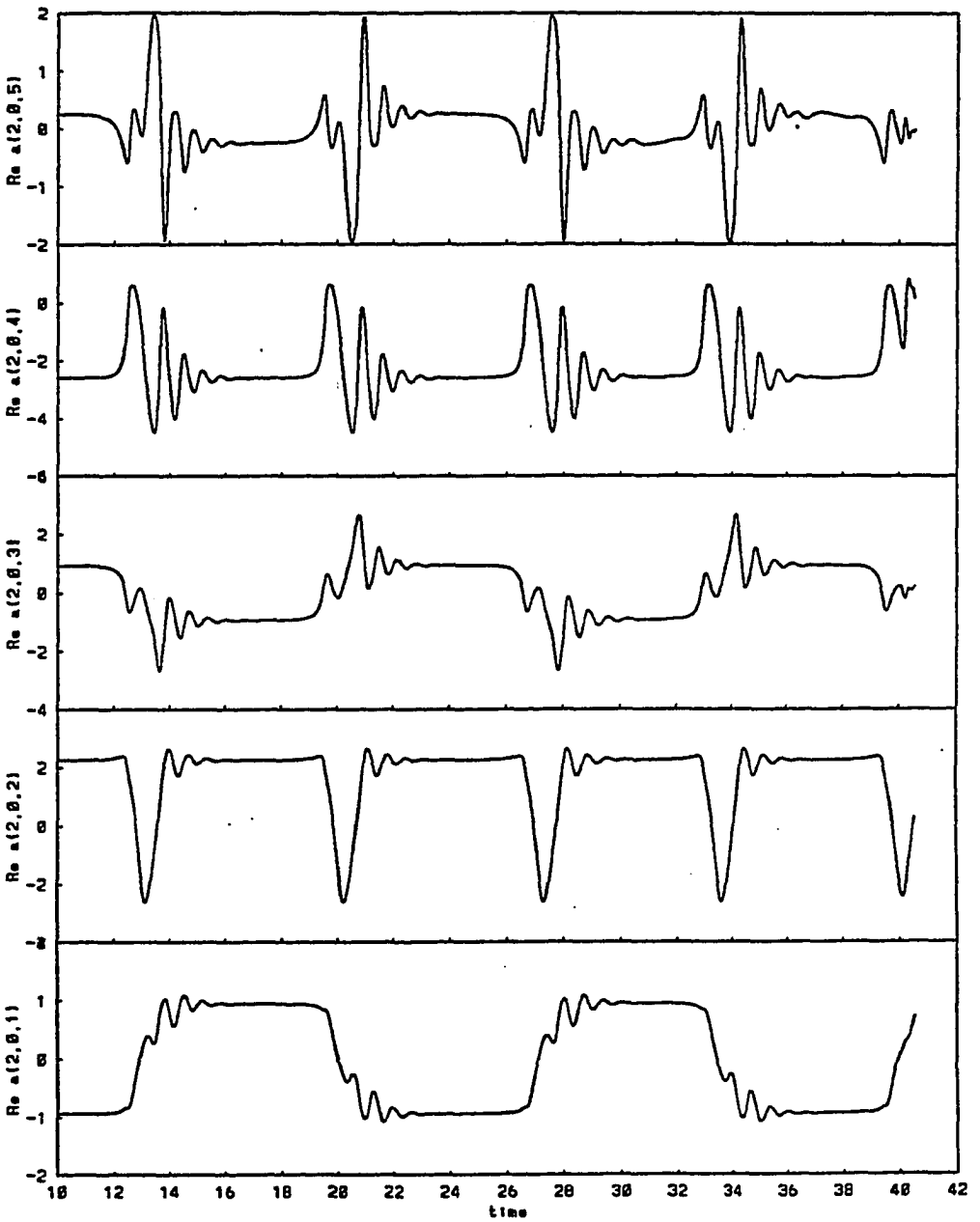

Figure 4.5. Typical solution in the window III of intermittency of the 64 dimensional system. Time series of the real parts of $a^2_{0,k}$ (k = 1,2,3,4 and 5) for α = 0.6.

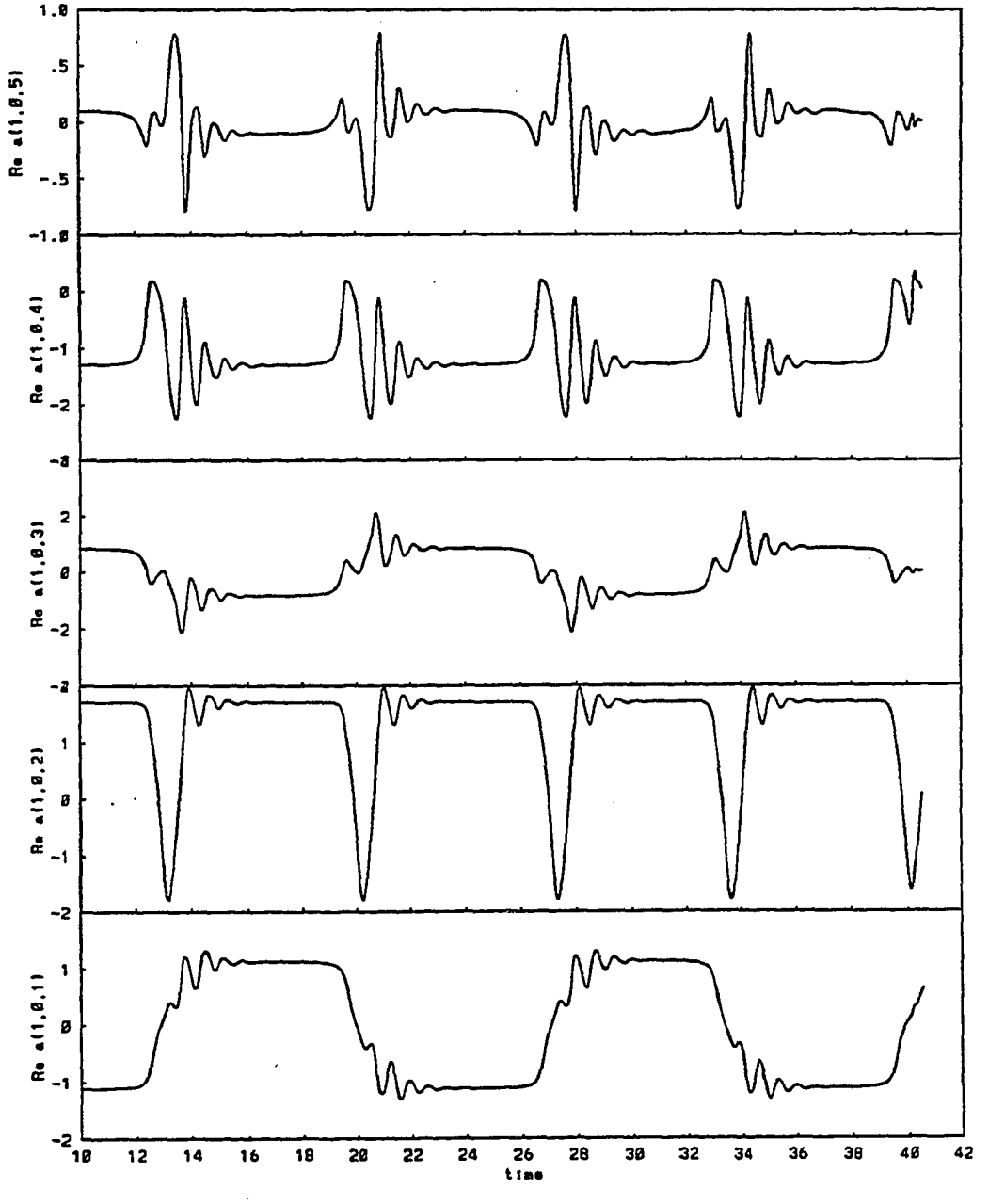

Figure 4.5 (continued). Typical solution in the window III of intermittency of the 64 dimensional system. Time series of the real parts of $a^1_{0,k}$ (k = 1,2,3,4 and 5) for α = 0.6.

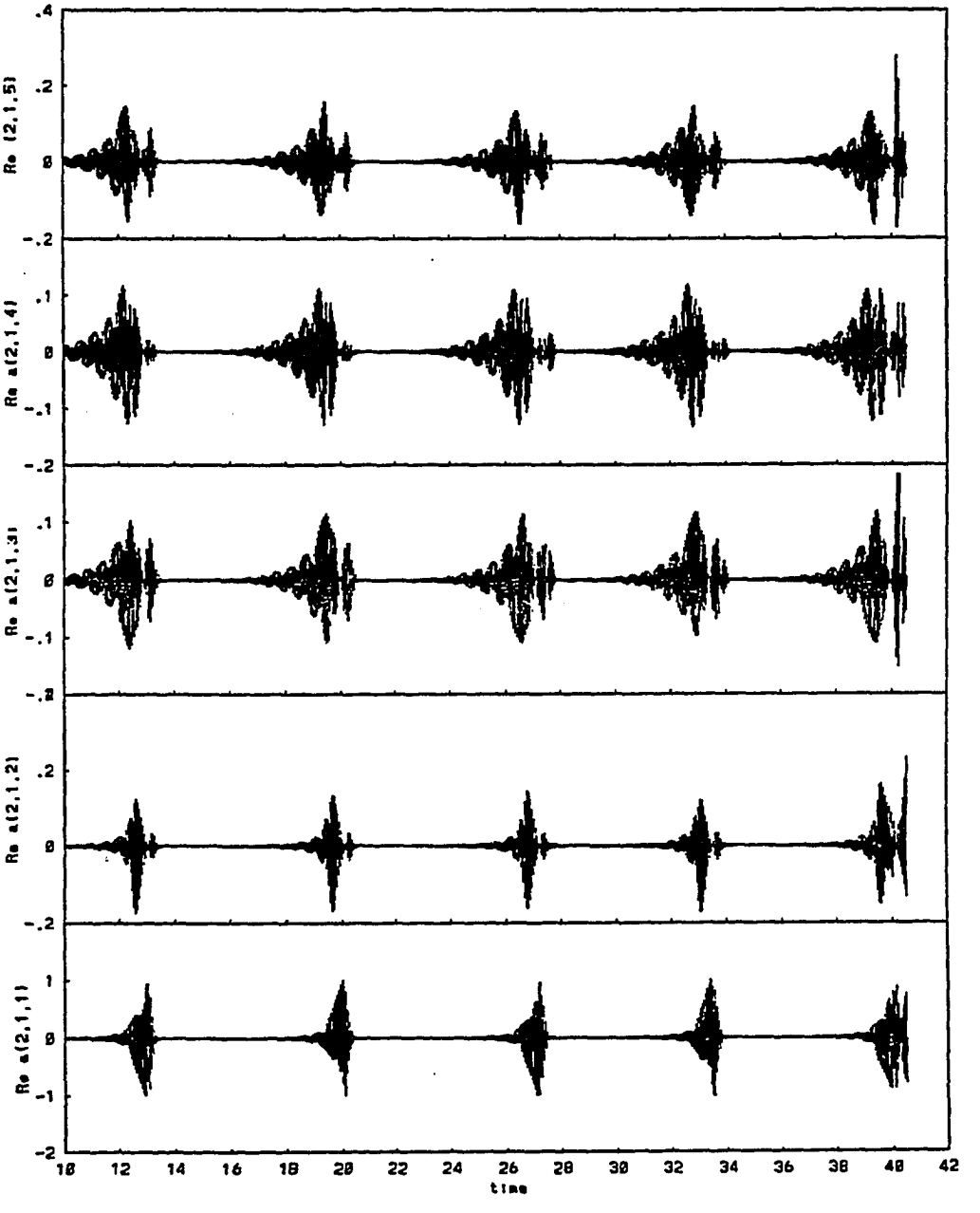

Figure 4.5 (continued). Typical solution in the window III of intermittency of the 64 dimensional system. Time series of the real parts of $a^2_{1,k}$ (k = 1,2,3,4 and 5) for $\alpha = 0.6$.

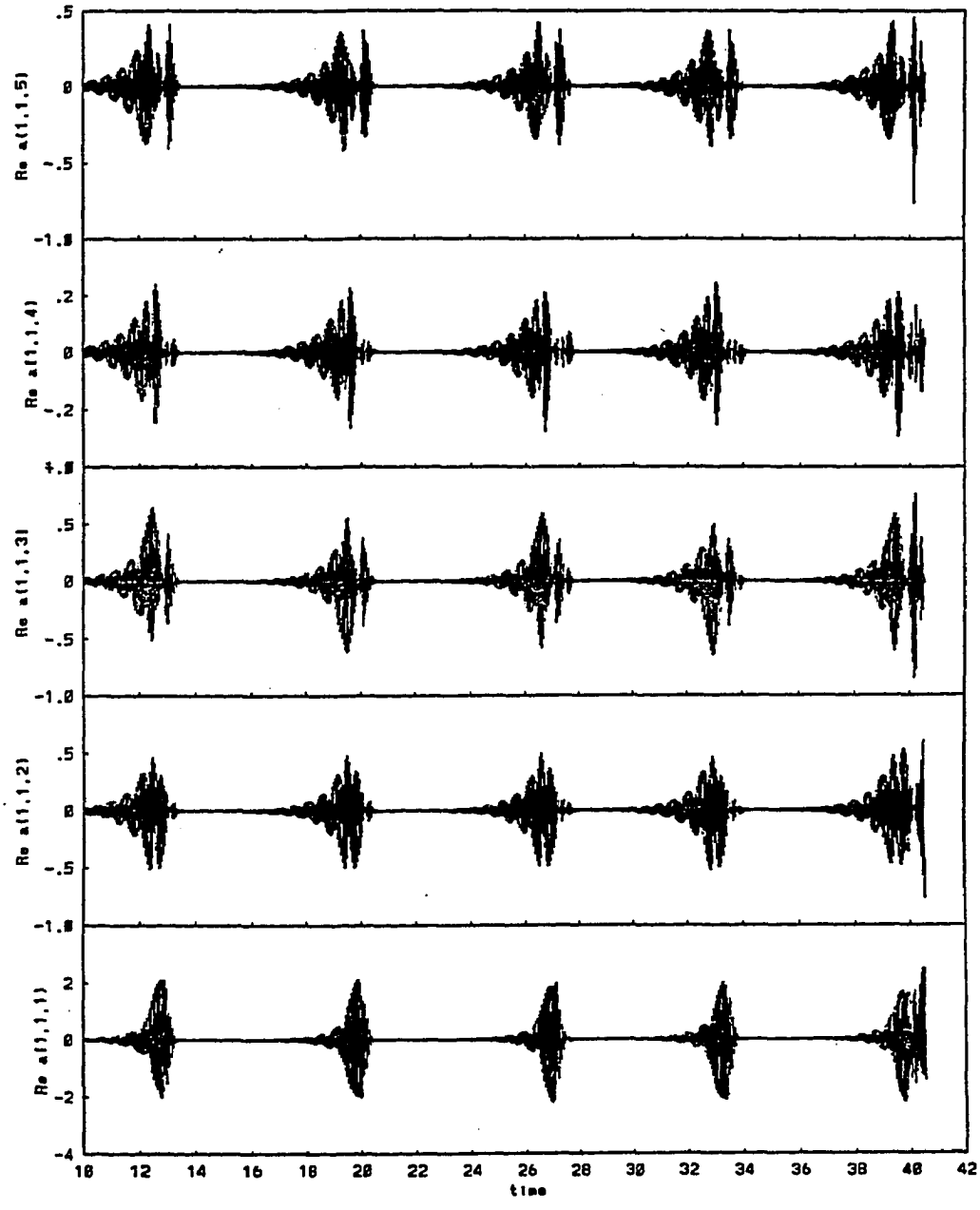

Figure 4.5 (continued). Typical solution in the window III of intermittency of the 64 dimensional system. Time series of the real parts of $a^1_{1,k}$ (k = 1,2,3,4 and 5) for α = 0.6.

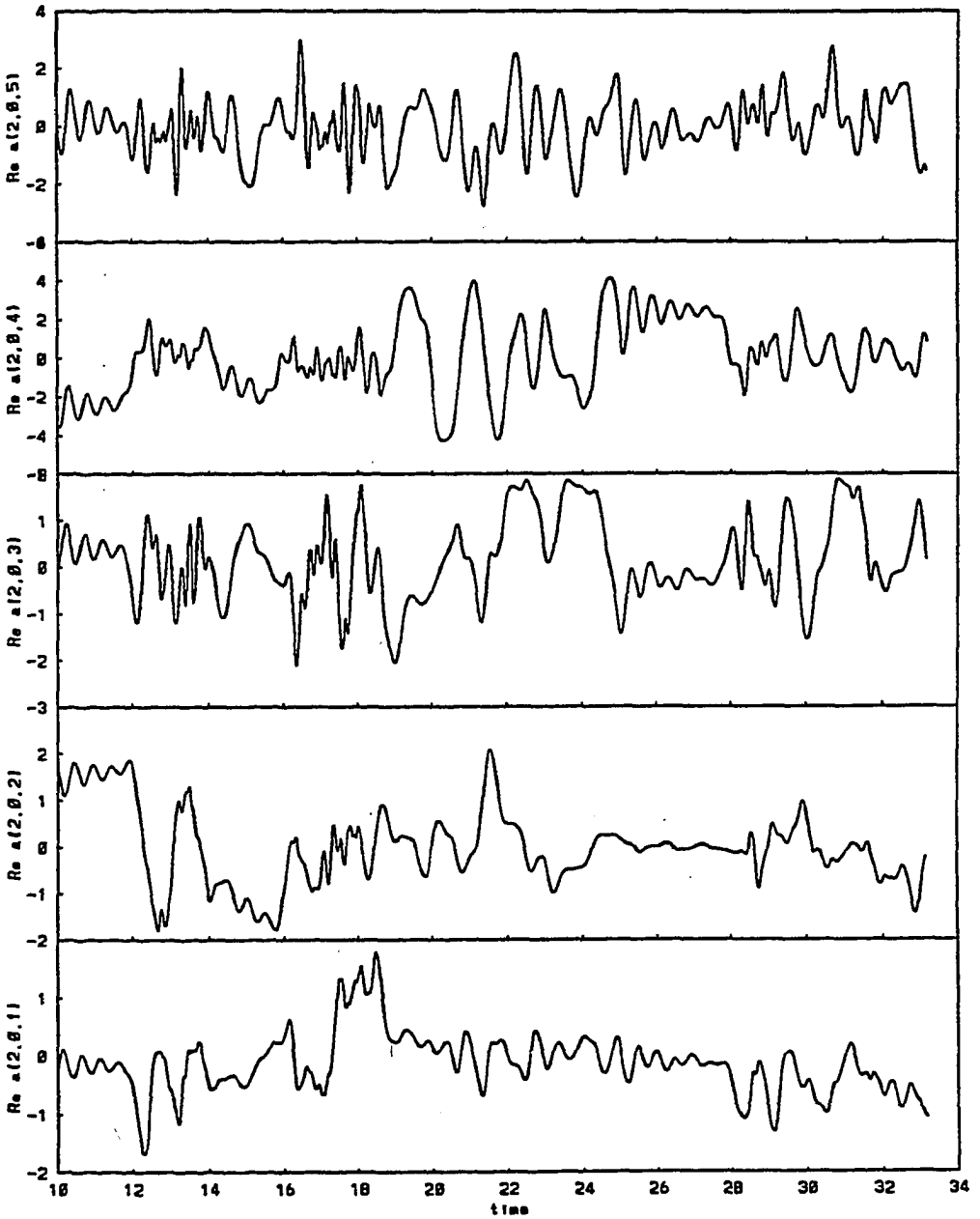

Figure 4.6. Typical solution in the window IV of intermittency of the 64 dimensional system. Time series of the real parts of $a_{0,k}^2$ (k = 1,2,3,4 and 5) for α = 0.3.

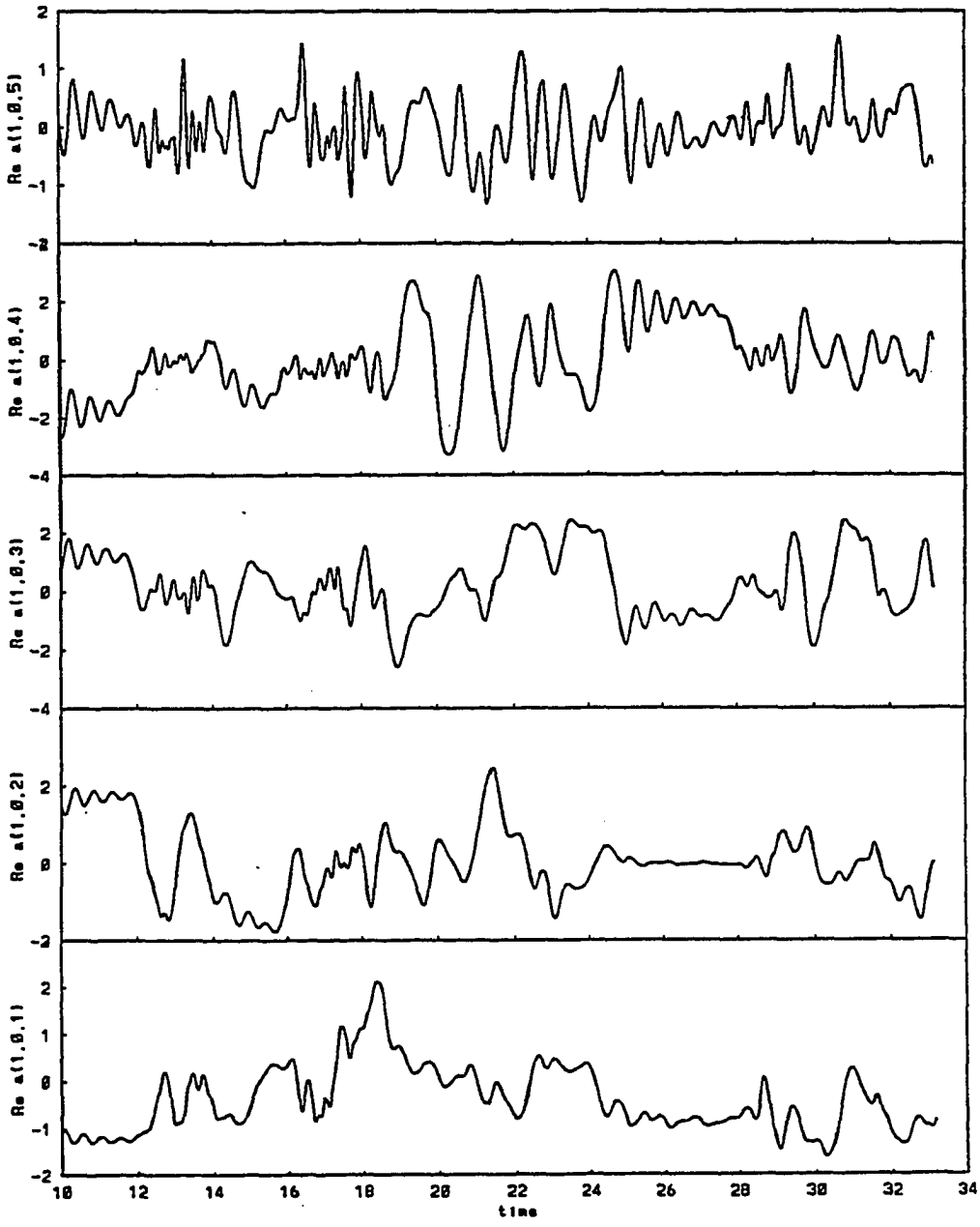

Figure 4.6 (continued). Typical solution in the window IV of intermittency of the 64 dimensional system. Time series of the real parts of $a^1_{0,k}$ (k = 1,2,3,4 and 5) for α = 0.3.

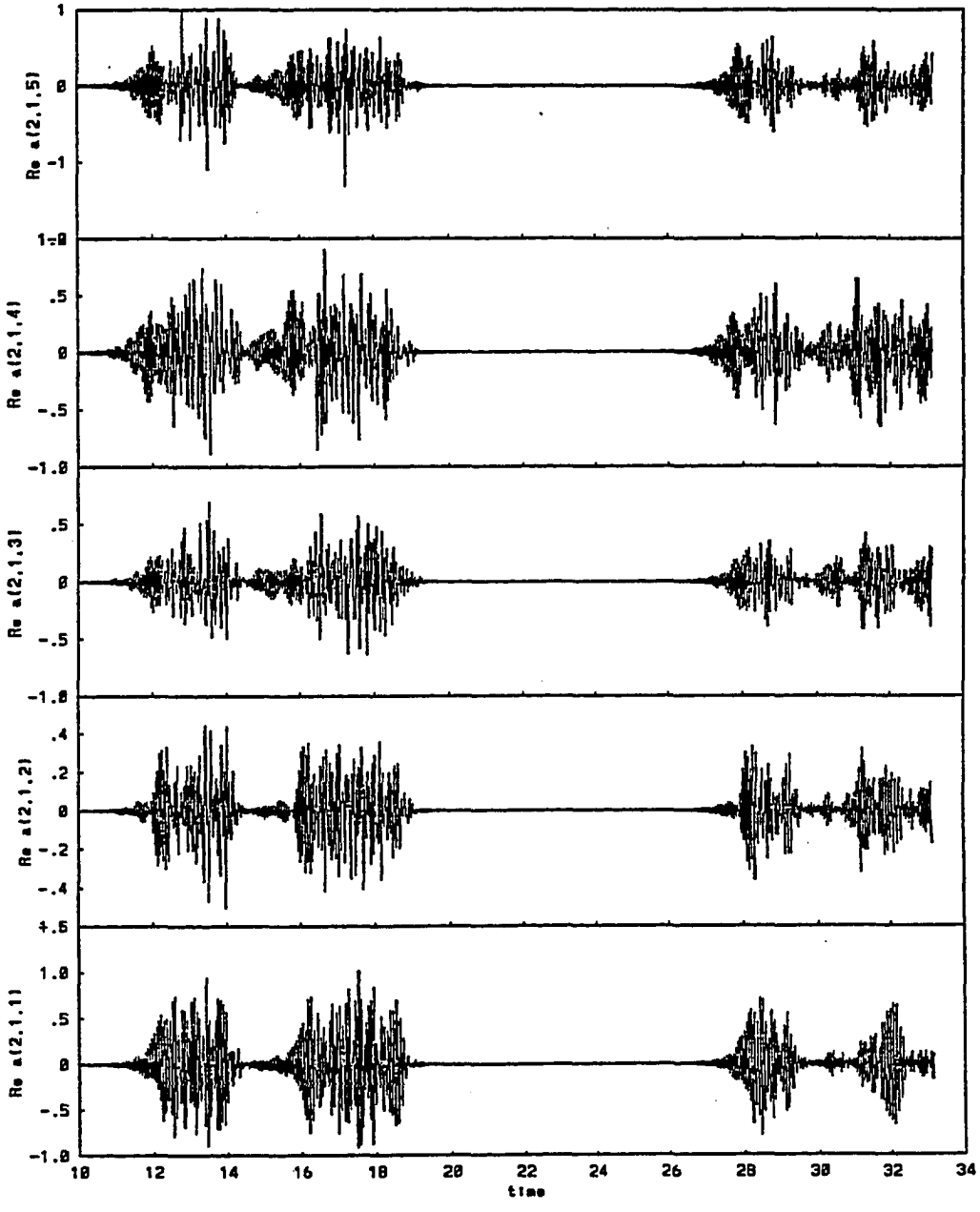

Figure 4.6 (continued). Typical solution in the window IV of intermittency of the 64 dimensional system. Time series of the real parts of $a^2_{1,k}$ (k = 1,2,3,4 and 5) for α = 0.3.

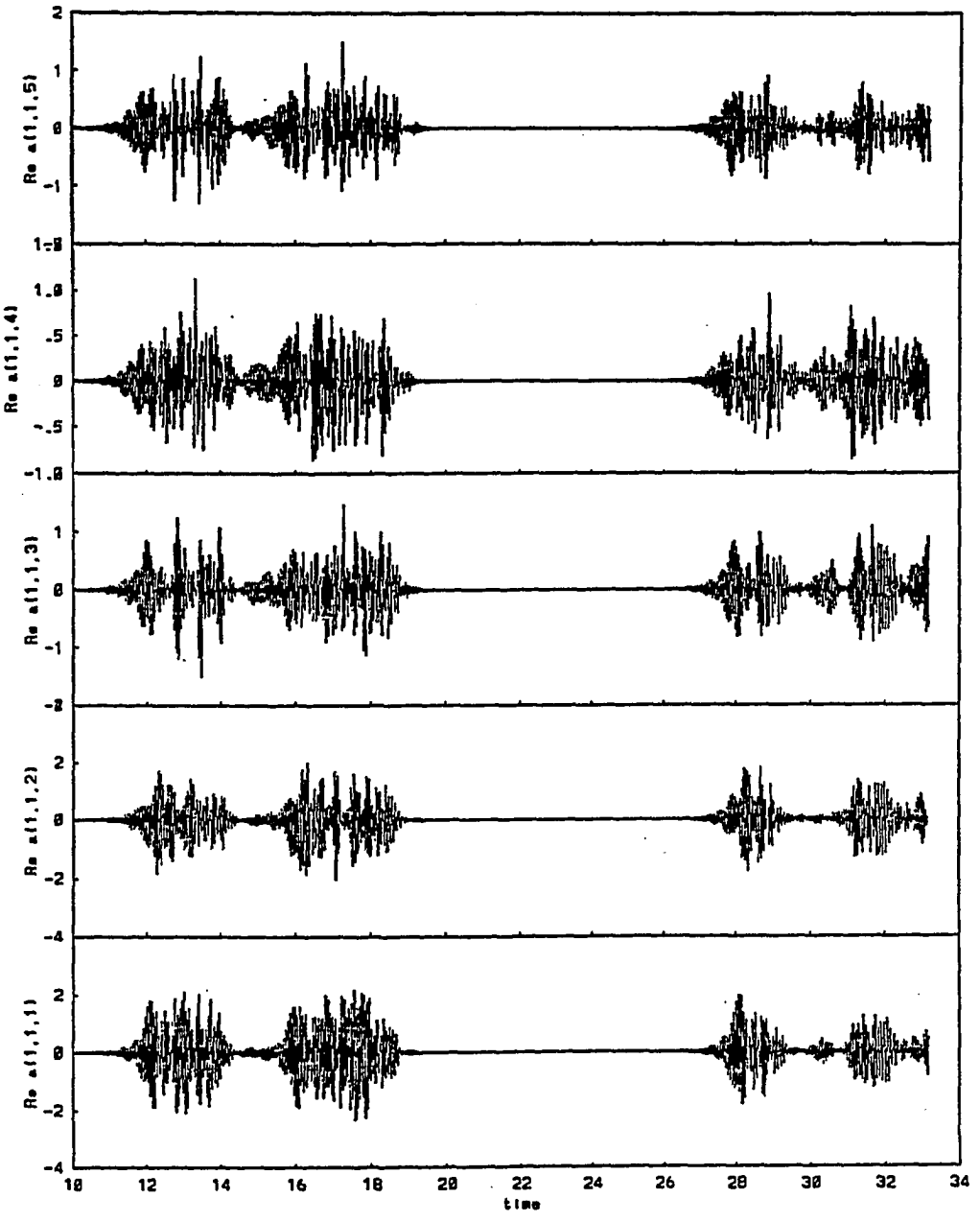

Figure 4.6 (continued). Typical solution in the window IV of intermittency of the 64 dimensional system. Time series of the real parts of $a^1_{1,k}$ (k = 1,2,3,4 and 5) for α = 0.3.

Integrations have also been carried out for a simpler system with $N = 2$, $N_1 = 0$ and $N_3 = 5$ (20 dimensional system) using both, the experimental and the numerical data and heteroclinic connections between the fixed points (analogous to the 10D model) are also found in this system.

4.4 Conclusions

It is now clear that the intermittent behavior displayed by the 10D dynamical system of Aubry *et al.* (1988) in which streamwise variations were neglected persists as non zero streamwise Fourier modes are included. As the bifurcation parameter (which adjusts the loss of energy towards the unresolved modes) decreases, four types of intermittency are observed. For large parameter values, the system displays intermittent behavior in the zero streamwise mode subspace only. As in the 10D system of Aubry *et al.* (1988), infinitely long streamwise rolls burst in the cross-stream direction. For lower values of the parameter, intermittency is observed in the full space so that streamwise modes, mostly inactive, get excited during the explosion events, resulting into a streamwise burst in the physical space. The fourth window of intermittency occurs as the parameter decreases further, showing that the motions in the zero streamwise subspace are not necessarily close to a fixed point but can already be of a more complex, i.e.turbulent nature. There is thus no doubt that in this dynamical system intermittency is generic. It is identified with the presence of a heteroclinic cycle connecting saddles. In the first three windows, these saddles are fixed points; in the fourth window, they are more complex (apparently chaotic) manifolds. A linear stability study of the fixed points in the first three windows proved that intermittency appeared through clearly identified bifurcations. In the first window, the stable fixed point becomes unstable with one dimensional unstable manifold. In the second window, the stable fixed point becomes unstable through a subcritical Hopf bifurcation in the (a_{01},a_{03},a_{05}) subspace with two dimensional unstable manifold. In the third window,

the already unstable fixed point gains additional unstable directions through a (subcritical) Hopf bifurcation in the (a_{-11}, a_{-13}, a_{-15}, a_{11}, a_{13}, a_{15}) subspace. The unstable manifold of the fixed point becomes four dimensional. The excitation of the higher Fourier modes occurs through (quadratic) non linearities for this range of the parameter α.

The quasi-steadiness of the rolls motions between the bursts is, of course, the result of the extreme simplicity of the model. Undoubtedly, a fully developed turbulent flow cannot be steady, even for small periods of time, but keeps fluctuating randomly. The fourth type of intermittency shows that this more realistic situation also appears in the model: The velocity field is apparently chaotic, involving only a certain number of scales and suddenly bursts into even more complex behavior involving the totality of the modes included in the model. Here, the orbit connects apparently chaotic, globally unstable regimes.

Chapter 5

Physical Interpretation

In this chapter the kinematics and dynamics of the coherent structures are studied. Structures of different types have been been extensively described from both visualization experiments and direct numerical simulations. However, the connection between these structures is still not well understood and highly questioned. It is shown that all the structures which have been previously reported are present in the truncated models developed in this investigation. Moreover, due to the low dimensionality of the system, the connection between the structures becomes rather clear. First the fixed point solutions are described and the presence of the basic structures in these type of solutions is established. This corresponds to a kinematical description of a very simplistic flow field. Then, in section 5.2, the attention is focussed on both the temporal and spatial distribution of the structures by studying the solutions during a burst. In section 5.3 of this chapter, criteria to fix the optimum value of the eddy viscosity parameter are developed. The variation of first and second order statistical quantities with the distance from the wall is plotted and compared with the experimental data of Eckelmann (1974). Concluding remarks on physical interpretation of the solutions are presented in the last section. All the solutions discussed in this chapter are based on the data from the 32 dimensional system discussed in Chapter 4.1. All the quantities are non-dimensionalized by the wall variables.

5.1 Structures in a Fixed Point Solution

The fixed point represents a steady solution which does not vary in the streamwise direction. This behavior is, therefore, much simpler than the actual flow behavior but this simplistic solution is used to extract information about the different type of structures and their relationships. The classification presented in the world-wide survey of Kline and Robinson (1989) is followed. Only the first five categories are referred to in the present investigation as the others seem to have been observed by a few researchers only or are not relevant to this work (outer structures, for example).

Figure 5.1 shows a vectorial plot of the instantaneous velocity components u_2 and u_3 in a cell of dimension 40 × 333 lying in the x_2-x_3 plane. Two pairs of counter rotating rolls, with the region in between the rolls lying at $x_3 = 0$ and $x_3 = 167$, are observed. The rolls observed in this simplistic solution are symmetric and always occur in pairs. Different type of coherent structures are located with respect to these rolls.

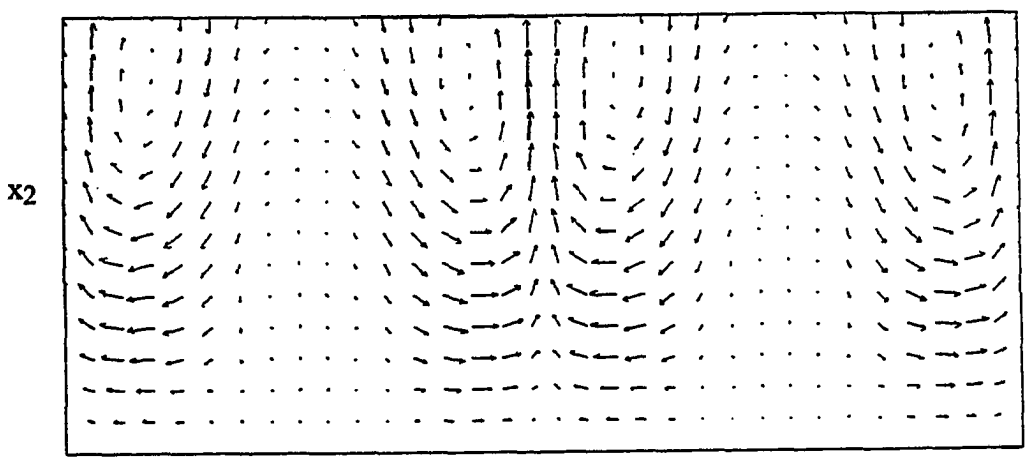

Figure 5.1. Vector representation of u_2-u_3 in an (x_2-x_3) plane during a fixed point region of the solution for $\alpha = 0.87$. The spanwise and normal dimensions of the box are 333 and 40 wall units respectively.

5.1.1 Low Speed Streaks in the Region $x_2 < 10$

Streaks are streamwise filaments of low speed, outward moving (away from the wall) fluid observed in the near-wall region. They were first reported by Hama (Corrsin 1956), who noted that when dye was injected into a sublayer through a small slit in the wall, the marking agent became concentrated into narrow regions of low velocity. Runstadler *et al.* (1963) quantified and correlated the mean spacing between the streaks. Since then, many researchers working in the field have examined this phenomenon. As it has been stated before, there are a lot of issues regarding the coherent structures in the turbulent boundary layer on which there is no agreement in the community. However, one subject, on which there is a consensus, is the average spanwise spacing of the low speed streaks which has been found to be about 100 wall units (Oldaker and Tiederman 1977, Achia and Thompson 1976, Lee, Eckelmann and Hanratty 1974, Blackwelder and Eckelmann 1979, Kreplin and Eckelmann 1979, Nakagawa and Nezu 1981, Sreenivasan 1989). Smith and Metzler (1983) have shown that the probability distribution function of the low speed structure around the mean value of 100 wall units is log-normal and has a typically dense range of 60 to 180 wall units. The low speed streaks have a speed about half the local mean speed. They are not straight but are observed to meander in the spanwise direction and their spanwise width varies from 30 to 50 wall units.

To locate the slow, outward moving streaks the profiles of the mean and instantaneous streamwise velocity, U and $\tilde{u}$, as a function of x_3 (at $x_2 = 2.8$) are plotted in figure 5.2. Figure 5.3 shows the normal velocity, u_2, as a function of x_3 (the other parameters are the same as in figure 5.1). It is observed that the regions of low u_1 occur at $x_3 = 0$ and $x_3 = 166$. These are also the locations where u_2 is maximum and hence constitute the low speed streaks. They appear in figure 5.1 as the narrow region in between the rolls, which is slow moving and has normal velocity in the outward direction. The spanwise extent of these streaks is observed to be about 30 viscous lengths.

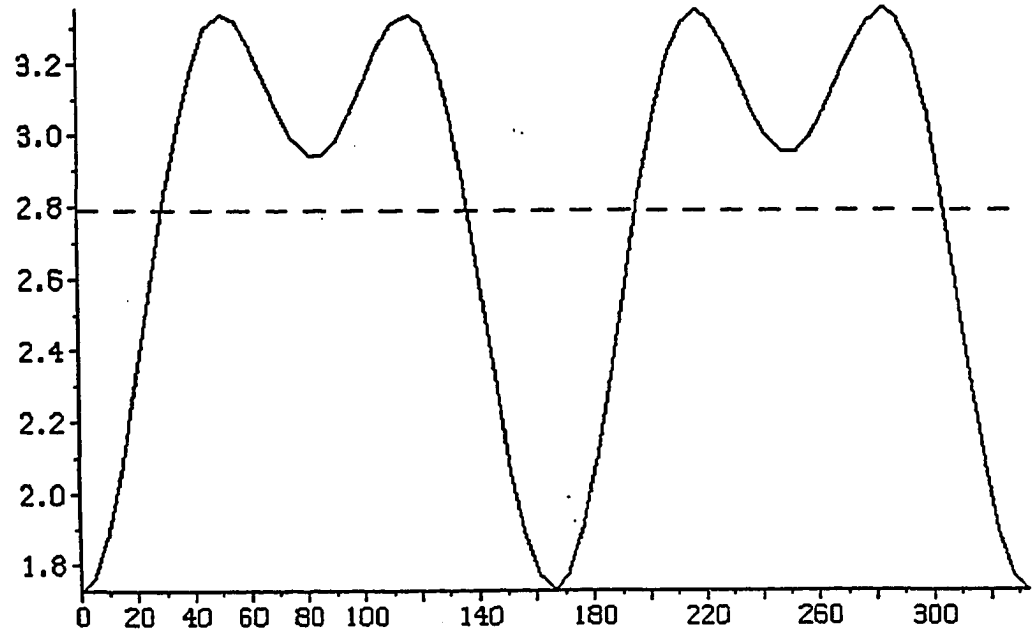

Figure 5.2. Distribution of the streamwise velocity, mean (U) - - - - - and instantaneous ($U+u_1$) ——, as a function of x_3 at $x_2 = 2.8$ for the fixed point solution ($\alpha = 0.87$).

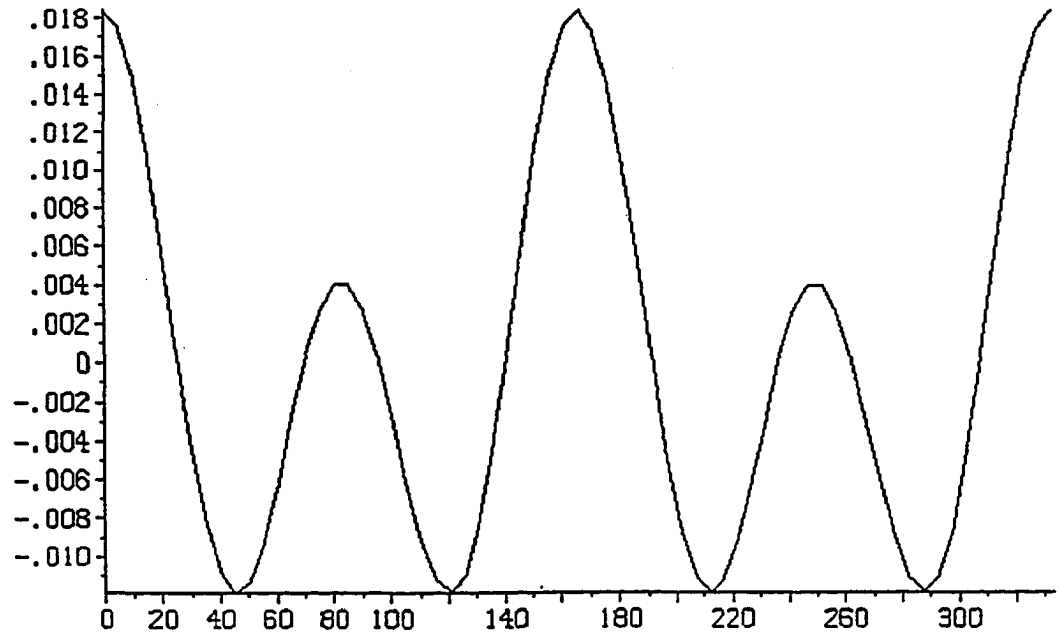

Figure 5.3. Distribution of the normal velocity u_2 as a function of x_3. All other parameters are the same as that for figure 5.2.

5.1.2 Ejections

The low speed streaks in the sublayer migrate outwards as they move in the streamwise direction and then they move far more rapidly away from the wall in ejection motions which have been termed as lifting (Kim *et al.* 1971, Corino and Brodkey 1969, Willmarth and Lu 1972, Smith and Metzler 1983). Kim *et al.* (1971) coined the term 'bursting' which was defined as the process during which the streaks lift away from the wall, oscillate and breakdown causing a rapid appearance of finer scales of motion suggestive of locally high values of turbulence production. The lifted low-speed streaks are observed in the region $10 < x_2 < 40$ and are the primary contributors to the Reynolds stress in the region $x_2 > 12$.

The regions of ejections are located in figure 5.1 in between the rolls directly above the sublayer streaks, where strong outward motions are observed. However, the streamwise component of the velocity cannot be seen in this figure. In figures 5.4 and 5.5, the streamwise and normal velocity components are presented as a function of x_3 at $x_2 = 38.5$.

It is still not clear if the near-wall streaks are dynamically important. Kline and Robinson (1989) point out: "Many workers believe that the streak structure in the very near-wall region is dynamically important. However, others believe that the streaks are passive and therefore not a significant factor in turbulence production." The simplistic solution of rolls seems to suggest that the ejections and the near-wall streaks are a part of the same structure - they are the ends of rolls which move away from the wall.

This picture of the streaks lying in between the rolls is not a new one. Blackwelder and Eckelmann (1979) used a quadrant probability analysis to deduce that pairs of counter-rotating streamwise vortices occur frequently in the wall region. They conjectured that the defect region which occurred in between the vortices forms the low-speed streak.

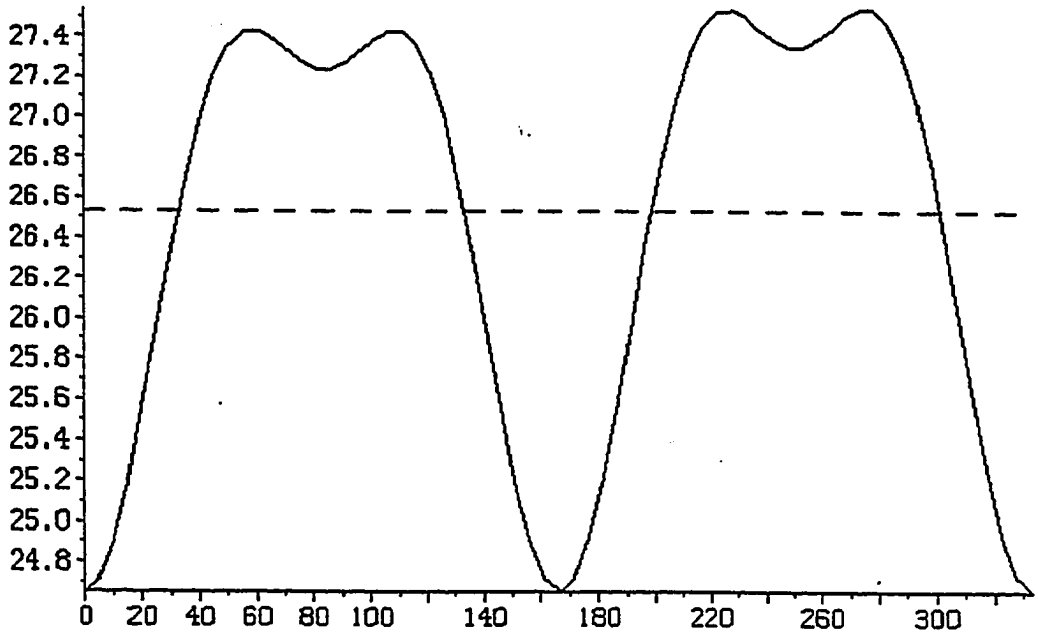

Figure 5.4. Distribution of the streamwise velocity, mean (U) - - - - - and instantaneous (U+u) ——, as a function of x_3 at $x_2 = 38.5$ for the fixed point solution.

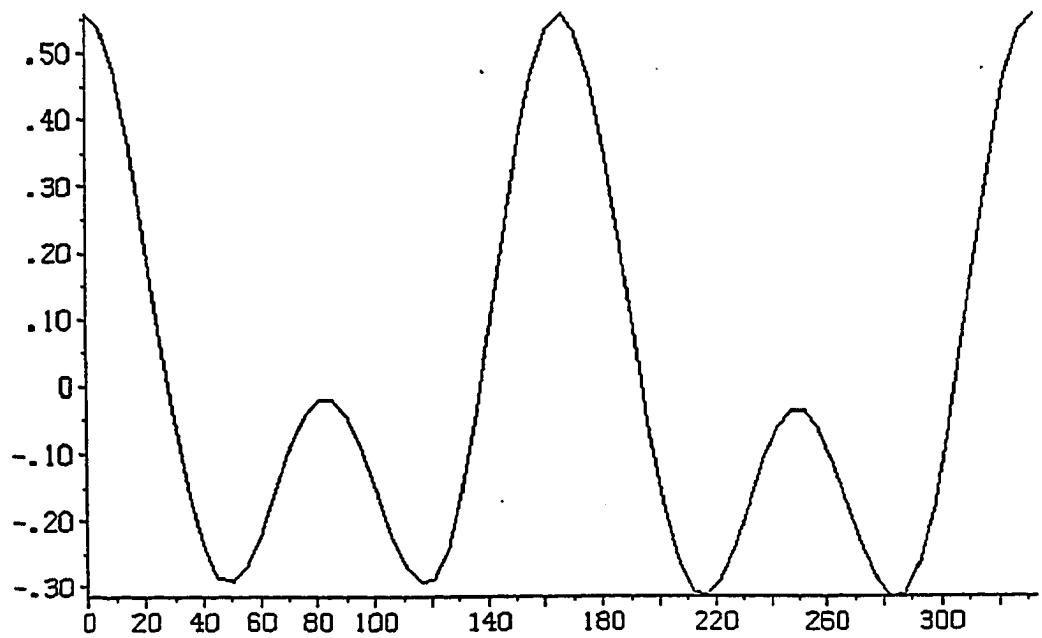

Figure 5.5. Distribution of the normal velocity u_2 as a function of x_3. All other parameters are the same as that for figure 5.4.

5.1.3 Sweeps of High Speed Fluid towards the Wall

Flow visualizations do not clearly show wallward sweeps of high speed fluids. Their presence can, however, be inferred from the continuity equation (see for example Corino and Brodkey 1969, Grass 1971). It is well established (Willmarth and Lu 1972, Wallace *et al.* 1972, Brodkey *et al.* 1974, Kim *et al.* 1987) that the sweeps are the major contributors to the Reynolds stress in the region very close to the wall ($x_2 < 12$). Like the streaks, these regions are also elongated in the streamwise direction but have a relatively larger spanwise dimension.

It is clear from figures 5.1, 5.4 and 5.5, that the outer regions of the rolls where fluid is coming towards the wall have an excess streamwise velocity compared to the mean, thus constituting the sweeps. It is also observed that the sweep regions occupy more spanwise space as compared to the streaks.

The picture of rolls, in the framework of sweeps and streaks, can be described as alternate regions of elongated patterns of fluid having high and low streamwise momentum,which is akin to the description given by Gupta *et al.*(1971).

5.1.4 Vortical Structures

A variety of views exists regarding different types of vortices and a significant portion of the boundary layer literature is devoted to detect and characterize the vortical structures. One major point of controversy is the definition of a vortex acceptable to all. Robinson *et al.* (1989) define the existence of a vortex by a mapping of instantaneous streamlines on a plane, normal to the core, which exhibits a circular or spiral pattern when viewed from the reference frame moving along with the center of the vortex core. This definition is circuitous, because in order to determine the reference frame, one needs an a priori identification of the vortex. Some researchers use contours of vorticity components

or enstrophy to study vortical structures (Moin and Kim 1982, Jiminez and Moin 1991). Complex eigenvalues of the deformation rate tensor (Chong *et al.* 1990, Hunt *et al.* 1988) and elongated regions of low pressure (Robinson *et al.* 1989) have also been suggested as means to infer the presence of vortices. Another popular method is the plotting of vorticity lines (Moin and Kim 1985). In this investigation the last method has been used. Another point which needs to be specified is whether the structures are obtained from ensemble averaged patterns or individual realizations, because ensemble averaged patterns will not be necessarily present in each realization.

Vortical structures fall in two broad categories. The first of these is the horseshoe or hairpin shaped structures. While Theodorsen (1952) was probably the first to suggest their existence in a conceptual model developed from the vorticity-transport form of the Navier-Stokes equations, Head and Bandyopadhyay (1981) established their presence in the boundary layer flows with the help of flow visualization experiments. Acarlar and Smith (1987) provided qualitative support for the hypothesis that the hairpin vortices form a characteristic structure in the boundary layer. More recently, Smith and Lu (1989) extended this hypothesis using template matching techniques to identify the hairpin structures. Moin and Kim (1982) obtained direct evidence for the existence of such structures using the direct numerical simulation database. The temporal evolution of a horseshoe vortex structure has been studied by Kim (1987). On the other hand, several teams of workers have inferred the existence of streamwise vortices in the near-wall region. The streamwise vortices are to be seen as nearly circular patterns in the streamlines in an x_2-x_3 plane. Bakewell and Lumley (1967) and Blackwelder and Eckelmann (1979) used different statistical techniques (the POD and two-point space-time correlations of hot wire data) to establish their existence. Smith and Schwartz (1983), using crossed bubble wire markers in an x_2-x_3 plane, showed that the streamwise vortices do not occur in the region below $x_2 < 10$, but are centered in the buffer layer ($10 < x_2 < 30$). The inferences based on the ensemble averages suggest that the streamwise vortices are continuously present in time

but the data of Smith and Schwartz (1983) based on individual realizations, indicates that they are present at a given point only intermittently. Robinson *et al.* (1989) believe that the predominant vortical structures in the near-wall region are the quasi-streamwise vortices.

Most of the earlier studies of the streamwise vortices were based on the ensemble averaged studies, which prescribe a spanwise symmetry and hence, it was widely believed that these vortices existed as counter-rotating pairs. Simulations and experimental data from realizations, however, show that they occur singly more often than in pairs (Moin 1987, Guezennec *et al.* 1989). Recent studies have also suggested that the hairpin shaped structures may also be predominantly one-sided (hook shaped) rather than symmetrical (Moin and Kim 1985, Robinson *et al.* 1989). In this investigation, the simplistic fixed point solutions (which show the spanwise symmetry) indicate the presence of symmetric counter-rotating streamwise vortices, but the time-varying solutions (during the bursting periods in the simpler windows of intermittency and at all times in the fourth window) show that asymmetric pairs and single vortices are also present (next section).

The roll shaped structures which are observed in the cross stream plane (figure 5.1) are indicative of the streamwise vortices. The shape of the vorticity lines in this picture in the region of the pair of counter-rotating rolls can be deduced by kinematical arguments. The vorticity due to the mean velocity has a contribution only in the spanwise component, $-U_{,2}$. The spanwise gradient of the streamwise velocity, which is the only contributing term to the normal vorticity in the fixed point solution, is negative in the left roll and positive in the right. In both the vortices, spanwise vorticity, which is dominated by the mean velocity gradient, is negative. This simple argument implies that the vorticity lines corresponding to a pair of counter-rotating rolls has a horseshoe shape with its head lying in between the rolls. This is seen in figure 5.6 where a perspective view of vortex lines starting at same x_1 and x_3 locations is shown. A comparison with figure 5.1 shows that the tip of the horseshoe lies in the region in between the rolls. The symmetry of the rolls by reflection through an x_1-x_2 plane accounts for the symmetry of the horseshoe. If the rolls are not

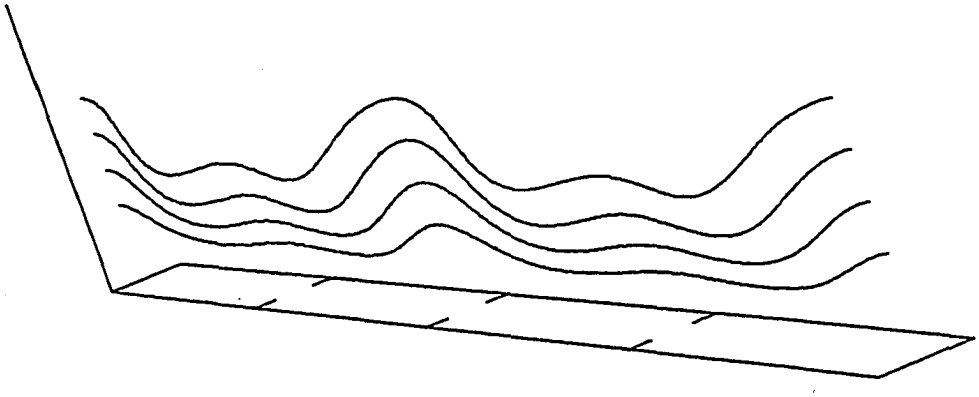

Figure 5.6. Vortex lines displaying the vortical structure for a fixed point regime of the solution at $\alpha = 0.87$. This is the perspective view of a three dimensional field. The box shown in the figure shows a portion of the lower wall of the channel.

symmetrical then the corresponding horseshoe will also be asymmetrical. In particular, when a roll is isolated then the vortex line will have a 'hook like' shape.

Another method of studying the relative importance of vorticity as compared to the extensional shear has been developed by Dresselhaus and Tabor (1989), who coined the term persistence of strain, denoted by σ^2, for the second invariant of the rate of deformation tensor, $u_{i,j}$. They showed that in the regions of vorticity domination, where the individual particles tend to tumble up, σ^2 is negative, whereas in the zones, where the flow tends to extend the particles, this quantity is positive. This has applications in the theory of turbulent drag reduction, where drag reduction due to the addition of polymer particles is attributed to their stretching in the buffer zone (Lumley 1977). An analysis of the fixed point solution reveals that in the ejection region in between the rolls the flow is highly extensional, as opposed to the center of the rolls, where it is highly vortical. In

terms of the horseshoe, its tip is the extensional zone and the legs in the 'tumbling' zone. In the viscous sublayer ($x_2 < 10$), it is found that σ^2 is very close to zero, which indicates that most of the extension takes place only in the buffer layer in the regions in between the rolls (in agreement with Lumley's theory).

5.1.5 Near-Wall Shear Layers

Shear layers with a normal and spanwise gradient of streamwise velocity have been reported by workers using various methods. While Corino and Brodkey (1969) used flow visualization techniques, Kreplin and Eckelmann (1979) and Johansson *et al.*(1987) used probe based results to establish their presence. The VITA technique has also been used to detect changes in the streamwise velocity (see for example Bogard and Tiederman 1987). Jiminez *et al.*(1988) used the contours of spanwise vorticity in the numerically simulated channel flow to establish that the near-wall region is dominated by intense three-dimensional shear layers. Blackwelder and Swearingen (1989) focussed their attention on the presence of the streamwise vortices near the wall and compared them with the Gortler vortices next to a concave wall. They argued that these vortices are the cause of the inflection points in the U(z) profile.

The presence of rolls in the solution leads to both vertical and horizontal shear layers. While the former comes from the juxtaposition of slow and fast moving fluid (streaks and sweeps) in the spanwise direction (see figures 5 and 7), the latter originates in the presence of the change of streamwise velocity as a function of the distance from the wall: a clear inflection point occurs in the sweep region where there is a sharp interface between the fluid very close to the wall and the fluid slightly away ($x_2 > 15$) which gets accelerated because of the sweep.

5.1.6 Concluding Remarks on the Structures

The results from the fixed point solution indicate a one to one correspondence between the various structures previously identified in the turbulence literature. Streamwise rolls, streaks, sweeps, horseshoe shaped vortical structures in the near-wall region and the shear layers are all the same structure. It is speculated, based on the information given above, that the ejection of the fluid from the near-wall region originates in the quasi-streamwise vortices and is a result of the kinematics of the flow. However, the streamwise vortices interact, move, break or reform because of the dynamics. This leads to a displacement of the ejection region. The ejections can themselves become weaker or stronger depending on whether the rolls move closer to or further away from each other. These results also explain the observation (Moin 1987) that the sweeps and ejections tend to occur in a side-by-side orientation rather than the sweep occurring directly upstream of an ejection, as suggested by some structural models. This picture of ejections and sweeps being produced by the streamwise vortices does not change when they occur singly and not in counter-rotating pairs.

5.2 Structures in Time Evolving Solutions

Until now, the structure of the flow has been described according to the steady solution of the model, which is simply a pair of reflection symmetric rolls. When the flow gains some dynamics, as of course it does in real turbulence, observation of the temporal evolution of velocity vectors in a cross section of the flow shows that the reflection symmetry is often broken (instantaneously but not statistically). Then the structures are very similar to those previously described, the main difference being that the rolls appear isolated or in asymmetric pairs also. Figure 5.7 shows instantaneous velocity vectors in the cross stream plane for a series of time steps. The solutions correspond to a value of α

= 0.2 in a period in between the bursts (the $l \neq 0$ modes are not activated) during the fourth window of intermittency. In this case, rolls are not symmetric but they are still accompanied by sweeps, streaks and three dimensional shear layers. Perhaps, the most significant change is that inclined vorticity lines which become half horseshoes or hook like structures in the case of one roll, asymmetric horseshoes in the case of two asymmetric rolls. The one to one relation of structures which has been established in the case of symmetric rolls is still valid. Many interesting phenomena can be seen in this series of streamline patterns. The spanwise locations marked as A and B, are in the region of ejections and streaks in the first 5 time steps with a pair of counter-rotating streamwise rolls lying in between them. After this, these two streaks start to move closer to each other and by the time step t = 8, they merge. Such phenomenon of streak merging has been reported by Smith and Metzler (1983). Another interesting sequence of events can be observed at the spanwise location C. For the first few time steps this region is in the sweep location but from the step t = 8 onwards, the sweep region divides, moving into opposite spanwise directions. A pair of rolls is formed at this location and at the end of the sequence there is an ejection and a streak at the spanwise location C.

Figure 5.8 shows a plot of instantaneous streamwise velocity at the spanwise location A of figure 5.7 for the first 9 time steps. The dotted line indicates the mean velocity profile at the first time step. For the first few steps the region A is in the ejection zone and so the instantaneous velocity is less than the mean, but at later times, it is in sweep region and is clear from the shape of the velocity profile.

This picture of near wall region structures, however, is not complete since it does not explain finite streamwise structures as observed in numerical simulations. For this, the more realistic solution, which does depend on time and displays streamwise variations, is investigated. The intermittent solution during a burst in the fourth window of intermittency as previously described is studied.

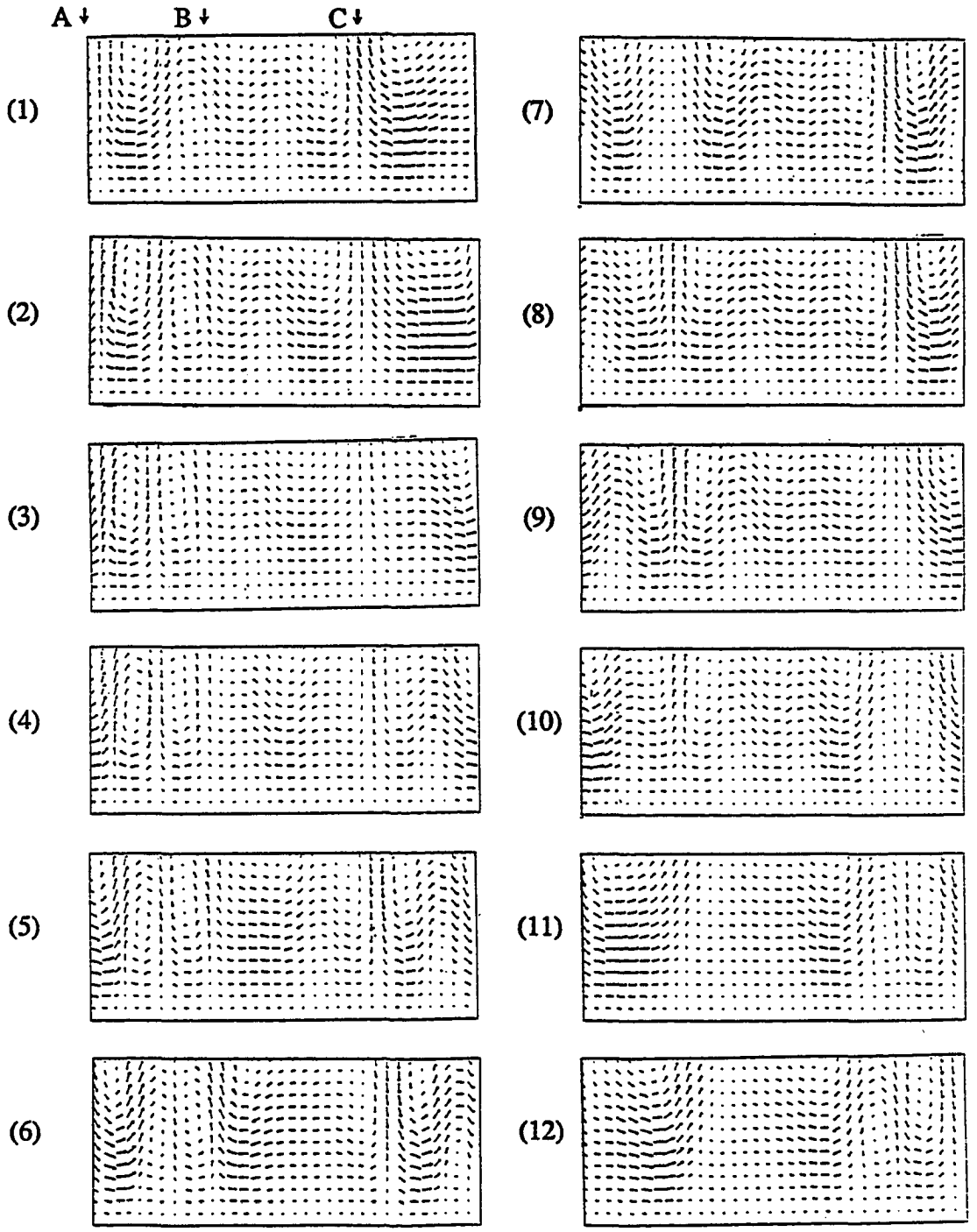

Figure 5.7 Time evolution of vector representation of u_2-u_3 in an (x_2-x_3) plane during the "quiescent" period of the IV window of intermittency. For box dimensions see figure 5.1. The numbers indicate subsequent time steps, $\Delta t = 0.08$ (in wall units).

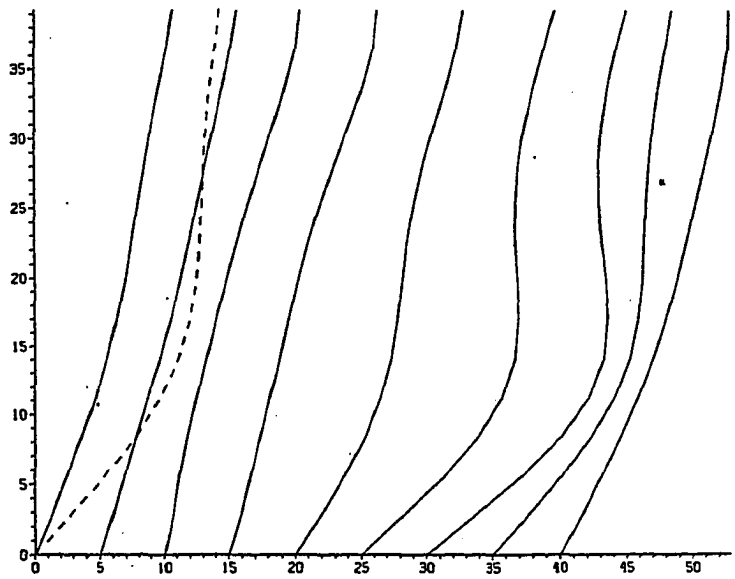

Figure 5.8 Profiles of the instantaneous streamwise velocity as a function of x_2 at the spanwise location A and for the time steps from 1 to 9 in figure 5.7. The dotted line represents the mean velocity profile.

Contours of the streamwise velocity fluctuations in an x_1-x_3 plane near the wall (x_2 = 2.8) are shown in figure 5.9. As expected, the pattern consists of elongated structures (the near-wall streaks). They have a length (in the streamwise direction) of about 500 wall units and a width (in the spanwise direction) of nearly 40 wall units. This plot resembles those obtained by other researchers (for example Moin and Kim 1982). In figure 5.10 perspective view of vortex lines for a box, corresponding to the region of ejection are shown. Vortex lines starting at the same x_2 and x_3 locations but at different x_1 locations are drawn. As expected, it is observed that the vorticity lines have the shape of a horseshoe. This pattern is very similar to the one reported by Kim and Moin (1986) and Kim (1987). Contours of spanwise vorticity in an x_1-x_2 plane, representing the lower part of a shear layer structure growing from the wall, are presented in figure 5.11. This is very similar to the picture obtained by Jiminez *et al.* (1988).

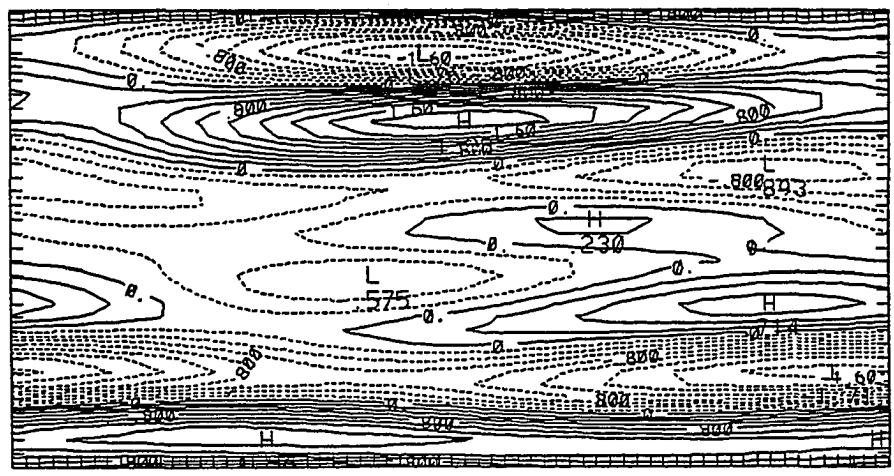

Figure 5.9. Contours of u_1 in an $(x_1\text{-}x_3)$ plane located at $x_2 = 2.8$, for a solution in the IV window of intermittency when all the modes are activated. The streamwise and spanwise dimensions of the box are 666 and 333 wall units respectively. The dotted lines represent values less than zero.

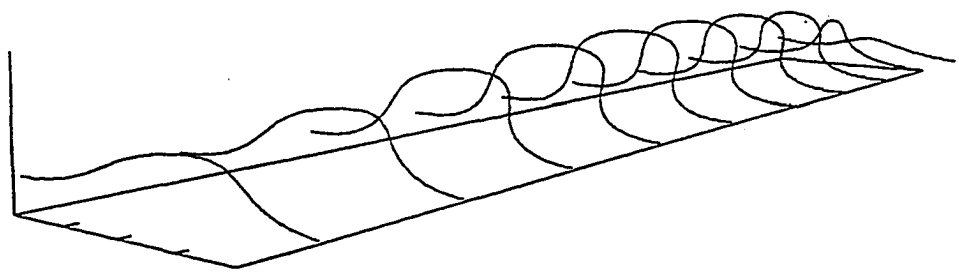

Figure 5.10. Vortex lines displaying the vortical structure during the IV window of intermittency when all the modes are excited. This is the perspective view of a three dimensional field. The box shown in the figure represents a portion of the lower wall of the channel. The mean flow direction is from lower left to upper right. The streamwise, spanwise and normal dimensions of the box are 450, 100 and 40 wall units respectively.

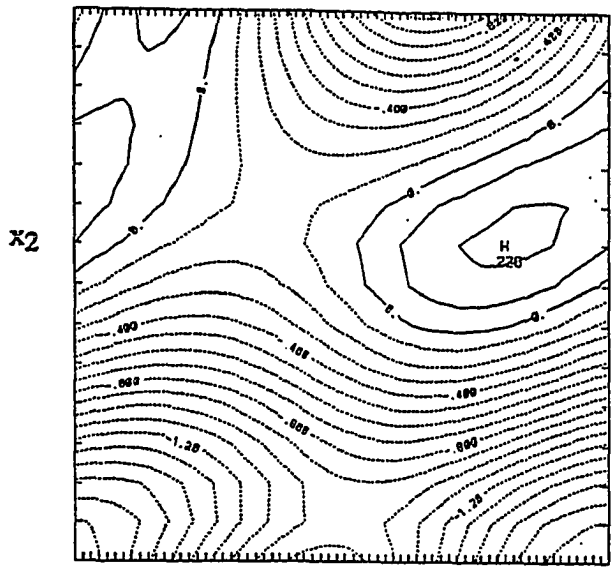

Figure 5.11. Contours of spanwise vorticity in an x_1-x_2 plane located at $x_3 = 250$, for a solution in the fourth window of intermittency ($\alpha = 0.2$) when all the modes are activated. The streamwise and normal dimensions of the box are 666 and 40 respectively.

The effect of the activation of the streamwise modes in the window IV of intermittency on the turbulence production, $-\langle u_1 u_2 \rangle U_{,2}$, is studied by calculating this term as a function of time. The Reynolds stress and the mean velocity gradient are computed by averaging over the homogeneous directions. In figure 5.12, the real parts of coefficients a_{03} and a_{-13} and the production term at $x_2 = 14$ are plotted as a function of time. It is observed that during the periods when the streamwise modes are activated turbulence production stays at higher values for a relatively longer times compared to the periods when the streamwise modes are not activated. While the theoretical maximum value of this term is 0.25, its average value at $x_2 = 14$ (in figure 5.12) is 0.203, which is in good agreement with the data presented in Kim *et al.* (1971).

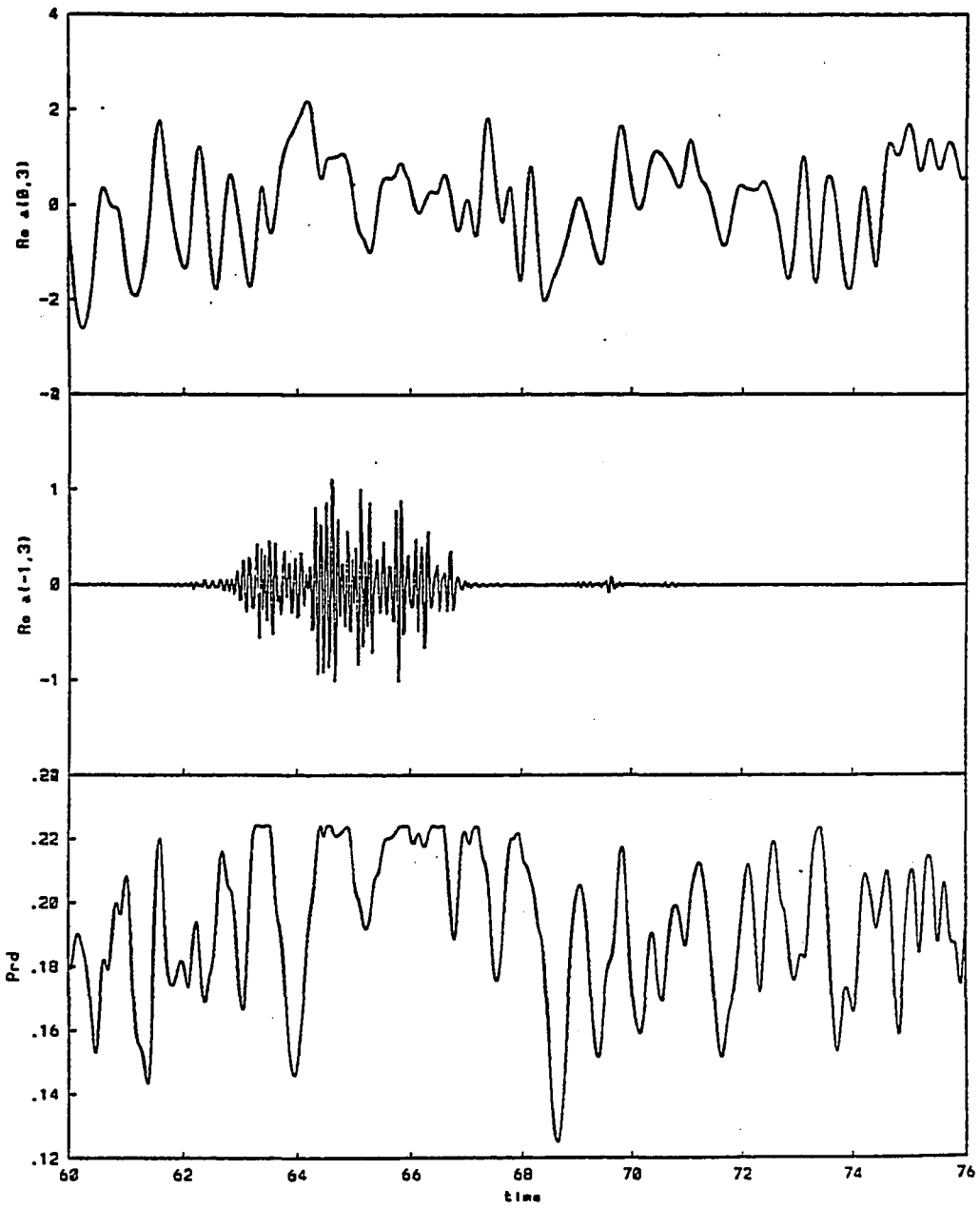

Figure 5.12. Real parts of a_{03} and a_{-13} and turbulence production (- $\langle u_1 u_2 \rangle U_{,2}$) at x_2 = 14 for the 32 dimensional system ($\alpha = 0.2$) as a function of time.

5.3 Optimum Value of α

In the last two sections solutions for various values of α (the parameter representing the loss of energy to the unresolved modes) have been presented. The issue is: which of these solutions represents the correct velocity field? As seen from the physical interpretation, it is clear that the solutions in the fourth window of intermittency represent much more realistic velocity fields than the fixed point solutions. In this section criteria are presented for approximately choosing the appropriate value of α. The analysis is a posteriori in the sense that it is carried out after obtaining the solutions for different values of α for a given truncation.

The kinetic energy (based on the velocity fluctuations and integrated over the entire spatial domain) of the solutions computed at various values of α are studied. The exclusion of the small scales in these truncated models has two opposite effects on the energy of the system. If the energy is calculated by summing over the eigenvalues of the resolved modes, then it is observed that in the 32 dimensional system this value is about 70 percent of the total energy (the remaining fraction is contained in the neglected modes). On the other hand, in a turbulent flow the viscous dissipation takes place through the small scales. When the flow is approximated by a set of truncated equations without any small scale modelling, the computed solutions contain too much energy.

The ratio of the energy contained in the solution of a truncated system for a particular value of α and the total energy of the flow, which is defined as f, is calculated. In figure 5.13, f is plotted as a function of α. It is observed that the value of f is unity when α lies between 0.1 and 0.2.

There is another criterion which the correct solutions must satisfy. Equation (2.11) specifies an condition that the coefficients $a_k^{(n)}(t)$ are uncorrelated. Recall that the eigenfunctions, $\phi_{i_k}^{(n)}(x_2)$, are derived from the experimental or numerical data for the velocity field $u_i(x,t)$. If the set of the coefficients $a_k^{(n)}(t)$ is obtained by taking an inner

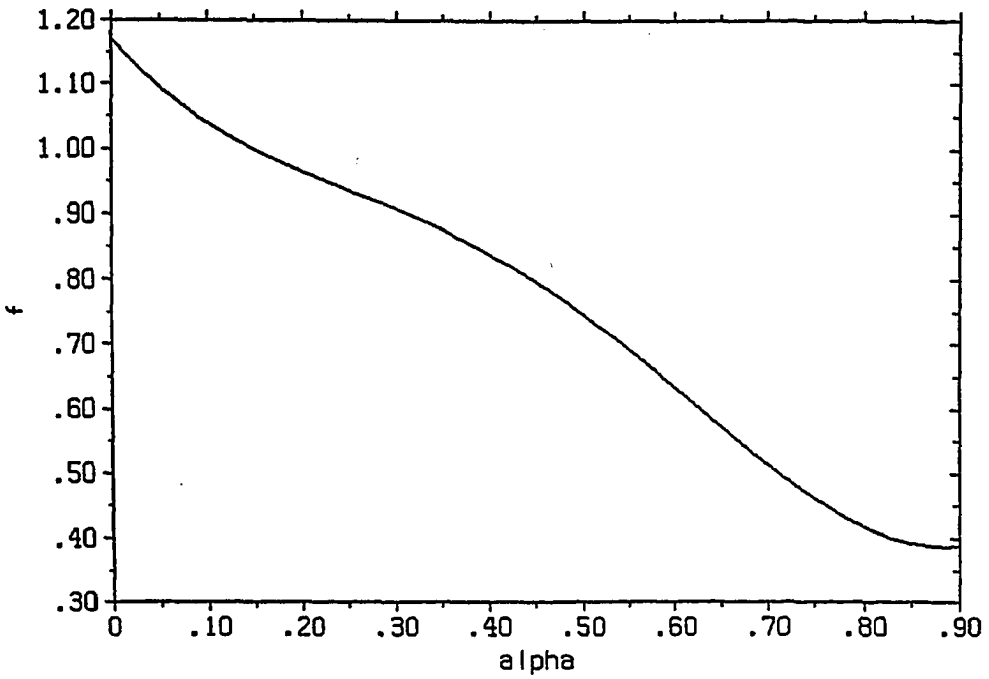

Figure 5.13. Distribution of f as a function of α for the 32 dimensional system.

product of these two quantities (as has been done by Sirovich, Ball and Keefe (1990) then (2.11) will be automatically satisfied. In the approach adopted in this work, $a_k^{(n)}(t)$ are computed by integrating a set of ODEs derived by taking a Galerkin projection of the Navier-Stokes equations. In the derivation of these ODEs the condition (2.11) has not been used explicitly but since the decomposition (2.8) is unique, it must be satisfied by the 'right' solutions representing the true behavior. Of course, since the solutions after modelling, (2.11) will not be satisfied exactly. For this analysis a matrix is defined as follows:

$$R_{kk'}^{nm} = \frac{\left\langle a_k^{(n)} a_{k'}^{(m)*} \right\rangle}{\sqrt{\lambda_k^{(n)}}\sqrt{\lambda_{k'}^{(m)}}}, \tag{5.1}$$

with m = n = 1 for the 32 dimensional case (in which case the superscripts are dropped). Here < > represents the time average. Whenever (2.11) is satisfied $R_{kk'}$ is an identity matrix.

It is quite clear that the solutions where some modes always stay at zero values cannot satisfy (2.11) because the diagonal elements of $R_{kk'}$ corresponding to these zero modes will be zero. In the 32 dimensional system for $\alpha < 0.91$ the non-zero streamwise modes stay at zero at all times (see table 4.1). This implies that the solutions for this range of α do not satisfy (2.11). As α is reduced the third window of intermittency occurs where all the modes get activated. However, the non-zero streamwise modes and the odd-zero streamwise modes are activated for a very short time and the diagonal elements corresponding to these modes are very small. After the third window of intermittency there is a range of α, where the non-zero streamwise modes are zero. For the same reason, these solutions do not represent actual velocity fields. As α is reduced further, the fourth window of intermittency occurs. In this window the non-zero streamwise modes are activated for a considerable period of time. For values of α between 0.1 and 0.2, $R_{kk'}$ is very close to a diagonal matrix (the largest non-diagonal value is of the order 10^{-2}). It is, however, not very close to an identity matrix and the diagonal elements are not always 1. Their values vary from 3.5 to 0.5. This is expected because if $R_{kk'}$ is an identity matrix then it implies that the energy of the computed system, which is directly related to the trace of $R_{kk'}$, is about 70 percent of the total energy (corresponding to the energy contained in the resolved modes only). In order to approximate the real flow field (with the totality of the energy), some diagonal elements of $R_{kk'}$ have necessarily values greater than 1.

Thus, it is concluded that for the 32 dimensional system the optimum value of α lies between 0.1 and 0.2. The solutions in this range of α lie in the fourth window of intermittency. Of course, this optimum value is deduced only after computing all the solutions and has to be computed separately for each set of truncations.

Discussing the 10D model of Aubry *et al.* (1988), Holmes (1989) points out that a reasonable quantitative reproduction of the 'energy budget' requires systems of very high dimensions, and these truncated models reveal the interaction mechanisms only qualitatively. However, the results presented below show that with the 32 dimensional model approximately correct distribution of the second order statistical quantities are recovered for the appropriate value of α. In figure 5.14, the rms of u_1 and u_2 (for $\alpha = 0.2$) are plotted as a function of x_2. The symbols in this figure are from the experimental data of Eckelmann (1974). Note that the rms values of u_2 obtained in this work are slightly lower than the experimental values, whereas the rms values of u_1 show a very good agreement. The reason for this is that of the three velocity components which constitute the turbulent kinetic energy, u_1 is the dominant one. Since the POD modes optimize the energy, a relatively larger fraction of its dominant component is captured by this set of truncations involving only 1 POD mode. The distributions of the Reynolds stress, $\langle u_1 u_2 \rangle$, and the mean velocity, U, as a function of x2 are shown in figures 5.15 and 5.16 respectively. As before, the symbols are from the data of Eckelmann (1974) and the results of the simulations in this investigation show a very good agreement with the experimental data. In figure 5.16, the broken line represents the log profile which is represented by:

$$U = \frac{1}{\kappa} \ln x_2 + B,$$

where $\kappa = 0.41$ and $B = 5.5$ (from Sreenivasan 1989).

5.4 Conclusions

In this chapter the solutions are studied in the physical space. From the results of the simulations, it is inferred that all the near-wall coherent structures, reported in the literature, are present in the low-dimensional model used in this investigation. This representation does a fairly good job in predicting the distribution of the rms values of u_1,

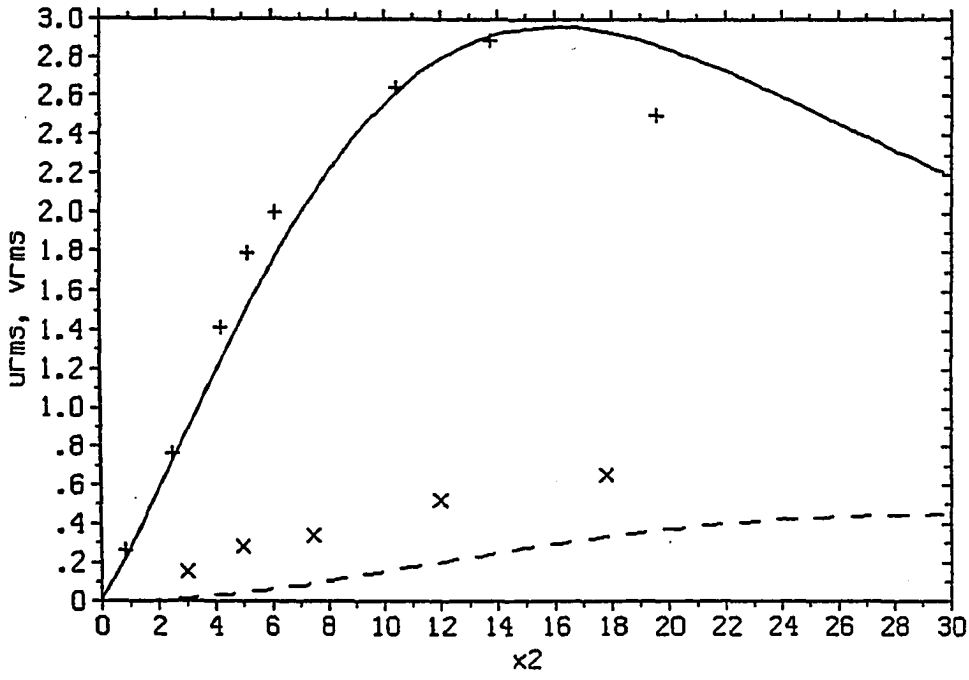

Figure 5.14. Root mean square velocity fluctuations (streamwise and normal) as a function of x_2 for the 32 dimensional system ($\alpha = 0.2$). Solid line: rms of u_1, dashed line: rms of u_2. Symbols are the experimental values from Eckelmann (1974) at Re = 8200. + : rms of u_1, × : rms of u_2.

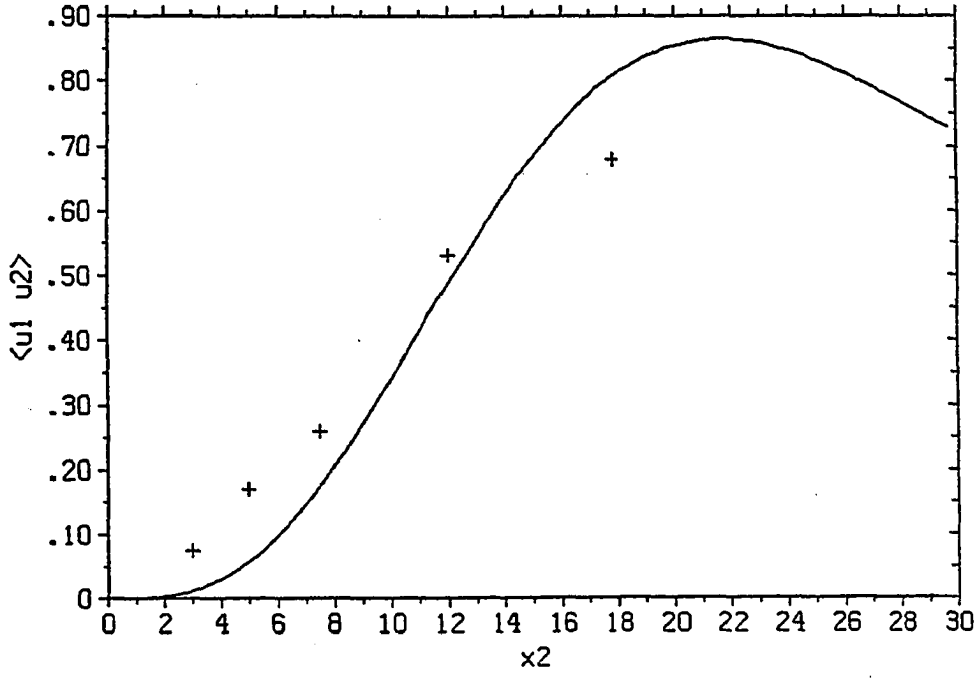

Figure 5.15. Distribution of $\langle u_1 u_2 \rangle$ as a function of x_2 for the 32 dimensional system ($\alpha = 0.2$). Symbols (+) are the experimental values from Eckelmann (1974) at Re = 8200.

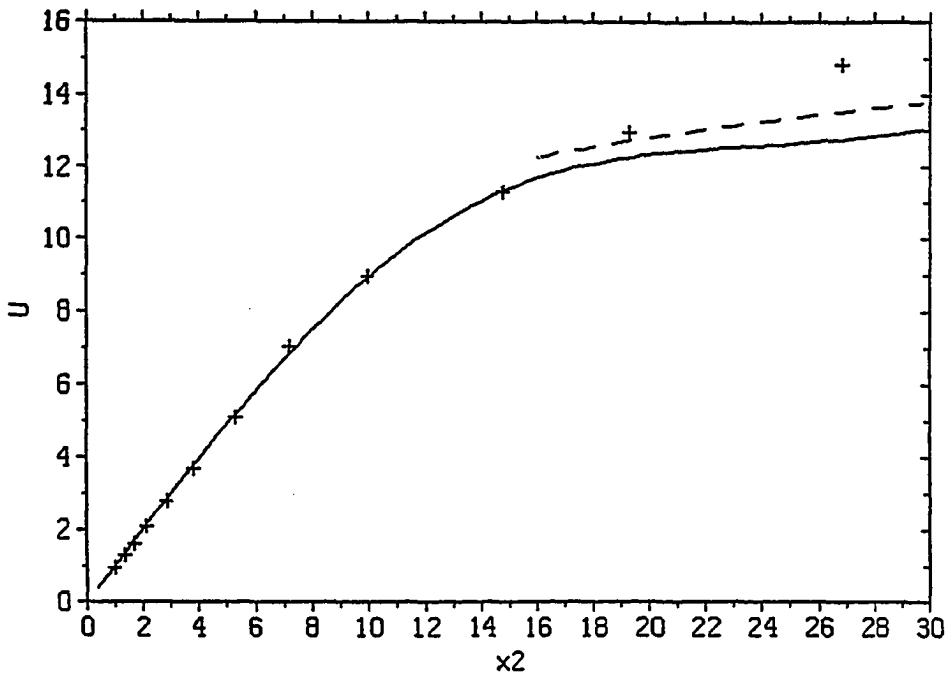

Figure 5.16. Mean velocity, U, as a function of x_2 for the 32 dimensional system (α = 0.2). Symbols are the experimental values from Eckelmann (1974) at Re = 8200. The broken line represents the log profile.

u_2, Reynolds stress and mean velocity.

Solutions for various values of α have been presented in this chapter. In some ways, this parameter seems to be playing the role of an inverse Reynolds number. Corino and Brodkey (1969) studied the wall region of the flow in a pipe at various Reynolds numbers and observed that the intensity and frequency of the ejections increase with the increasing values of the Reynolds number. They mention: "...(at high Reynolds number), the events (ejections) occurred so often and at such close intervals that even in the periods in between the events the fluid was highly agitated, and it was extremely difficult to determine when one event ended and the next began". The solutions at different values of the Heisenberg parameter indicate the same effect. For very high values of α, there is no turbulence and all fluctuations are zero. As α is reduced intermittent solutions are seen.

Within the window of intermittency of a particular type of solution, the frequency of the intermittency increases, as α decreases. In the first three windows of intermittency, the solutions are simple but as α reduces further, the solutions are irregular, displaying the features observed by Corino and Brodkey.

This investigation studies the interaction of the structures, and the regeneration of new structures because of these interactions in a turbulent flow, but the question of the origin of the coherent structures is not addressed- the structures are given as an input (in the form of the POD modes). The fact that the horseshoe vortices and the streamwise rolls are a part of the same 'structure' suggests that the formation of the streamwise rolls is a consequence of the stretching of the vorticity as in the scenario of Theodorsen (1957). It is relevant to quote the recent results of two studies at MIT, which may shed some light on the question of origin of structures. In the first study, Breuer and Haritonidis (1990), on the basis of a linear inviscid theory, show that a three-dimensional initial disturbance results in the formation of inclined shear layers, in a laminar boundary layer. In the second study, Breuer and Landahl (1990) trace the evolution of the three-dimensional disturbance via the Navier-Stokes equations for the laminar boundary layer flow. For this case, two distinct nonlinear effects are seen; the first is the production of a low speed streak, bounded by vertical and spanwise intense shear layers and the second is oscillations in the u_2 and u_3 components. In the simulations carried out in this investigation, the equations are always non-linear and the observed coherent structures represent low-speed streaks and vertical and spanwise shear layers.

Chapter 6

Expansion of Vorticity in the POD Modes

In most of the works where the POD modes have been applied the structures have been derived such that they maximize the energy, i.e. the random vector field which is expanded in terms of the POD modes is the velocity vector. In this part of the investigation the vorticity vector is expanded into the POD modes so that the 'structures' would maximize the enstrophy. From the generating equation of the POD modes it follows that the autocorrelation matrix, $<\omega_i(x)\omega_j(x')>$, is needed to solve the eigenvalue problem. It is shown below that the optimal modes which maximize the enstrophy can be directly derived from the POD modes which maximize the energy, thus avoiding the need for the autocorrelation matrix of vorticity. The method is illustrated by applying it to the near wall region of the turbulent boundary layer.

6.1 Derivation of the Vorticity Modes

In Chapter 2, the expansion of the velocity fluctuations, u_i, into the POD modes was discussed. Now the vorticity fluctuations are expanded into the POD modes. In the rest of this work the former will be termed as velocity modes and the latter as vorticity modes. The vorticity modes are derived for the turbulent boundary layer and so all the

regarding the flow (homogeneity in x_1 and x_3 directions and stationarity) made in Chapter 2 are valid. The eigenvalue problem to be solved is the following:

$$\int \Psi_{ij_k}(x_2,x_2')\psi_{j_k}^{(n)}(x_2')dx_2' = \Lambda_k^{(n)}\psi_{i_k}(x_2), \tag{6.1}$$

where $\psi_i^{(n)}$ and $\Lambda^{(n)}$ represent the eigenfunctions and their corresponding eigenvalues and Ψ_{ij} is the Fourier transform of the autocorrelation tensor for vorticity. Equation (6.1) has to be solved for each wavenumber k. The quantity optimized by these eigenfunctions is the enstrophy, $<\omega_i\,\omega_i>$.

It is now shown that given $\phi_i^{(n)}$ and $\lambda^{(n)}$, the velocity modes and their eigenvalues, one can solve for $\psi_i^{(n)}$ and $\Lambda^{(n)}$, without actually knowing the time dependent coefficients, $a^{(n)}(t)$, in (2.8). Using the definition of the vorticity and (2.8), the vorticity fluctuations, ω_i, can be written as:

$$\omega_i = \frac{1}{\sqrt{L_1L_3}}\sum_{lkn} a_k^{(n)}(t)\xi_{i_k}^{(n)}(x_2)\,e^{2\pi i(lx_1+kx_3)}, \tag{6.2}$$

where

$$\xi_{1_k}^{(n)} = \frac{d\phi_{3_k}^{(n)}}{dx_2} - 2\pi ik\phi_{2_k}^{(n)},$$

$$\xi_{2_k}^{(n)} = 2\pi i\left(k\phi_{1_k}^{(n)} - l\phi_{3_k}^{(n)}\right),$$

and

$$\xi_{3_k}^{(n)} = 2\pi il\phi_{2_k}^{(n)} - \frac{d\phi_{1_k}^{(n)}}{dx_2}.$$

The contribution to the vorticity field by each structure (n) of the velocity modes is given by the following expression:

$$\omega_i^{(n)} = \frac{1}{\sqrt{L_1 L_3}} \sum_{lk} a_k^{(n)}(t) \xi_{i_k}^{(n)}(x_2)\, e^{2\pi i(lx_1 + kx_3)}. \tag{6.3}$$

$\hat{\omega}_{i_k}$, the Fourier transform of ω_i, can be expressed as:

$$\hat{\omega}_{i_k}(x_2) = \sqrt{L_1 L_3} \sum_n a_k^{(n)} \xi_{i_k}^{(n)}. \tag{6.4}$$

Ψ_{ij_k}, the Fourier transform of $<\omega_i(x_2)\omega_j(x_2')>$, is determined from the relation:

$$\Psi_{ij_k}(x_2, x_2') = \frac{1}{L_1 L_3} \langle \hat{\omega}_{i_k}(x_2) \hat{\omega}_{j_k}^*(x_2') \rangle = \sum_{mn} \langle a_k^{(n)} a_k^{(m)*} \rangle \left\{ \xi_{i_k}^{(n)}(x_2) \xi_{j_k}^{(m)*}(x_2') \right\}. \tag{6.5}$$

In view of (2.11) and (6.5) the eigenvalue problem, (6.1), can be rewritten as

$$\int \sum_m \lambda_k^m \xi_{i_k}^{(m)}(x_2) \xi_{j_k}^{(m)*}(x_2')\, \psi_{j_k}^{(n)}(x_2')\, dx_2' = \Lambda_k^{(n)} \psi_{i_k}^{(n)}(x_2), \tag{6.6}$$

which needs to be solved for each wavenumber k.

The vorticity fluctuations can be expressed in terms of the computed eigenvalues and eigenvectors (ψ and Λ) as

$$\omega_i(x_1, x_2, x_3, t) = \frac{1}{\sqrt{L_1 L_3}} \sum_{n,k} b_k^{(n)}(t) \psi_{i_k}^{(n)}(x_2)\, e^{2\pi i\left(\frac{l}{L_1} x_1 + \frac{k}{L_3} x_3\right)}, \tag{6.7}$$

where $b^{(n)}(t)$ are time dependent coefficients which have to be determined.

ψ and b satisfy orthogonality relations analogous to (2.10) and (2.11), respectively, i.e.

$$\int \psi_{i_k}^{(n)} \psi_{i_{k'}}^{(m)*} dx_2 = \delta_{nm}\delta_{kk'}, \tag{6.8}$$

and

$$\langle b_k^{(n)} b_{k'}^{(m)*} \rangle = \Lambda_k^{(n)} \delta_{nm}\delta_{kk'}. \tag{6.9}$$

The contribution to the vorticity by each structure (n) of the vorticity modes is

$$\omega_i^{(n)} = \frac{1}{\sqrt{L_1 L_3}} \sum_k b_k^{(n)}(t) \psi_{i_k}^{(n)}(x_2)\, e^{2\pi i(\frac{l}{L_1}x_1 + \frac{k}{L_3}x_3)}. \tag{6.10}$$

The relation between $a^{(n)}(t)$ and $b^{(n)}(t)$, the time dependent coefficients in (2.8) and (6.7) can be derived as follows. From (6.4) and (6.7),

$$\hat{\omega}_{i_k} = \sqrt{L_1 L_3} \sum_n a_k^{(n)} \xi_{i_k}^{(n)} = \sqrt{L_1 L_3} \sum_m b_k^{(m)} \psi_{i_k}^{(m)}. \tag{6.11}$$

Taking an inner product of (6.11) with $\psi_{i_k}^{(p)}$ and using (6.8) leads to the following expression:

$$b_k^{(p)} = \sum_n c_k^{(p)(n)} a_k^{(n)}, \tag{6.12}$$

where

$$c_k^{(p)(n)} = (\xi_{i_k}^{(n)}, \psi_{i_k}^{(p)}).$$

6.2 Results and Discussion

The velocity modes (derived by Herzog 1986) are used to obtain the vorticity modes. The data is available only for the first 3 velocity modes and so the index of summation m in (6.6) varies from 1 to 3. All the quantities, as before, are non-dimensionalized by the wall variables (u_τ and ν). The eigenvalue distribution is studied as a function of the streamwise (l) and spanwise (k) wavenumbers. Figure 6.1 shows $\Lambda^{(n)}_{l,k}$ for $l = 0$ as a function of k for the first 3 modes. For the dominant mode (n = 1) the peak is observed at $k = 0.006$, while it occurred at $k = 0.003$ for the velocity modes. It, thus, follows that the enstrophy spectrum is shifted to the right (in the spanwise direction) as compared to the energy spectrum. The variation of eigenvalues with the streamwise wavenumber, l, also exhibits a similar behavior. In figure 6.2, the distribution of $\Lambda^{(n)}_{l,k}$ is plotted as a function of l for $k = 0$. For the velocity modes (figure 2.2), it is observed that the maximum occurs at $l = 0$ and that there is a monotonic decay as l increases. The vorticity modes also have a maximum at $l = 0$ but there is a local maximum at $l = 0.0015$. Similar results have been recently reported by Balint *et al.* (1991), who compared the energy and enstrophy spectra at a location close to the wall ($x_2 = 18$) in a turbulent boundary layer and found that the peak of the enstrophy spectrum shifts to the right as compared to the energy spectrum. Moreover, the knowledge of the distribution of the eigenvalues in wavenumber space is useful in selecting the modes to be retained in a numerical simulation. For example, if a simulation has to be carried out with 2 l modes (say the 32 dimensional case) then the information which can be deduced from the eigenvalue spectrum of the velocity modes is that $l = 0$ should be retained. The eigenvalue spectrum of vorticity modes reveals that the modes with $l = 0.0015$ are also important and should be retained.

The convergence of the enstrophy in the successive eigenfunctions is quite rapid. Since the index of summation m in (6.6) varies up to 3, only the first three modes make a significant contribution towards the enstrophy. While the first eigenmode captures 75 percent of the total enstrophy, the first two capture 94 percent.

Eigenfunctions for the vorticity modes, $\psi_i^{(n)}$, and the corresponding functions for the velocity modes, $\xi_i^{(n)}$(6.2), are displayed for a set of wavenumbers in figures 6.3 and 6.4. These functions have very similar shapes and this similarity is observed for all the set of wavenumbers for which $\psi_i^{(n)}$ is calculated. Note, however, that this does not imply that the vorticity structures (for each n) from (6.3) and (6.10) will be identical because the distribution of the eigenvalues with the wavenumbers are different for these two sets.

Next, the vortical structures are investigated at one instant of time. In order to calculate the coefficients, $b_k^{(n)}(t)$, (6.12) is used and the data for the coefficients, $a_k^{(n)}(t)$, is taken from the simulations of the 64 dimensional system (Chapter 4.3). It is recalled that this system includes 2 normal modes, 3 streamwise modes (N_1 =1) and 11 spanwise modes (N_3 = 5). First, the vorticity field is calculated from (6.2). In figure 6.5 (a,b and c) contours of ω_1,ω_2 and ω_3 are shown in a cross-stream (x_2-x_3) plane. Of the three components, the spanwise component is the dominant one. The contributions from the first two structures for the velocity modes are calculated from (6.3). Contours of the three vorticity components for these first and second structures in the same cross-stream plane are shown in figures 6.6 and 6.7 respectively. The first structure (figure 6.6) has patterns very similar to those observed in the total field (figure 6.5). However, the limiting values of the contours (table 6.1) show that the ratio of the maximum value of ω_3 in figure 6.6 and that in figure 6.5 is 0.625. The structures derived from the vorticity modes are calculated from (6.10). Contours of the three components for the first two structures in the cross-stream plane are plotted in figures 6.8 and 6.9 respectively. As in the previous case the first structure looks akin to the total field but in this case it captures a greater portion of the

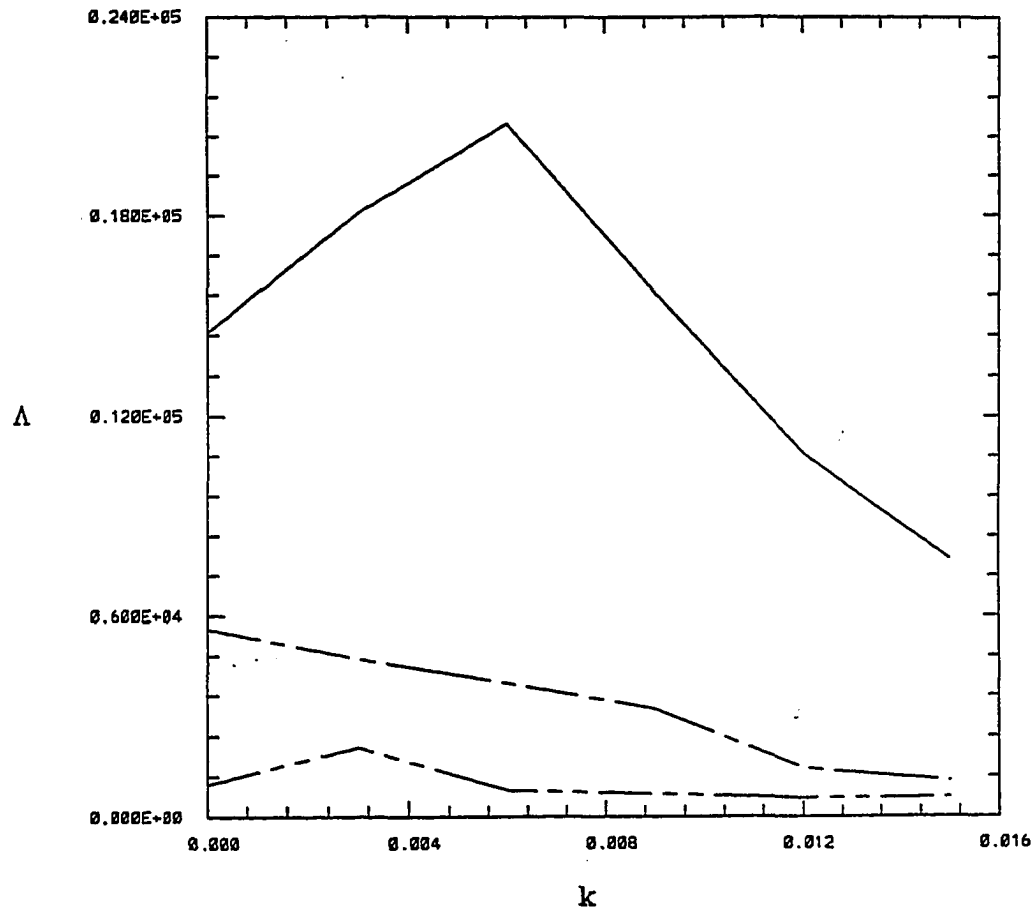

Figure 6.1. Distribution of the eigenvalues for the vorticity modes, $\Lambda_{0,k}^{(n)}$, as a function of the spanwise wavenumber, k, at the zero streamwise wavenumber (n = 1 ----------, n = 2 - ---- -- ----and n = 3 ---- -- -- ----).

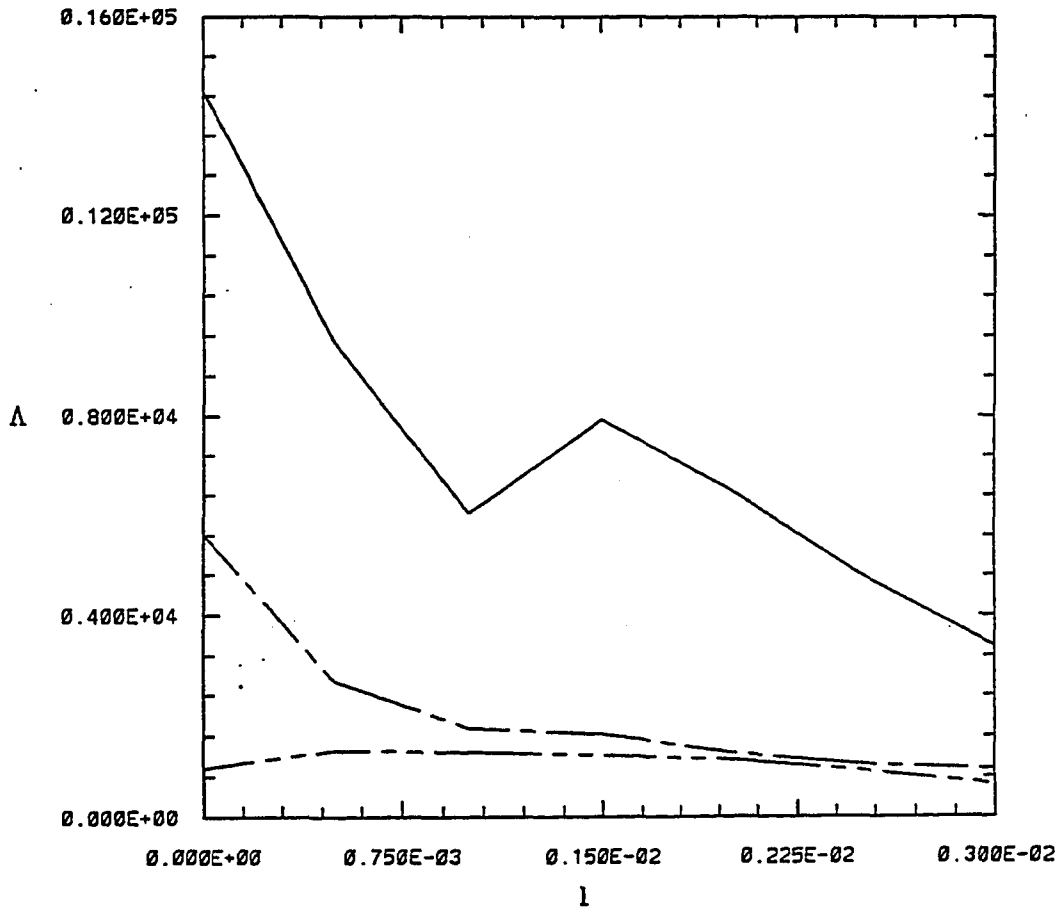

Figure 6.2. Distribution of the eigenvalues for the vorticity modes, $\Lambda_{l,0}^{(n)}$, as a function of the streamwise wavenumber, l, at the zero spanwise wavenumber (n = 1 ----------, n = 2 -- --- -- ----and n = 3 ---- -- -- ----).

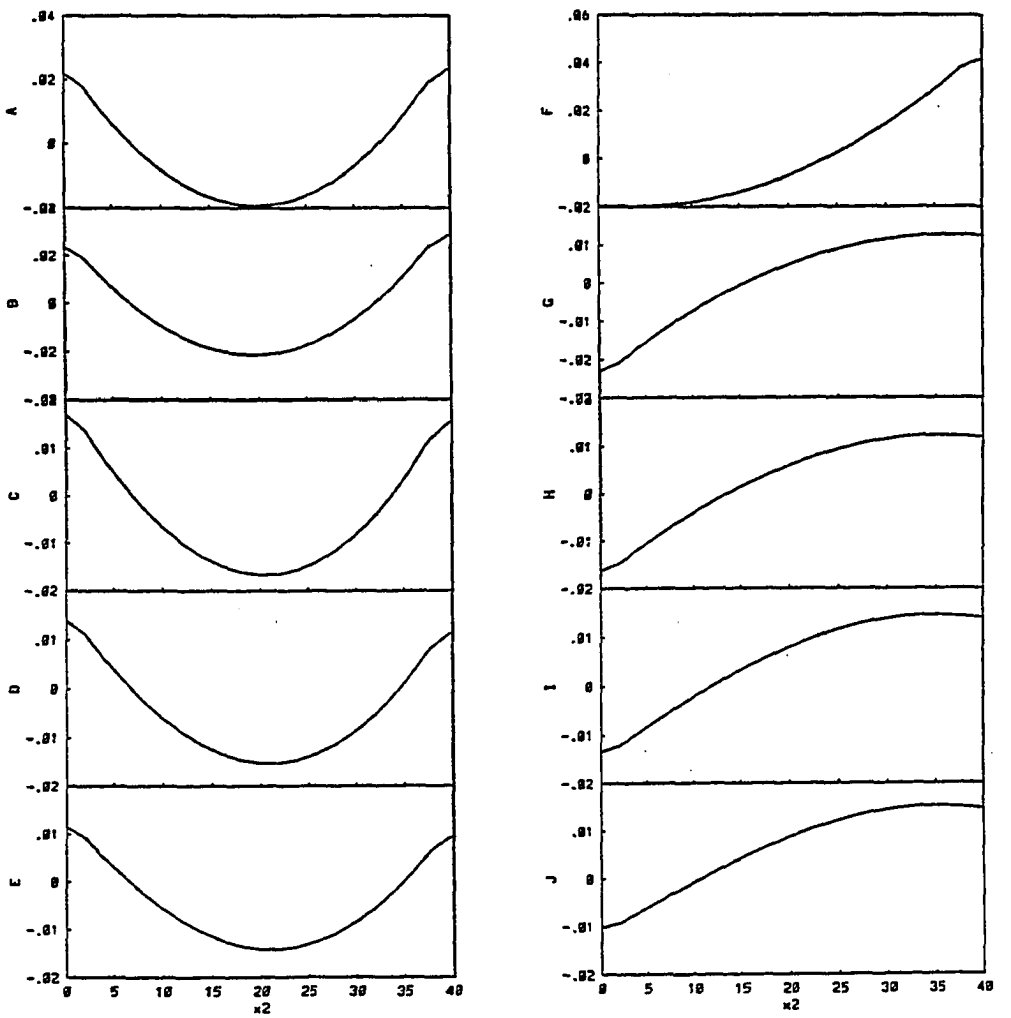

Figure 6.3(a). The real (A-E) and imaginary (F-J) parts of the x_1 component of the eigenfunctions for the first vorticity mode, $\psi_{1k}^{(1)}$, as a function of x_2, for the streamwise wavenumber = 1.5×10^{-3} and different spanwise wavenumbers - (A) and (F): 3.0×10^{-3}, (B) and (G): 6.0×10^{-3}, (C) and (H): 9.0×10^{-3}, (D) and (I): 1.2×10^{-2}, (E) and (J): 1.5×10^{-2}.

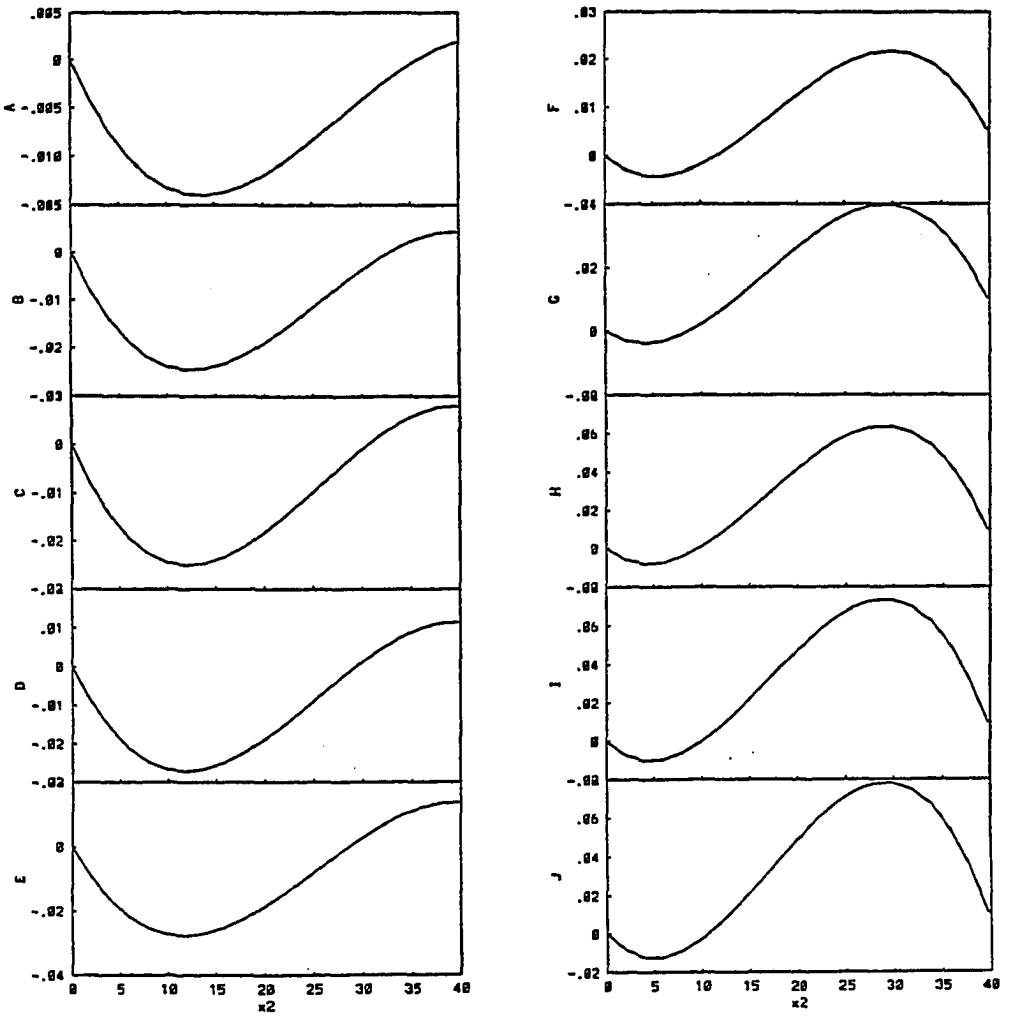

Figure 6.3(b). The real (A-E) and imaginary (F-J) parts of the x_2 component of the eigenfunctions for the first vorticity mode, $\psi_{2_k}^{(1)}$, as a function of x_2, for the streamwise wavenumber = 1.5×10^{-3} and different spanwise wavenumbers - (A) and (F): 3.0×10^{-3}, (B) and (G): 6.0×10^{-3}, (C) and (H): 9.0×10^{-3}, (D) and (I): 1.2×10^{-2}, (E) and (J): 1.5×10^{-2}.

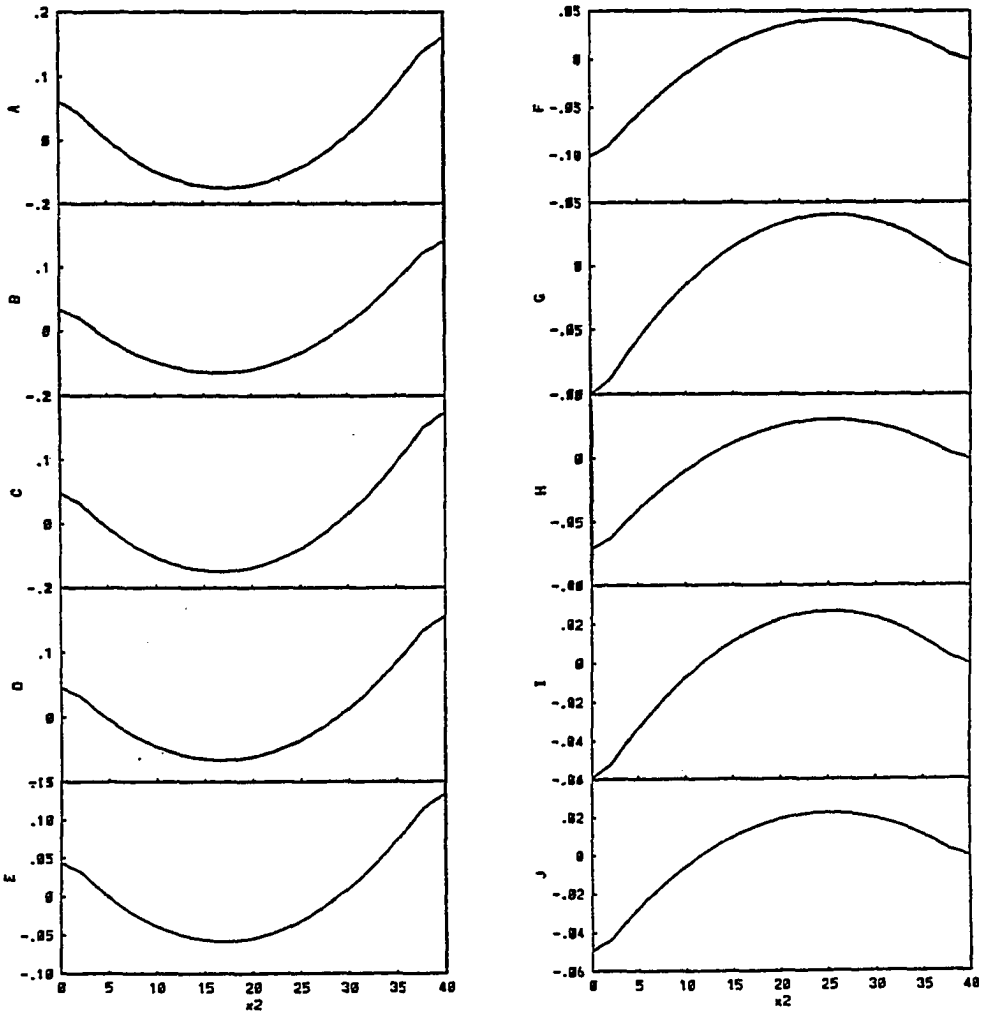

Figure 6.3(c). The real (A-E) and imaginary (F-J) parts of the x_3 component of the eigenfunctions for the first vorticity mode, $\psi^{(1)}_{3_k}$, as a function of x_2, for the streamwise wavenumber = 1.5×10^{-3} and different spanwise wavenumbers - (A) and (F): 3.0×10^{-3}, (B) and (G): 6.0×10^{-3}, (C) and (H): 9.0×10^{-3}, (D) and (I): 1.2×10^{-2}, (E) and (J): 1.5×10^{-2}.

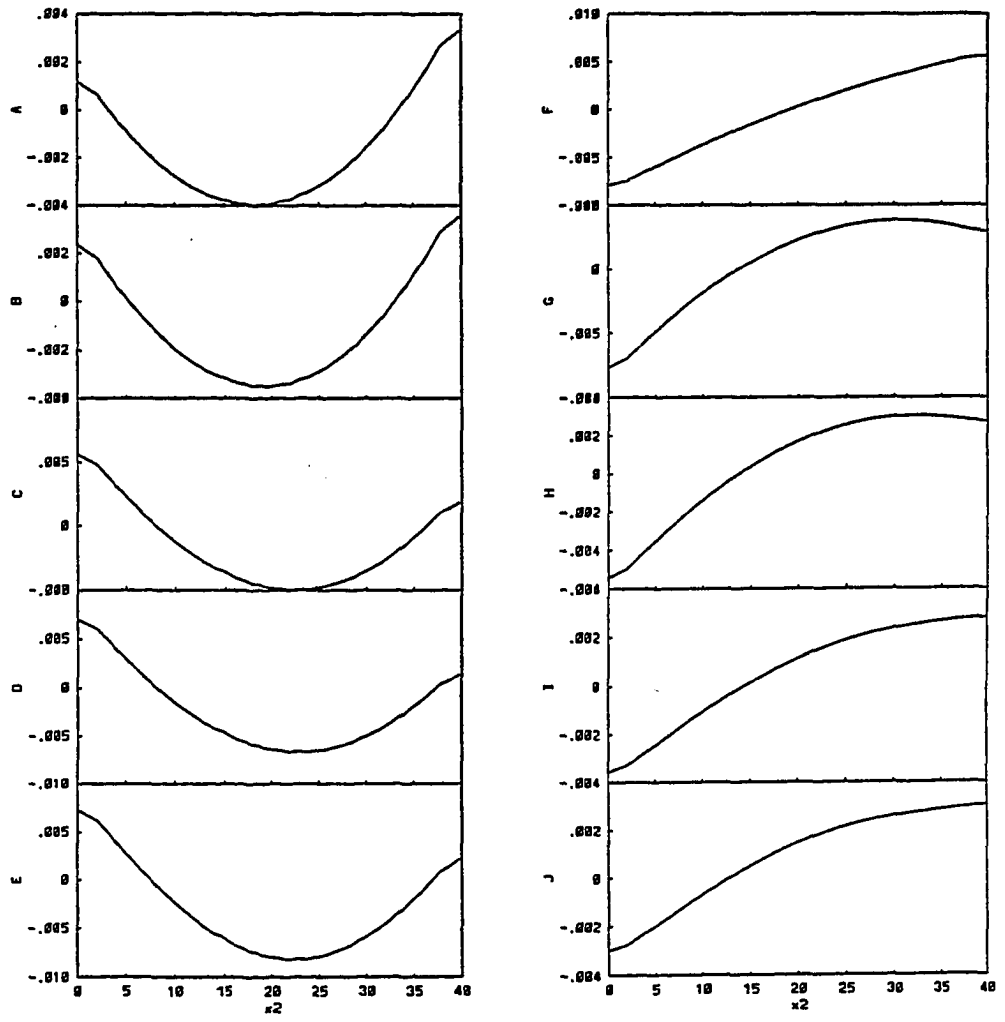

Figure 6.4(a). The real (A-E) and imaginary (F-J) parts of $\xi^{(1)}_{1_k}$ as a function of x_2, for the streamwise wavenumber = 1.5×10^{-3} and different spanwise wavenumbers - (A) and (F): 3.0×10^{-3}, (B) and (G): 6.0×10^{-3}, (C) and (H): 9.0×10^{-3}, (D) and (I): 1.2×10^{-2}, (E) and (J): 1.5×10^{-2}.

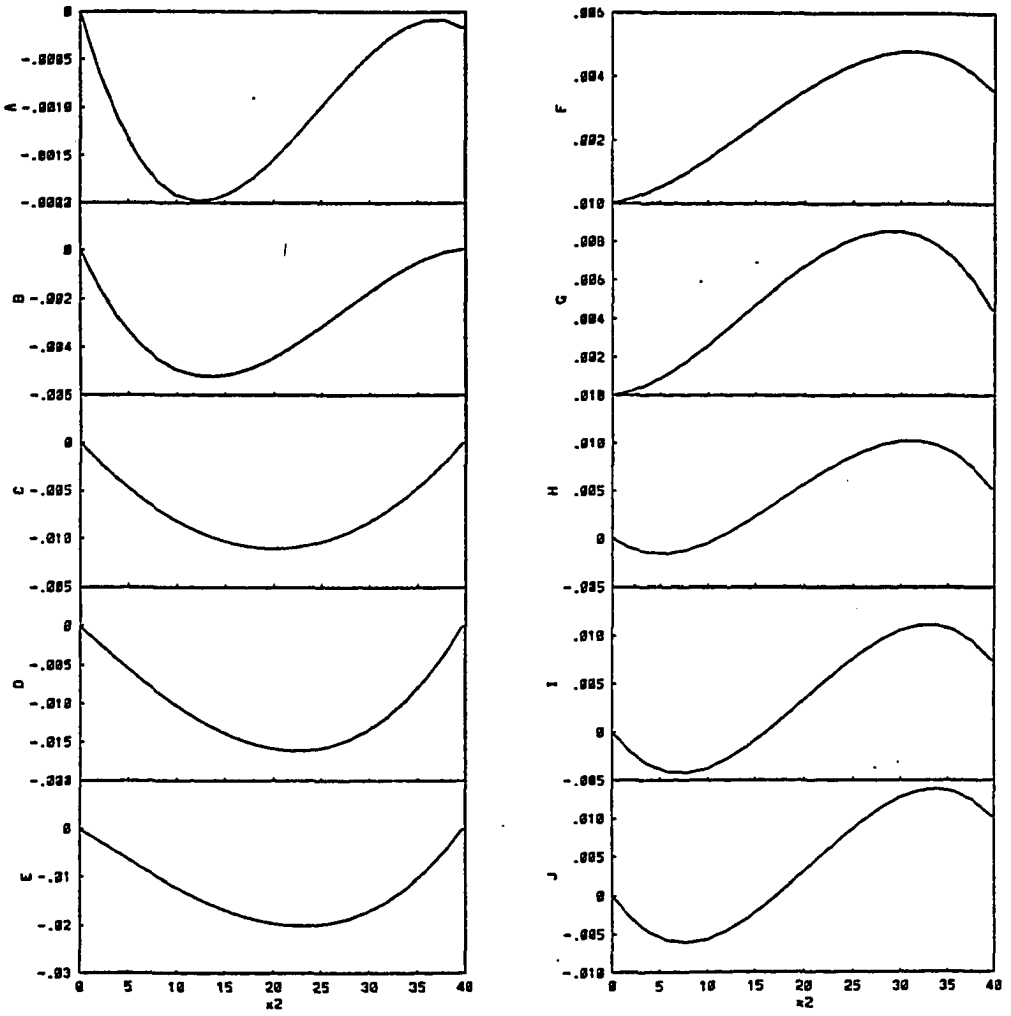

Figure 6.4(b). The real (A-E) and imaginary (F-J) parts of $\xi_{2k}^{(1)}$ as a function of x_2, for the streamwise wavenumber = 1.5×10^{-3} and different spanwise wavenumbers - (A) and (F): 3.0×10^{-3}, (B) and (G): 6.0×10^{-3}, (C) and (H): 9.0×10^{-3}, (D) and (I): 1.2×10^{-2}, (E) and (J): 1.5×10^{-2}.

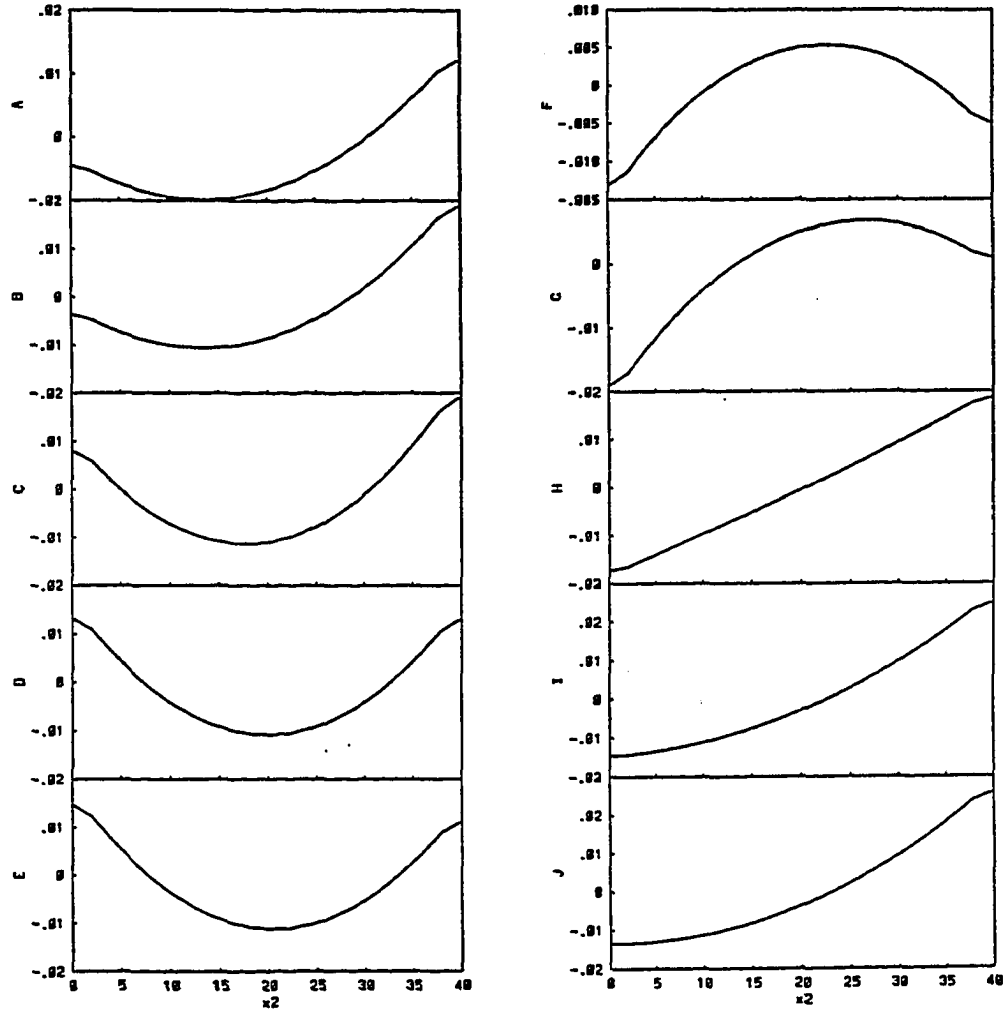

Figure 6.4(c). The real (A-E) and imaginary (F-J) parts of $\xi_{3_k}^{(1)}$ as a function of x_2, for the streamwise wavenumber = 1.5×10^{-3} and different spanwise wavenumbers - (A) and (F): 3.0×10^{-3}, (B) and (G): 6.0×10^{-3}, (C) and (H): 9.0×10^{-3}, (D) and (I): 1.2×10^{-2}, (E) and (J): 1.5×10^{-2}.

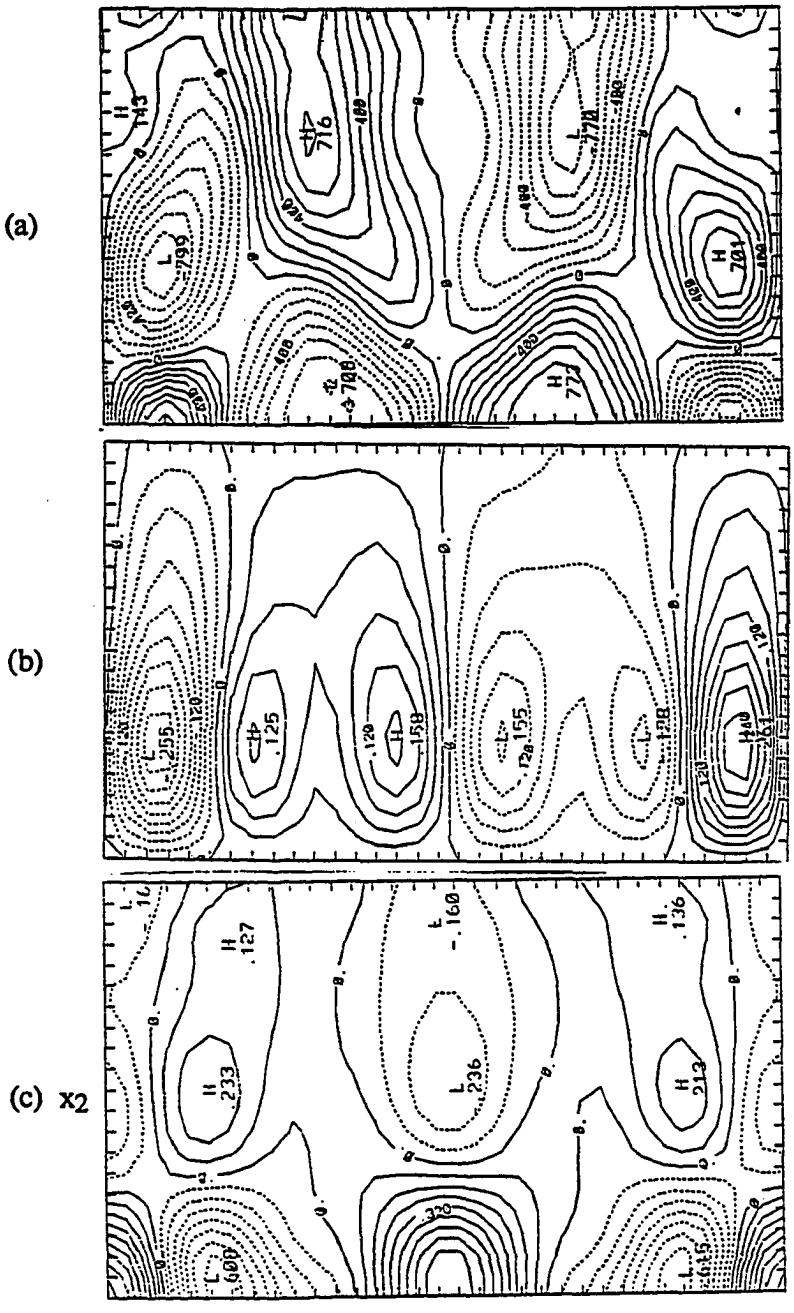

Figure 6.5. Contours of the three components of vorticity, ω_i, (i=1, 2 and 3 in (a), (b) and (c) respectively) in an x_2-x_3 plane from the calculations of Chapter 4.3. The normal dimension of the box from the wall (bottom) to the top is 40 and the spanwise dimension is 333. The dotted lines represent contours whose magnitude is less than zero. The maximum and minimum values are shown in table 6.1.

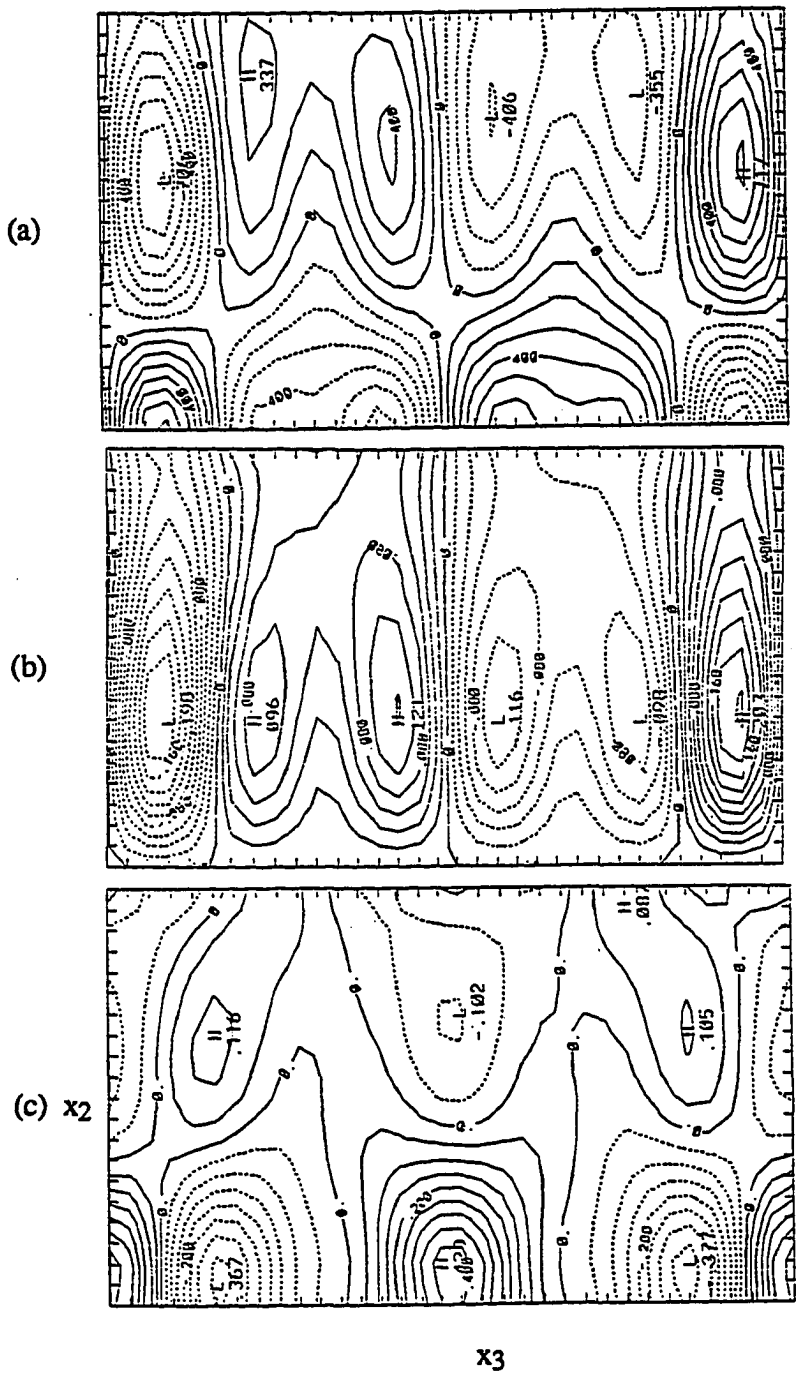

Figure 6.6. Contours of the three components of vorticity calculated from the first velocity mode (other details as in figure 6.5).

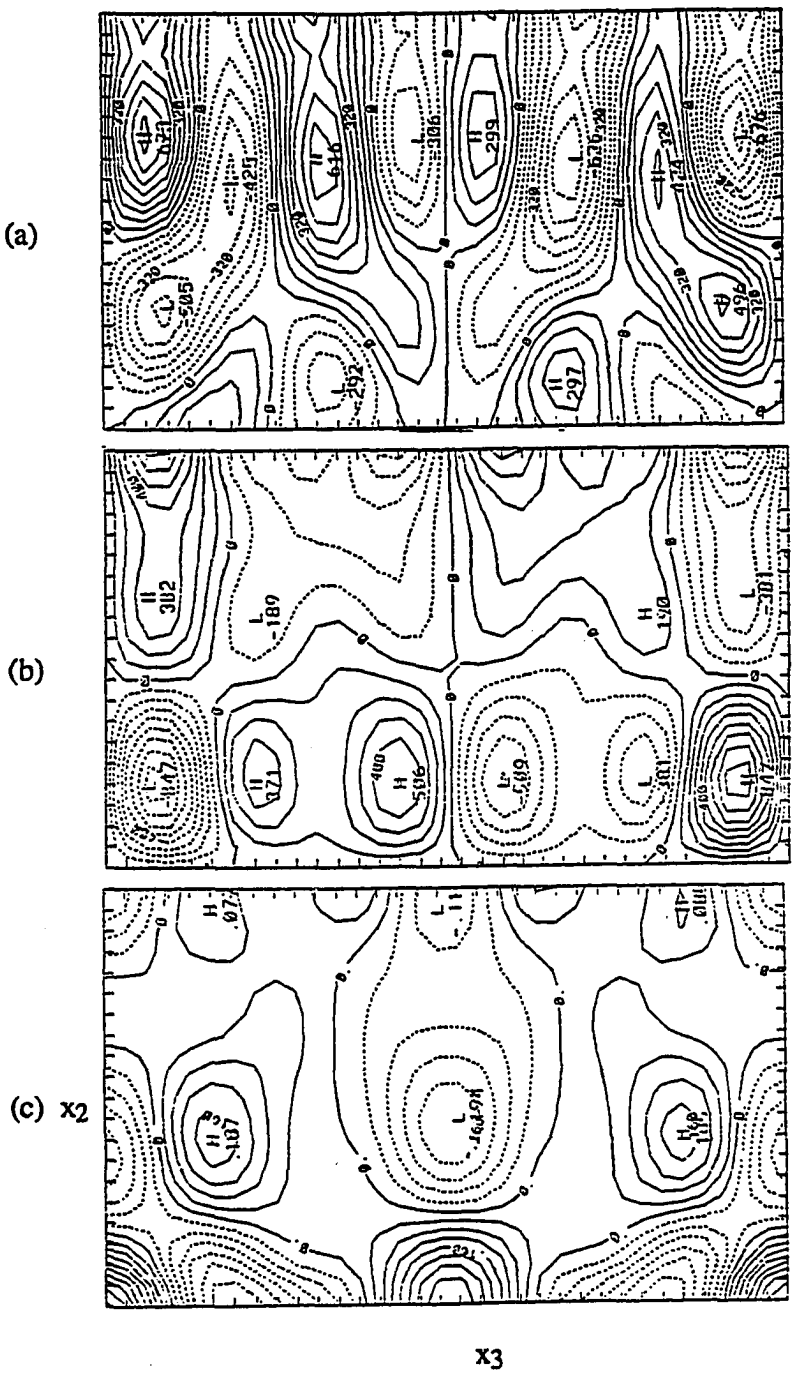

Figure 6.7. Contours of the three components of vorticity calculated from the second velocity mode (other details as in figure 6.5).

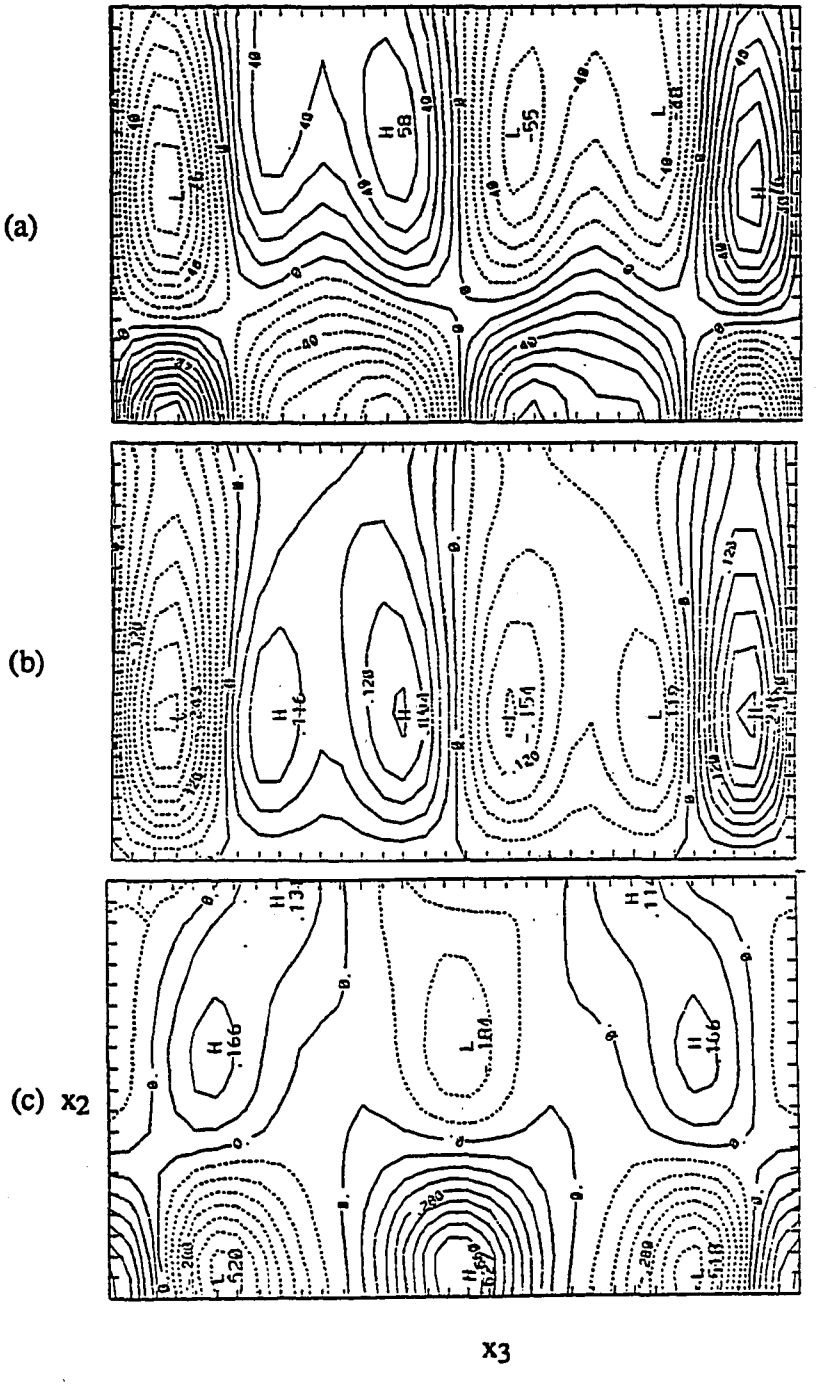

Figure 6.8. Contours of the three components of vorticity calculated from the first vorticity mode (other details as in figure 6.5).

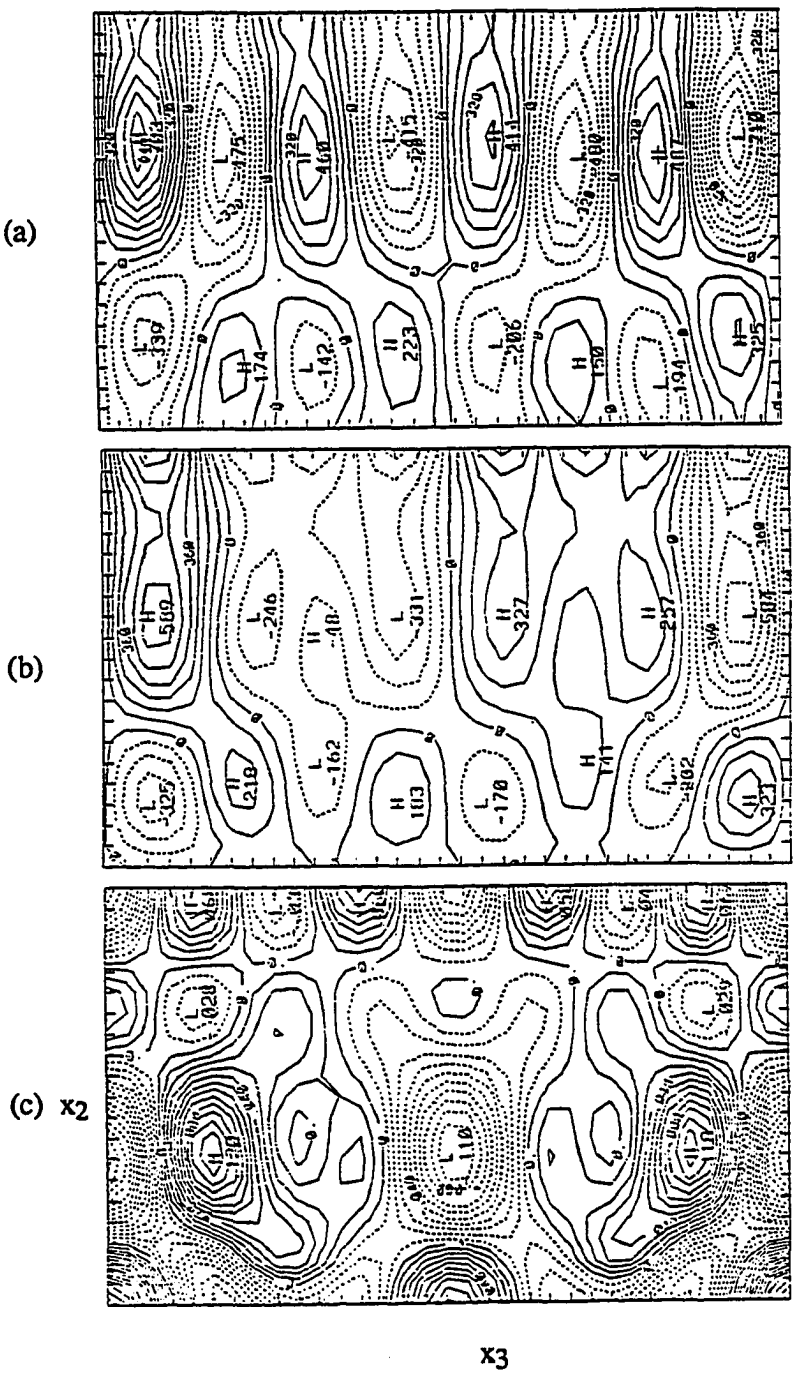

Figure 6.9. Contours of the three components of vorticity calculated from the second vorticity mode (other details as in figure 6.5).

Figure	Quantity	Maximum	Minimum
6.5(a)	ω_1 (from the total field)	0.08	-0.08
6.5(b)	ω_2 (from the total field)	0.24	-0.24
6.5(c)	ω_3 (from the total field)	0.64	-0.56
6.6(a)	ω_1 (from the first velocity mode)	0.07	-0.07
6.6(b)	ω_2 (from the first velocity mode)	0.20	-0.18
6.6(c)	ω_3 (from the first velocity mode)	0.40	-0.35
6.7(a)	ω_1 (from the second velocity mode)	0.06	-0.06
6.7(b)	ω_2 (from the second velocity mode)	0.08	-0.08
6.7(c)	ω_3 (from the second velocity mode)	0.36	-0.24
6.8(a)	ω_1 (from the first vorticity mode)	0.09	-0.09
6.8(b)	ω_2 (from the first vorticity mode)	0.24	-0.24
6.8(c)	ω_3 (from the first vorticity mode)	0.56	-0.49
6.9(a)	ω_1 (from the second vorticity mode)	0.06	-0.06
6.9(b)	ω_2 (from the second vorticity mode)	0.07	-0.07
6.9(c)	ω_3 (from the second vorticity mode)	0.15	-0.14

Table 6.1. Maximum and minimum values of the vorticity contours.

total vorticity compared to the first structure of the velocity modes (the ratio of maximum value of ω_3 in figure 6.8 to that in figure 6.5 being 0.875). Vectorial plots of ω_2-ω_3 in a cross-stream plane also exhibit the same trend. In figure 6.10(a) the plot is shown for the total field whereas the plots obtained from the first velocity and vorticity structures are shown in figures 6.10 (b) and 6.10 (c). The ratio of the magnitude of the maximum vector in figure 6.10(b) and figure 6.10 (a) is 0.6 while the ratio corresponding to figure 6.10 (c) and figure 6.10 (a) is 0.87. Thus, it can be inferred that the first structures from the vorticity and the velocity modes are qualitatively very similar to the total field but the former captures a greater percentage of the field than the latter.

The technique of deriving the vorticity modes from the velocity modes has been demonstrated for the near-wall boundary layer flow. A note of caution should, however, be added. Since the peak in the enstrophy spectrum occurs at a higher wavenumber than in the energy spectrum, the wavenumbers for which the vorticity modes are calculated should go well past the peak of the enstrophy spectrum.

6.3 Conclusions

In this chapter the POD has been applied to the vorticity field, extending the latter into structures. It has been shown that given the data for the velocity eigenfunctions and their eigenvalues, the vorticity modes and their eigenvalues can be calculated. Since researchers in the community have been working on the velocity modes for different types of turbulent flows these databases can be utilized to generate the vorticity modes for these flows.

The vorticity modes are obtained for the near-wall region of the turbulent boundary layer. The spectrum of their eigenvalues is studied and compared with that of the velocity modes. As expected it is found that the peak in the spectrum of eigenvalues for the vorticity modes is at a higher wavenumber compared to the spectrum for the velocity

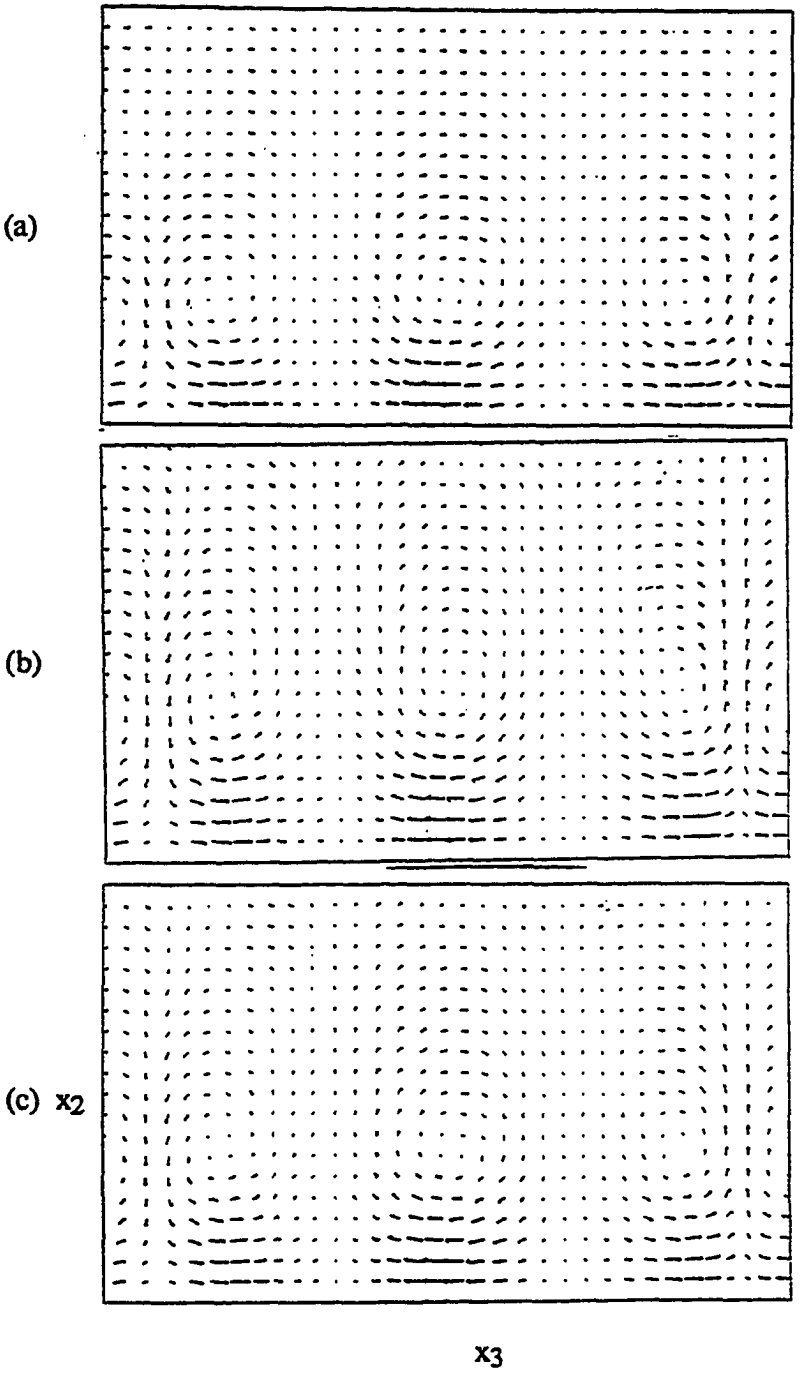

Figure 6.10. Vector representation of ω_2 - ω_3 in an x_2-x_3 plane from (a) the total field, (b) the first velocity mode, and (c) the first vorticity mode. The dimensions and orientation of the box are the same as in figure 11. The magnitudes of the maximum vectors in (a), (b) and (c) are 0.719, 0.627 and 0.429 respectively.

modes. This shift is, however, small and this is attributed to the low Reynolds number of the flow in the near-wall region (J. L. Lumley, private communication 1991). The distribution of the eigenvalues in the wavenumber space can also be used as a guiding criterion in deciding which modes are to be retained while carrying out a numerical simulation.

From the results of integrations in section 4.3, the vorticity field is calculated and the physical structures reconstructed from the velocity and vorticity modes are compared. While the first structures are qualitatively similar, the one from vorticity modes is more 'efficient' in the sense that it has a larger value of enstrophy than its velocity counterpart.

Chapter 7

A Dynamic Eddy Viscosity Model

An alternate model to account for the losses to the unresolved modes, based on the approximate inertial manifold approach, is proposed in this chapter. Through the application of the inertial manifold theory, the long time behavior of a dissipative partial differential equation (PDE) can be reduced to a finite dimensional dynamical system. An inertial manifold is a finite dimensional, invariant, smooth manifold which contains the global attractor of the PDE (the PDE reduces to a finite set of ODEs on this manifold). The systems where the existence of inertial manifolds has been established include the Ginzburg-Landau equation (Constantin 1987, Doering *et al.* 1988 and others), reaction-diffusion equations (Constantin *et al.* 1988, Mallet-Paret and Sell 1988 and Jolly 1989), damped Hamiltonian systems (Nicolaenko 1987) and the Kuramoto-Sivashinsky equation (Constantin *et al.* 1988, 1989 and Foias *et al.* 1988b). So far, the existence of the inertial manifolds has not been proved for the 3-D Navier-Stokes equations. Even if the existence of the inertial manifold for a particular PDE is proved, there are no methods for obtaining it in a closed form and it is, therefore, necessary to approximate it. Methods developed with this purpose are referred to as the approximate inertial manifold (AIM) techniques or the nonlinear Galerkin methods. See for example, Foias *et al.* (1988a), Foias and Temam (1988), Temam (1988), Titi (1988) and Jolly *et al.* (1990). In a recent work, Foias *et al.* (1991) have demonstrated that the application of this method to the Navier-Stokes

equations leads to their modification such that an effective viscosity-like term arises in a natural way.

AIMs have been developed for the Navier-Stokes equations. The velocity is expanded in terms of Stokes eigenfunctions (i.e. Fourier modes). A Galerkin projection onto these modes (similar to the procedure adopted in Chapter 2) leads to a set of ODEs. Truncating this set, the higher order modes are approximated by means of algebraic equations and the approximated values are used in the equations for the lower order (retained) terms. In this work, the AIM technique is applied to Galerkin projections onto the POD modes (instead of Fourier modes). Since these modes are more optimal than any other set, a combination of the POD technique and the AIM ideas should be particularly efficient. However, up to our knowledge, no theory has been established on this idea.

Let $a_<$ and $a_>$ represent the fully resolved and the approximated modes, respectively. The ODEs for these terms can be written as follows:

$$\frac{da_<}{dt} = L(a_<) + L(a_>) + Q(a_< + a_>, a_< + a_>) + C(a_< + a_>, a_< + a_>, a_< + a_>). \quad (7.1)$$

$$\frac{da_>}{dt} = L(a_<) + L(a_>) + Q(a_< + a_>, a_< + a_>) + C(a_< + a_>, a_< + a_>, a_< + a_>), \quad (7.2)$$

where L, Q and C represent the linear, quadratic and cubic terms. The time derivative term in (7.2) is assumed to be negligible compared to the other terms and an iterative scheme, adapted on the basis of the steady inertial manifold technique (Titi 1988), is developed to approximate the value of $a_>$ from (7.2). Let $a_>^N$ represent the value after N+1 iterations. While the first iteration consists of

$$L(a_>^0) = L(a_<) + Q(a_<, a_<) + C(a_<, a_<, a_<), \quad (7.3)$$

each subsequent iteration is carried out by

$$L(a_>^{I+1}) = L(a_<) + + Q(a_< + a_>^I, a_< + a_>^I) + C(a_< + a_>^I, a_< + a_>^I, a_< + a_>^I). \qquad (7.4)$$

If $a_>$ converges after N iterations then the value of $a_>^N$ is used to represent $a_>$ in (7.1).

The method can be viewed as an effective dynamic eddy-viscosity model, where the effect of the neglected modes is accounted for at each time step. Note that this is different from the eddy viscosity model described earlier (Chapter 2) where the neglected modes are represented by time-independent coefficients of the linear and quadratic terms.

Preliminary studies are performed for two sets of truncations. Here, $a_<$ and $a_>$ represent $a_{l,k}^{(1)}$ and $a_{l,k}^{(2)}$ respectively, with k = 1, 2, 3, 4 and 5. In the first set l = 0 (10D model) and in the second l = -1, 0 ,1 (32 dimensional model). In both cases, convergence of the iterative scheme described above was not achieved in the approximation of $a_>$, indicating that the method fails for the set of ODEs considered here. From the results of the integrations of the 20 and 64 dimensional systems the exact values of $a_>$ are studied, and it is found that the time derivative term in (7.2), which had been neglected in these approximations, is of the same order as the time derivative term in (7.1). So neglecting this term does not seem to be justified and is the possible reason for the failure of this approach. It is also possible that the number of resolved terms is not high enough and should be increased. It is interesting to note that in the context of the usual AIM technique (using the Fourier modes as resolved modes), Jones and Titi (1991) have recently shown that under a time-dependent forcing f(t), the term $\frac{da_>}{dt}$ may be very large. The reason why this term is important in this case may be related to the latter finding, since the turbulence production arises as time-dependent cubic terms. Perhaps, a remedy to this problem would be to consider the POD modes for the time derivative of the velocity, rather than the velocity

itself, an idea proposed by Sirovich (1989). In this case, the norm of the term $\frac{da_>}{dt}$ in (7.2) would be systematically minimized.

Chapter 8

Conclusions

The findings of this investigation are summarized in this chapter. The initial study of Aubry *et al.* (1988) revealed a basic intermittency due to a saddle-saddle connection in the dynamical system generated by taking a Galerkin projection of the POD modes of the near-wall turbulent flow onto the Navier-Stokes equations. The biggest limitation of their representation was the lack of explicit streamwise variations in the flow for the chosen set of truncations. One of the goals of this investigation was to study the effect of the addition of the non-zero streamwise modes on the intermittent mechanisms reported in Aubry *et al.* (1988). Another issue of key importance, which is related to the objective stated above, was the robustness of the intermittent phenomenon to the order of the truncation (in both the streamwise and the normal directions). The results of this work show clearly that the bifurcation behavior exhibited by the 10D model persists as the non-zero streamwise modes are added. For larger values of the eddy viscosity parameter, behavior similar to the 10D model is seen. As this parameter is reduced, more exotic bifurcations are seen in which the newly added non-zero streamwise modes also participate in the heteroclinic cycles by providing additional directions of instability. From the dynamical systems viewpoint, a linear analysis of the system around the fixed point was able to explain this intermittent behavior. An analysis of the quadratic terms was also carried out and it revealed that the delayed excitation of the higher order modes observed in the simulations was caused by nonlinear interactions. Solutions with a second normal mode also exhibited this type of

intermittent behavior. The POD modes obtained from experimental as well as numerical data were used in the simulations and the saddle-saddle connections were found from both types of data.

For the solutions displaying streamwise variations (1 and 2 normal modes) another new window of intermittency, which occurred at lower values of the eddy viscosity parameter, was discovered. The zero streamwise modes stay active all the time displaying an irregular behavior, whereas during the 'bursts' the non-zero streamwise modes also become active. This represents a generalized heteroclinic connection between limit sets. While the heteroclinic connections from the fixed points in the 10D model are a direct consequence of the O(2) symmetry exhibited by the equations (Armbruster *et al.* 1988), the explanation for the IV window of intermittency is still an open question from the view point of the dynamical systems community. It is speculated that it is caused by the $O(2)\times SO(2)$ equivariance of the models showing streamwise variations (P. Holmes, private communication 1990).

In order to analyze the intermittent behavior, a new approach of taking the POD in the homogeneous directions (the streamwise and spanwise) of the solutions in the different windows of intermittency was tried. This approach was able to separate out the fixed points and the unstable manifolds from the solutions in the first three windows (exactly like the linear analysis of the fixed point instability). However, for the fourth window it did not reveal any new results except that it separated the zero and the non-zero streamwise modes. Since the results of this approach were exactly the same as that of the linear analysis, this was not reported in this work but this represents a possible technique of analyzing chaotic bifurcations. In this context, it is relevant to refer the reader to the work of Aubry *et al.* (1991) in which a 'more general form' of the POD (termed as the biorthogonal decomposition) has been used as a technique to analyze the dynamics in spatially and temporally evolving flows.

Next, the physical flow quantities were studied in the different windows of intermittency. Different types of coherent structures as reported in the turbulence literature were derived from these simulations. The accomplishments of this analysis were two-fold. Firstly, the presence of all the types of structures occurring in the near-wall region was verified. This establishes the validity of these low dimensional models. Secondly, from the simple fixed point solutions, a relationship between various types of structures was proposed and was verified for the more complex solutions. Interesting dynamics like streak-merging, which had been observed in the experiments, was found in a typical time-varying solution.

For a given set of truncations, criteria were formulated to find the optimum value of the eddy-viscosity parameter. This analysis was based on the ratio of energy in the truncated system at a given value of α and the energy in the full (untruncated) system. For the optimum value of α, thus obtained, the rms values of the velocity components, Reynolds stress and mean velocity were computed as a function of the distance from the wall and were then compared with the experimental data. A very good agreement was found, and in particular the logarithmic variation of the mean velocity was observed in the outer part of the buffer layer.

Next, the POD was applied to the vorticity field. The main result of this part of the investigation is the utilization of the POD data of the velocity modes to obtain the vorticity modes. This technique was demonstrated for the near-wall region of the turbulent boundary layer and vortical structures were derived for a typical solution. The POD data for the velocity modes have been generated for different flows and can be used to derive the vorticity modes for all these flows. However, a full exploitation of the vorticity modes will involve a derivation of a set of ODEs by taking a Galerkin projection of the vorticity modes on the vorticity equation. This equation will also have velocity terms but they can be taken care of by using the relation between the time coefficients of vorticity and velocity derived in this work. The obvious advantage of such an approach is the absence of the pressure

term, but the eddy viscosity modelling will be different from the one used in this work. Such an investigation for the boundary layer flow will be carried out in the future.

Finally, a dynamic eddy viscosity model based on the combination of the AIM and the POD techniques is proposed. For the cases studied in this work, the iterative scheme employed in the method did not converge.

Appendix A.

Equations for the coefficients of the ODEs

Coefficient of the linear term:

$$b_k^{(n)(m)} = b^1 + b^2.$$

$$b^1 = \sqrt{L_1 L_3} \int_0^{X_2} \left\{ -\left(1 - \frac{x_2}{H}\right) \phi_{2_k}^{(m)} \phi_{i_k}^{(n)*} - ilx_2 \left(1 - \frac{x_2}{2H}\right) \phi_{i_k}^{(m)} \phi_{i_k}^{(n)*} \right\} dx_2.$$

(part of interaction with mean velocity)

$$b^2 = \sqrt{L_1 L_3} \left[(l^2 + k^2)\delta_{mn} + \int_0^{X_2} \left\{ D^2 \phi_{i_k}^{(m)} \phi_{i_k}^{(n)*} \right\} dx_2 \right].$$

(viscous term)

Coefficient of the quadratic term:

$$c_{kk'}^{(n)(p)(q)} = -(1 - \delta_{k0}) \int_0^{X_2} \phi_{j_{k'}}^{(p)} \Omega_{k_j - k_{j'}} \phi_{i_{k-k'}}^{(q)} \phi_{i_k}^{(n)*} dx_2.$$

Coefficient of the cubic term:

$$d_{kk'}^{(n)(p)(q)(r)} = \frac{-1}{\sqrt{L_1 L_3}}\left(\int_0^{X_2} \phi_{1k'}^{(p)} \phi_{2k'}^{(q)*} \phi_{ik}^{(n)*} \phi_{2k}^{(r)} dx_2 + il \int_0^{X_2} \phi_{ik}^{(n)*} \phi_{ik}^{(r)} \left\{ \int_0^{x_2} \phi_{1k'}^{(p)} \phi_{2k'}^{(q)*} dx_{2'} \right\} dx_2 \right).$$

1. i denotes the complex number, $\sqrt{-1}$.

2. D denotes the derivative with respect to x_2: $D = \frac{d}{dx_2}$.

3. k denotes the wavenumber (l,k).

4. $\Omega_{k_j} = ik_j$ if $j = 1,3$

   $= D$ if $j = 2$.

Appendix B

Eigenvalues of the 32 dimensional system linearized about a fixed point for the different subsystems.

α	Eigenvalues of the subsystem (Re a_{02}, Re a_{04})
1.50	-15.823 -1.199
1.40	-13.684 -6.308
1.30	(-11.513, 1.922)
1.20	-14.772 -11.442
1.10	-20.806 -8.926
1.00	-26.885 -7.024
0.95	-30.236 -6.172
0.90	-33.907 -5.385
0.89	-34.687 -5.236
0.88	-35.483 -5.089
0.87	-36.297 -4.945
0.86	-37.130 -4.804
0.85	-37.981 -4.665

α	Eigenvalues of the subsystem (Im a_{02}, Im a_{04})
1.50	-15.824 0.000
1.40	-13.793 0.000
1.30	-11.657 0.000
1.20	-9.392 0.000
1.10	-6.966 0.000
1.00	-4.358 0.000
0.95	-2.988 0.000
0.90	-1.585 0.000
0.89	-1.302 0.000
0.88	-1.019 0.000
0.87	-0.735 0.000
0.86	-0.451 0.000
0.85	-0.167 0.000

α	Eigenvalues of the subsystem (Re a_{01}, Re a_{03}, Re a_{05})
1.50	-37.336 -4.634 -1.573
1.40	-33.639 (-3.337, 1.391)
1.30	-29.870 (-3.368, 2.200)
1.20	-26.019 (-3.314, 2.604)
1.10	-22.080 (-3.195, 2.739)
1.00	-18.051 (-3.018, 2.493)
0.95	-15.993 (-2.920, 2.078)
0.90	-13.875 (-2.839, 1.050)
0.89	-13.437 (-2.829, 0.495)
0.88	-12.991 -3.662 -1.984
0.87	-12.536 -4.147 -1.497

0.86	-12.067 -4.538 -1.117
0.85	-11.579 -4.903 -0.784

α	Eigenvalues of the subsystem (Im a_{01}, Im a_{03}, Im a_{05})
1.50	-37.336 -4.694 0.004
1.40	-33.640 -3.731 0.453
1.30	-29.876 -2.654 0.420
1.20	-26.042 -0.987 -0.321
1.10	-22.156 (-0.216, 1.476)
1.00	-18.287 (0.221, 2.089)
0.95	-16.408 (0.450, 2.316)
0.90	-14.612 (0.693, 2.502)
0.89	-14.266 (0.744, 2.534)
0.88	-13.925 (0.796, 2.565)
0.87	-13.591 (0.849, 2.594)
0.86	-13.262 (0.903, 2.620)
0.85	-12.940 (0.958, 2.645)

α	Eigenvalues of the subsystem (a_{-11}, a_{-13}, a_{-15}, a_{11}, a_{13} and a_{15})
1.50	(-69.,149.) (-69.,102.) (-49.,123.) (-49.,123.) (-16.,94.) (-12.95,100.)
1.40	(-65.,145.) (-64., 96.) (-47.,120.) (-46.,119.) (-16.,88.) (-10.02,100.)
1.30	(-60.,140.) (-58., 90.) (-44.,117.) (-43.,114.) (-16.,83.) (-7.73, 99.)
1.20	(-55.,136.) (-53., 85.) (-41.,114.) (-40.,110.) (-16.,78.) (-5.61, 97.)
1.10	(-50.,131.) (-48., 79.) (-38.,111.) (-37.,106.) (-15.,73.) (-3.55, 95.)
1.00	(-45.,126.) (-43., 73.) (-34.,108.) (-33.,102.) (-15.,68.) (-1.52, 92.)
0.95	(-43.,123.) (-41., 71.) (-32.,106.) (-32.,100.) (-14.,65.) (-0.53, 90.)

0.90	(-40.,120.)	(-38., 68.)	(-30., 98.)	(-30.,104.)	(-14.,62.) (0.41, 88.)
0.89	(-40.,119.)	(-38., 68.)	(-30., 97.)	(-29.,103.)	(-13.,61.) (0.58, 88.)
0.88	(-39.,118.)	(-38., 67.)	(-30., 97.)	(-28.,103.)	(-13.,61.) (0.76, 87.)
0.87	(-39.,118.)	(-37., 67.)	(-29., 96.)	(-28.,102.)	(-13.,60.) (0.93, 87.)
0.86	(-38.,117.)	(-37., 66.)	(-29., 96.)	(-27.,102.)	(-13.,59.) (1.10, 86.)
0.85	(-38.,116.)	(-36., 66.)	(-29., 95.)	(-27.,102.)	(-13.,59.) (1.26, 86.)

α	Eigenvalues of the subsystem (a_{-12}, a_{-14}, a_{10}, a_{12}, a_{14})				
1.50	(-67.,17.)	(-56.,135.)	(-56.,135.)	(-31.,100.)	(-31.,100.)
1.40	(-63.,19.)	(-52.,131.)	(-52.,131.)	(-29., 96.)	(-29., 98.)
1.30	(-59.,21.)	(-49.,127.)	(-48.,127.)	(-27., 92.)	(-26., 96.)
1.20	(-54.,22.)	(-45.,122.)	(-45.,123.)	(-25., 88.)	(-24., 93.)
1.10	(-50.,24.)	(-41.,118.)	(-41.,118.)	(-23., 84.)	(-21., 91.)
1.00	(-45.,25.)	(-37.,113.)	(-37.,114.)	(-21., 79.)	(-19., 89.)
0.95	(-42.,26.)	(-35.,111.)	(-35.,112.)	(-20., 76.)	(-17., 88.)
0.90	(-40.,26.)	(-33.,108.)	(-32.,109.)	(-19., 73.)	(-16., 87.)
0.89	(-39.,26.)	(-33.,107.)	(-32.,109.)	(-18., 72.)	(-15., 87.)
0.88	(-39.,26.)	(-32.,107.)	(-32.,108.)	(-18., 72.)	(-15., 87.)
0.87	(-38.,27.)	(-32.,106.)	(-31.,107.)	(-18., 71.)	(-15., 86.)
0.86	(-38.,27.)	(-31.,105.)	(-31.,107.)	(-18., 70.)	(-15., 86.)
0.85	(-37.,27.)	(-31.,105.)	(-30.,106.)	(-17., 70.)	(-14., 86.)

1. (a,b) denotes the complex conjugate pair a+ib, a-ib.

Appendix C

Eigenvalues of the 54 dimensional system linearized about a fixed point for the different subsystems.

α	Eigenvalues of the subsystem (Re a_{02}, Re a_{04})
2.10	-15.617 -2.101
2.00	-14.109 -5.701
1.90	-11.898 -10.031
1.85	(-11.503, 1.797)
1.75	(-12.608, 1.591)
1.65	-17.030 -10.517
1.55	-21.143 -8.936
1.45	-25.372 -7.567
1.40	-27.616 -6.931
1.35	-29.982 -6.327
1.30	-32.501 -5.757
1.25	-35.204 -5.219
1.22	-36.926 -4.912
1.21	-37.518 -4.812
1.20	-38.120 -4.714
1.19	-38.731 -4.616

α	Eigenvalues of the subsystem (Im a_{02}, Im a_{04})
2.10	-15.622 0.000
2.00	-14.184 0.000
1.90	-12.696 0.000
1.85	-11.931 0.000
1.75	-10.352 0.000
1.65	-8.699 0.000
1.55	-6.962 0.000
1.45	-5.133 0.000
1.40	-4.184 0.000
1.35	-3.215 0.000
1.30	-2.228 0.000
1.25	-1.229 0.000
1.22	-0.626 0.000
1.21	-0.425 0.000
1.20	-0.224 0.000
1.19	-0.024 0.000

α	Eigenvalues of the subsystem (Re a_{01}, Re a_{03}, Re a_{05})
2.10	-36.671 -4.480 -2.357
2.00	-34.062 (-3.553, 1.309)
1.90	-31.417 (-3.588, 1.975)
1.85	-30.080 (-3.585, 2.195)
1.75	-27.374 (-3.550, 2.513)
1.65	-24.624 (-3.482, 2.701)
1.55	-21.828 (-3.383, 2.757)

1.45	-18.982 (-3.258, 2.630)
1.40	-17.538 (-3.189, 2.457)
1.35	-16.074 (-3.121, 2.160)
1.30	-14.577 (-3.062, 1.627)
1.25	-13.018 -3.529 -2.531
1.22	-12.020 -4.651 -1.432
1.21	-11.669 -4.929 -1.181
1.20	-11.304 -5.203 -0.948
1.19	-10.920 -5.483 -0.729

α	Eigenvalues of the subsystem (Im a_{01}, Im a_{03}, Im a_{05})
2.10	-36.671 -4.672 -0.164
2.00	-34.062 -3.973 0.110
1.90	-31.420 -3.221 0.143
1.85	-30.085 -2.804 0.087
1.75	-27.389 -1.749 -0.288
1.65	-24.659 (-0.695, 1.032)
1.55	-21.909 (-0.382, 1.630)
1.45	-19.164 (-0.069, 2.047)
1.40	-17.810 (0.091, 2.219)
1.35	-16.480 (0.255, 2.371)
1.30	-15.189 (0.426, 2.504)
1.25	-13.950 (0.607, 2.619)
1.22	-13.239 (0.720, 2.678)
1.21	-13.008 (0.759, 2.696)
1.20	-12.781 (0.799, 2.713)
1.19	-12.556 (0.839, 2.728)

α	Eigenvalues of the subsystem (a_{-11}, a_{-13}, a_{-15}, a_{11}, a_{13} and a_{15})					
2.10	(-69.,155.)	(-68.,103.)	(-48.,130.)	(-48.,129.)	(-17.,100.)	(13.70,107.)
2.00	(-65.,152.)	(-65., 99.)	(-47.,128.)	(-46.,126.)	(-18., 96.)	(-11.64,107.)
1.90	(-62.,149.)	(-61., 95.)	(-45.,125.)	(-44.,123.)	(-18., 92.)	(-9.90,107.)
1.85	(-60.,147.)	(-59., 93.)	(-44.,124.)	(-43.,122.)	(-18., 90.)	(-9.08,106.)
1.75	(-57.,144.)	(-55., 89.)	(-42.,122.)	(-41.,119.)	(-17., 87.)	(-7.51,105.)
1.65	(-53.,141.)	(-52., 85.)	(-40.,120.)	(-39.,116.)	(-17., 83.)	(-5.97,104.)
1.55	(-50.,137.)	(-48., 81.)	(-38.,118.)	(-36.,113.)	(-16., 80.)	(-4.46,102.)
1.45	(-47.,134.)	(-45., 77.)	(-35.,115.)	(-34.,110.)	(-16., 76.)	(-2.97,100.)
1.40	(-45.,132.)	(-43., 75.)	(-34.,114.)	(-33.,109.)	(-16., 74.)	(-2.24, 99.)
1.35	(-43.,130.)	(-41., 73.)	(-32.,113.)	(-32.,107.)	(-15., 72.)	(-1.52, 98.)
1.30	(-41.,128.)	(-39., 71.)	(-31.,106.)	(-30.,111.)	(-15., 70.)	(-0.83, 96.)
1.25	(-39.,125.)	(-38., 69.)	(-30.,104.)	(-29.,110.)	(-14., 68.)	(-0.17, 95.)
1.22	(-38.,124.)	(-37., 68.)	(-29.,103.)	(-27.,109.)	(-14., 67.)	(0.20, 94.)
1.21	(-38.,124.)	(-36., 68.)	(-29.,103.)	(-27.,109.)	(-14., 66.)	(0.32, 94.)
1.20	(-38.,123.)	(-36., 68.)	(-29.,102.)	(-27.,109.)	(-14., 66.)	(0.44, 93.)
1.19	(-37.,123.)	(-36., 67.)	(-28.,102.)	(-26.,108.)	(-14., 65.)	(0.55, 93.)

α	Eigenvalues of the subsystem (a_{-12}, a_{-14}, a_{10}, a_{12}, a_{14})				
2.10	(-67., 24.)	(-55.,141.)	(-55.,141.)	(-31.,107.)	(-31.,107.)
2.00	(-64., 25.)	(-53.,138.)	(-53.,138.)	(-29.,104.)	(-29.,105.)
1.90	(-61., 26.)	(-50.,135.)	(-50.,135.)	(-28.,101.)	(-27.,104.)
1.85	(-60., 27.)	(-49.,133.)	(-49.,134.)	(-27.,100.)	(-27.,103.)
1.75	(-57., 28.)	(-46.,131.)	(-46.,131.)	(-26., 97.)	(-25.,101.)
1.65	(-53., 29.)	(-44.,128.)	(-44.,128.)	(-24., 94.)	(-23., 99.)
1.55	(-50., 30.)	(-41.,124.)	(-41.,125.)	(-23., 90.)	(-21., 98.)
1.45	(-47., 31.)	(-38.,121.)	(-38.,122.)	(-21., 87.)	(-19., 96.)

1.40	(-45., 32.)	(-37.,119.)	(-36.,120.)	(-21., 85.)	(-18., 96.)
1.35	(-43., 32.)	(-35.,117.)	(-35.,119.)	(-20., 83.)	(-17., 95.)
1.30	(-42., 32.)	(-34.,115.)	(-33.,117.)	(-19., 81.)	(-16., 94.)
1.25	(-40., 33.)	(-33.,113.)	(-32.,115.)	(-18., 79.)	(-15., 94.)
1.22	(-39., 33.)	(-32.,112.)	(-31.,114.)	(-18., 77.)	(-15., 93.)
1.21	(-38., 33.)	(-31.,112.)	(-31.,113.)	(-18., 77.)	(-14., 93.)
1.20	(-38., 33.)	(-31.,111.)	(-30.,113.)	(-17., 77.)	(-14., 93.)
1.19	(-37., 33.)	(-31.,111.)	(-30.,112.)	(-17., 76.)	(-14., 93.)

α	Eigenvalues of the subsystem (a_{-21}, a_{-23}, a_{-25}, a_{21}, a_{23} and a_{25})					
2.10	(-118.,171.)	(-118.,248.)	(-94.,226.)	(-94.,227.)	(-36.,232.)	(-32.51,243.)
2.00	(-112.,165.)	(-111.,245.)	(-90.,221.)	(-89.,224.)	(-36.,224.)	(-30.14,242.)
1.90	(-107.,158.)	(-105.,242.)	(-87.,216.)	(-85.,222.)	(-36.,217.)	(-28.06,240.)
1.85	(-104.,155.)	(-102.,240.)	(-85.,214.)	(-82.,220.)	(-36.,214.)	(-27.06,239.)
1.75	(-98.,149.)	(-96.,237.)	(-80.,209.)	(-78.,217.)	(-36.,207.)	(-25.08,236.)
1.65	(-93.,143.)	(-90.,233.)	(-76.,204.)	(-73.,214.)	(-37.,200.)	(-23.09,232.)
1.55	(-87.,136.)	(-84.,230.)	(-72.,200.)	(-68.,211.)	(-37.,193.)	(-21.04,228.)
1.45	(-82.,130.)	(-78.,225.)	(-67.,195.)	(-62.,208.)	(-37.,186.)	(-18.92,223.)
1.40	(-79.,127.)	(-75.,223.)	(-65.,193.)	(-60.,206.)	(-37.,181.)	(-17.82,220.)
1.35	(-76.,124.)	(-73.,220.)	(-63.,191.)	(-57.,205.)	(-37.,177.)	(-16.70,217.)
1.30	(-74.,121.)	(-70.,217.)	(-61.,188.)	(-54.,203.)	(-37.,172.)	(-15.57,214.)
1.25	(-71.,118.)	(-68.,213.)	(-59.,186.)	(-51.,201.)	(-37.,168.)	(-14.43,211.)
1.22	(-70.,116.)	(-66.,211.)	(-58.,184.)	(-50.,200.)	(-37.,165.)	(-13.75,208.)
1.21	(-69.,115.)	(-66.,210.)	(-58.,184.)	(-49.,199.)	(-37.,164.)	(-13.52,207.)
1.20	(-69.,115.)	(-65.,209.)	(-58.,183.)	(-48.,199.)	(-36.,163.)	(-13.30,207.)
1.19	(-68.,114.)	(-65.,208.)	(-58.,183.)	(-48.,199.)	(-36.,162.)	(-13.08,206.)

α	Eigenvalues of the subsystem (a_{-22}, a_{-24}, a_{20}, a_{22}, a_{24})				
2.10	(-102.,234.)	(-102.,234.)	(-71.,203.)	(-71.,204.)	(-45.,304.)
2.00	(-97.,231.)	(-97.,231.)	(-68.,199.)	(-68.,201.)	(-43.,296.)
1.90	(-92.,227.)	(-91.,227.)	(-66.,194.)	(-66.,198.)	(-41.,287.)
1.85	(-89.,226.)	(-89.,226.)	(-64.,192.)	(-64.,196.)	(-40.,282.)
1.75	(-84.,222.)	(-84.,223.)	(-62.,193.)	(-62.,187.)	(-38.,273.)
1.65	(-79.,219.)	(-78.,219.)	(-59.,190.)	(-59.,182.)	(-36.,265.)
1.55	(-75.,215.)	(-73.,215.)	(-56.,187.)	(-56.,177.)	(-34.,256.)
1.45	(-70.,211.)	(-68.,211.)	(-54.,184.)	(-53.,171.)	(-31.,247.)
1.40	(-68.,208.)	(-65.,209.)	(-52.,183.)	(-51.,168.)	(-30.,242.)
1.35	(-66.,205.)	(-63.,207.)	(-51.,181.)	(-50.,164.)	(-29.,238.)
1.30	(-64.,202.)	(-60.,204.)	(-50.,180.)	(-48.,161.)	(-28.,233.)
1.25	(-62.,199.)	(-57.,201.)	(-49.,178.)	(-46.,157.)	(-27.,228.)
1.22	(-60.,197.)	(-56.,199.)	(-48.,177.)	(-45.,155.)	(-26.,225.)
1.21	(-60.,196.)	(-55.,198.)	(-48.,177.)	(-45.,154.)	(-26.,224.)
1.20	(-59.,196.)	(-55.,197.)	(-48.,177.)	(-45.,154.)	(-26.,223.)
1.19	(-59.,195.)	(-54.,197.)	(-48.,176.)	(-45.,153.)	(-25.,222.)

1. (a,b) denotes the complex conjugate pair a+ib, a-ib.

Bibliography

Acarlar, M. S. and Smith, C. R. 1987 A study of hairpin vortices in a laminar boundary layer. Part 2: Hairpin vortices generated by fluid injection. *J. Fluid Mech.* **175**, 43-83.

Achia, B. U. and Thompson, D. W. 1976 Structure of the turbulent boundary layer in drag reducing pipe flow. *J. Fluid Mech.* **81**, 439-64.

Armbruster, D., Guckenheimer, J. and Holmes, P. 1988 Heteroclinic cycles and modulated travelling waves in systems with 0(2) symmetry. *Physica* **29D**, 257-282.

Aubry, N. 1987 A dynamical system / coherent structure approach to the fully developed turbulent wall layer. Ph. D. thesis, Cornell University.

Aubry, N., Guyonet, R., and Lima, R. 1991 Spatio-temporal analysis of complex signals: theory and applications. *J. Statist. Phys.* **64 (3/4)**, 683-739.

Aubry, N., Holmes, P., Lumley, J.L., and Stone, E. 1988 The dynamics of coherent structures in the wall region of a turbulent boundary layer. *J. Fluid Mech.* **192**, 115-173.

Aubry, N. and Lian, W. Y. 1991 Analysis of spatio-temporal complexity in the Kuramoto-Sivashinsky equation. *Physica D*, submitted.

Aubry, N. and Sanghi, S. 1989 Streamwise and spanwise dynamics in the turbulent wall layer. In *Forum on Chaotic Flow*, ed. K.N. Ghia. New York: ASME.

Aubry and Sanghi, S. 1990 Bifurcations and bursting of streaks in the turbulent wall layer. In *Turbulence and Coherent Structures*, (eds. M. Lesieur and O. Métais). Dordrecht: Kluwer.

Bakewell, P & Lumley, J.L. 1967 Viscous sublayer and adjacent wall region in turbulent pipe flow. *Phys. Fluids* **10**, 1880-89.

Balint, J. -L., Wallace, J. M. and Vukoslavcevic, P. 1991 The velocity and vorticity vector fields of a turbulent boundary layer. Part 2. Statistical properties. *J. Fluid Mech.* **228**, 53-86.

Berkooz, G. 1991 Turbulence, coherent structures, and low dimensional models. Ph.D. thesis, Cornell University.

Berkooz, G., Holmes, P.J. and Lumley, J.L. 1991 Intermittent dynamics in simple models of the turbulent wall layer. *J. Fluid Mech.* **230**, 75-95.

Blackwelder, R. F. & Eckelmann, H. 1979 Streamwise vortices associated with the bursting phenomenon. *J. Fluid Mech.* **94** (3), 577-594.

Blackwelder, R. F. & Kaplan, R. E. 1976 On the wall structure of the turbulent boundary layer. *J. Fluid Mech.* **76**, 89-112.

Blackwelder, R. F.& Swearingen, J. D. 1989 The role of inflectional velocity profiles in wall bounded flows In *Near Wall Turbulence*, (eds. S. J. Kline and N. H. Afgan), pp.268-288. New York: Hemisphere.

Bogard, D. G. & Tiederman, W. G. 1986 Burst detection with single point velocity measurements. *J. Fluid Mech.* **162**, 389-413.

Bogard, D. G. & Tiederman, W. G. 1987 Characteristics of ejections in turbulent channel flow. *J. Fluid Mech.* **179**, 1-19.

Breuer, K. S. & Haritonidis, J. H. 1990 The evolution of a localized disturbance in a laminar boundary layer. Part 1. Weak disturbances. *J. Fluid Mech.* **220**, 569-94.

Breuer, K. S. & Landahl, M. T. 1990 The evolution of a localized disturbance in a laminar boundary layer. Part 2. Strong disturbances. *J. Fluid Mech.* **220**, 595-621.

Bridges, J., Hussain, H. S. & Hussain, F. 1990 Whither coherent structures? Comment 1. In *Whither Turbulence: Turbulence at the Crossroads* (ed. J. L. Lumley), Springer Lecture Notes in Physics, **357**, pp. 132-151. New York: Springer Verlag.

Brodkey, R. S., Wallace J. M. & Eckelmann, H. 1974 Some properties of truncated turbulence signals in bounded shear flows. *J. Fluid Mech.* **63**, 209-24.

Chambers, D. H., Adrian, R. J., Moin, P. and Sung, H. J. 1988 Karhunen Loeve expansion of Burger's model of turbulence. *Phys. Fluids* **31**, 2573-82.

Champneys, A. R. 1991 Homoclinic orbits in the dynamics of articulated pipes conveying fluid. Preprint.

Chong, M. S., Perry, A. E. and Cantwell, B. J. 1990. A general classification of three-dimensional flow fields. *Phys. Fluids A* **2** (5), 765-77.

Constantin, P. 1987 In *Proceedings of the AMS/SIAM summer conference on the connection between finite and infinite dimensional systems, Boulder, Col. 1987*, (eds. Foias et al.).

Constantin, P., Foias, C., Nicolaenko, B. and Temam, R. 1988 Integral manifolds and inertial manifolds for dissipative partial differential equations. *Appl. Math. Sciences* No. **70**, New York: Springer Verlag.

Constantin, P., Foias, C., Nicolaenko, B. and Temam, R. 1990 Spectral barriers and inertial manifolds for dissipative partial differential equations. *J. Dynamics and Diff. Eqns.* **1**, 45-73.

Corino, E.R. & Brodkey, R.S. 1969 A visual investigation of the wall region in turbulent flow. *J. Fluid Mech.* **37**, 1-30.

Corrsin, S. 1957 Some current problems in shear flows. In *Proc. Naval Hydr. Symp. 24-28 Sept. 1956*, (ed. F. S. Sheman).

Curry, J. H. 1978. Generalized Lorenz systems. *Commun. Math. Phys.* **60**, 193-204.

Curry, J. H., Herring, J. R., Loncaric, J. & Orszag, S.A. 1984 Order and disorder in two- and three-dimensional Benard convection. *J. Fluid Mech.* **147**, 1-38.

Deane, A. E., Kevrekidis, I. G., Karniadakis, G. E. and Orszag, S. A. 1991 Low-dimensional models for complex geometry flows: application to grooved channels and circular cylinders. *Phys. Fluids A* **3 (10)**, 2337-54.

Dresselhaus, E. and Tabor, M. 1989 The persistence of strain in dynamical systems. Preprint, Columbia University. To appear in *J. Phys. A.*

Doering, C. R., Gibbon, J. D., Holm, D. D. and Nicolaenko, B. 1988 Low dimensional behavior in the complex Ginzburg-Landau equation. *Nonlinearity* **1**, 279-309.

Eckelmann, H. 1974 The structure of the viscous sublayer and the adjacent wall region in a turbulent channel flow. *J. Fluid Mech.* **65 (3)**, 439-59.

Foias, C., Manley, O. P. and Temam, R. 1988a Modelling of the interaction of the small and large eddies in two dimensional turbulent flows. *Math. Modelling Numerical Anal.* **22**, 93-118.

Foias, C., Manley, O. P. and Temam, R. 1991 Approximate inertial manifolds and effective viscosity in turbulent flows. *Phys. Fluids A* **3 (5)**, 898-911.

Foias, C., Sell, G. R. and Temam, R. 1988b Inertial manifolds for nonlinear evolutionary equations. *J. Diff. Eqns.* **73**, 309-53.

Foias, C. and Temam, R. 1988 The algebraic approximation of attractors: the finite dimensional case. *Physica* **28 D**, 282-304.

Fortuna, G. and Hanratty, T. J. 1972 The influence of drag-reducing polymers on turbulence in the viscous sublayer. *J. Fluid Mech.* **53 (3)**, 575-86.

George, W. K. 1989 Insight into the dynamics of coherent structures from a proper orthogonal decomposition. In *Near Wall Turbulence*, (eds. S. J. Kline and N. H. Afgan), pp. 469-487. New York: Hemisphere.

Glauser, M. N. 1987 Ph.D. thesis, Department of mechanical engineering, University of Buffalo, SUNY, Buffalo, NY.

Glezer, A., Kadioglu, Z. and Pearlstein, A. J. 1989 Development of an extended proper orthogonal decomposition and its application to a time periodically forced plane mixing layer. *Phys. Fluids A* **1**, 1363-73.

Grass, A. J. 1971 Structural features of turbulent flow over smooth and rough boundaries. *J. Fluid Mech.* **50**, 233-55.

Guezennec, Y. G., Piomelli, U. and Kim, J. 1989 On the shape and dynamics of wall structures in turbulent channel flows. *Phys. Fluids A* **1 (4)**, 764-66.

Gupta, A. K., Laufer,J. and Kaplan,R. E. 1971 Spatial structure in the viscous sublayer. *J. Fluid Mech.* **50**, 493-512.

Hatziavramidis, D. T. and Hanratty, T. J. 1979 The representation of the viscous wall region by a regular eddy pattern. *J. Fluid Mech.* **95 (4)**, 655-79.

Head, M.R. and Bandyopadhyay, P. 1981 New aspects of turbulent boundary layer structure. *J. Fluid Mech.* **107**, 297-338.

Herzog, S. 1986 The large scale structure in the near-wall region of turbulent pipe flow. Ph.D. thesis, Cornell University.

Holmes, P. 1990 Can dynamical systems approach turbulence? In *Whither Turbulence: Turbulence at the Crossroads* (ed. J. L. Lumley), Springer Lecture Notes in Physics, **357**, pp. 197-249. Springer Verlag, New York.

Hunt, J. C. R., Wray A. A. and Moin, P. 1988 Eddies, streams, and convergence zones in turbulent flows. In *Proc. 1988 Summer Program Cent. Turbul. Res.* pp. 193-207, Stanford, Calif: Cent. Turbul. Res.

Hussain, A. K. M. F. 1986 Coherent structures and turbulence. *J. Fluid Mech.* **173**, 303-56.

Jang, P. S., Benney, D. J. & Gran, R. L. 1986 On the origin of streamwise vortices in a turbulent boundary layer. *J. Fluid Mech.* **169**, 109-123.

Jimenez, J., Moin, P. , Moser, R.& Keefe, L. 1988 Ejection mechanisms in the sublayer of a turbulent channel. *Phys. Fluids* **31 (6)**, 1311-1313.

Jimenez, J.and Moin, P. 1990 The minimal flow unit in near-wall turbulence. *J. Fluid Mech.* **225**, 213-40.

Johansson, A. V., Alfredsson, P. H., & Eckelmann, H. 1987 On the evolution of shear-layer structures in near-wall turbulence. In *Advances in Turbulence*. pp. 383-90. Berlin: Springer Verlag.

Jolly, M. S 1988 Explicit construction of an inertial manifold for a reaction diffusion equation. *J. Diff. Eqns.* **77**.

Jolly, M. S., Kevrekidis, I. G. and Titi, E. S. 1990 Approximate inertial manifolds for the Kuramato-Sivashinsky equation: analysis and computations. *Physica* **44** D, 38.

Jones, D. A. and Titi, E. S. 1991 A remark on quasi-stationary approximate inertial manifolds for the Navier-Stokes equations. Preprint, Cornell University, Ithaca, New York.

Kim, J. 1985 Turbulence structures associated with the bursting event. *Phys. Fluids* **28**, 52-58.

Kim, J. 1987 Evolution of a vortical structure associated with the bursting event in a channel flow. In *Turbulent shear flows 5*, pp.221-233. Berlin: Springer Verlag.

Kim, H. T., Kline, S. J. and Reynolds, W. C. 1971 The production of turbulence near a smooth wall in a turbulent boundary layer *J. Fluid Mech.* **50**, 133-160.

Kim, J. and Moin,.P. 1986 The structure of vorticity field in turbulent channel flow. Part 2. Study of ensemble-averaged fields *J Fluid Mech.* **162**, 339-363

Kim, J., Moin,.P., and Moser, R. D. 1987 Turbulence statistics in fully developed channel flow at low Reynolds number. *J. Fluid Mech.* **177**, 133-166.

Kirby, M. and Armbruster, D. 1991 Reconstructing phase space for pde simulations. Preprint.

Kline, S.J., Reynolds, W.C., Schraub, F.A. and Runstadler, P.W. 1967 *The* structure of turbulent boundary layers. *J. Fluid Mech.* **30**, 741-773.

Kline, S.J. and Robinson, S.K.1989 Quasi-coherent structures in the turbulent boundary layer: Part I. Status report on a community-wide summary of the data. In *Near Wall Turbulence*, (eds. S. J. Kline and N. H. Afgan), pp.200-217. New York: Hemisphere.

Kreplin, H. -P., and Eckelmann, H. 1979 Propagation of perturbations in the viscous sublayer and adjacent wall region. *J. Fluid Mech.* **95**, 305-22.

Lee, M. K., Eckelmann, L. D. and Hanratty, T. J. 1974 Identification of turbulent wall eddies through the phase relation of the components of the fluctuating velocity gradient. *J. Fluid Mech.* **66**, 17-33.

Leibovich, S. and Mahalov, A. 1990 Resonant interactions in rotating pipe flow. (submitted to *J. Fluid Mech.*).

Loève, M. 1955 *Probability Theory*. Van Nostrand.

Lu, S. S. and Willmarth, W. W. 1973 Measurements of the structure of the Reynolds stress in a turbulent boundary layer. *J. Fluid Mech.* **60**, 481-511.

Lumley, J.L. 1967 The structure of inhomogeneous turbulent flows. In *Atmospheric Turbulence and Radio Wave Propagation* (eds. A.M. Yaglom & V.I. Tatarski), pp 166-178 Moscow: Nauka.

Lumley, J.L. 1977 Drag reduction in two phase and polymer flows. *Phys. Fluids* **20 (10, II)**, S64-71.

Mallet-Paret, J. and Sell, G. R. 1988 Inertial manifolds for reaction diffusion equations in higher space dimensions. *J. Amer. Math. Soc.* **1**, 805-66.

Mitchell, J. E. and Hanratty, T. J. 1966 A study of turbulence at a wall using an electrochemical wall shear-stress meter. *J. Fluid Mech.* **26 (1)**, 199-221.

Moffatt, H. K. 1990 Fixed points of turbulent dynamical systems and suppression of nonlinearity. In *Whither Turbulence: Turbulence at the Crossroads* (ed. J. L. Lumley), Springer Lecture Notes in Physics, **357**, pp. 250-257. New York: Springer Verlag.

Moin, P. 1984 Probing turbulence via large eddy simulation. *AIAA Pap. No. 84-0174.*

Moin, P. 1987 Analysis of turbulence data generated by numerical simulations. *AIAA Pap. No. 87-0194.*

Moin, P. and Kim, J. 1982 Numerical investigation of turbulent channel flow. *J. Fluid Mech.* **118**, 341-377.

Moin, P. and Kim, J. 1985 The structure of the vorticity field in turbulent channel flow. Part 1: analysis of instantaneous fields and statistical correlations. *J. Fluid Mech.* **155**, 441-64.

Moin, P. and Moser, R.D. 1989 Characteristic-eddy decomposition of turbulence in a channel, *J. Fluid Mech.* **200**, 471-509.

Mullin, T. and Darbyshire, A.G. 1990 Intermittency in a rotating annular flow. (submitted to *Europhys. Lett. A*).

Nakagawa, H. and Nezu, I. 1981 Structure of space-time correlations of bursting phenomena in an open-channel flow. *J. Fluid Mech.* **104**, 1-43.

Nicolaenko, B 1987 In *Proceedings of the AMS/SIAM summer conference on the connection between finite and infinite dimensional systems, Boulder, Col. 1987*, (eds. Foias *et al.*).

Nicolaenko, B., Scheurer, B. and Temam, R. 1985. Some global dynamical properties of the Kuramato-Sivashinsky equations: nonlinear stability and attractors, *Physica* **16** *D*, 155-183.

Nicolaenko, B., Scheurer, B. and Temam, R. 1986. Attractors for the Kuramato-Sivashinsky equations, Los Alamos National Lab, Report LA-UR-85-1630.

Nicolaenko, B.and She, A.S. 1990. Symmetry breaking homoclinic chaos in the Kolmogorov flow. In *Topological Dynamics of Turbulence* (to appear), Cambridge University Press.

Oldaker, D. K. and Tiederman, W. G. 1977 Spatial structure of the viscous sublayer in drag-reducing channel flows. *Phys. Fluids* **20 (10, II)**, S133-44.

Reynolds, O. 1883 An experimental investigation of the circumstances which determine whether the motion of water shall be direct or sinuous, and the law of resistance in parallel channels. *Phil. Trans. R. Soc. Lond.* **174**, 935.

Robinson, S. K. 1991 Coherent motions in the turbulent boundary layer. *Ann. Rev. Fluid Mech.* **23**, 601-39.

Robinson, S.K., Kline, S.J. and Spalart, P.R. 1989 Quasi-coherent structures in the turbulent boundary layer: Part II. Verification and new information from a numerically simulated flat-plate layer. In *Near Wall Turbulence*, (eds. S. J. Kline and N. H. Afgan), pp.218-247. New York: Hemisphere.

Runstadler, P. G., Kline, S. J. and Reynolds, W. C. 1963 An experimental investigation of flow structure of the turbulent boundary layer. *Rep. No. MD-8*, Dep. of Mech. Eng. Stanford Univ., Stanford, Calif.

Sanghi, S. and Aubry, N. 1990 Models for the structure and dynamics of near wall turbulence. In *Studies in Turbulence: In Recognition of Contributions by John Lumley* (eds. Gatsky, Speziale and Sarkar), New York: Springer Verlag(in press).

Sirovich, L. 1989 Empirical eigenfunctions and low dimensional systems. In *New perspectives in turbulence, Newport conference proceedings, June 11-15, 1989, Newport, RI.* New York: Springer Verlag.

Sirovich, L., Ball, K. S. & Keefe, L. R. 1990 Plane waves and structures in turbulent channel flow. *Phys. Fluids.A* **2(12)**, 2217-2226.

Sirovich, L., Maxey, M. and Tarman, H. 1987 Analysis of turbulent thermal convection. In *Proc. 6th Symp. Turbulent Shear Flows,* (eds. F. Durst *et al.*), New York: Springer Verlag.

Sirovich, L. and Park, H. 1990 Turbulent thermal convection in a finite domain. Part I: Theory. Part II: Numerical simulations. *Phys. Fluids A* **2 (9)**, 1649-68.

Sirovich, L. and Rodriguez, J. D. 1987 Coherent structures and chaos: a model problem. *Phys. Lett. A* **120 (5)**, 212.

Smith, C. R. and Lu, L. J. 1989 The use of a template-matching technique to identify hairpin vortex flow structures in turbulent boundary layers. In *Near Wall Turbulence,* (eds. S. J. Kline and N. H. Afgan), pp.248-67. New York: Hemisphere.

Smith, C.R. and Metzler, S. P. 1983 The characteristics of low-speed streaks in the near-wall region of a turbulent boundary layer. *J. Fluid Mech.* **129**, 27-54.

Smith, C. R. & Schwartz, S.P. 1983 Observation of streamwise rotation in the near-wall region of a turbulent boundary layer. *Phys. Fluids* **26(3)**, 641-652.

Spalart, P. R. 1988 Direct simulation of a turbulent boundary layer up to $R_\theta = 1410$. *J. Fluid Mech.* **187**, 61-98.

Sreenivasan, K. R., 1989 The turbulent boundary layer. In *Frontiers in experimental fluid mechanics,* (ed. M. Gad-el-Hak), pp.159-205. New York: Springer Verlag.

Stone, E. 1991 A study of low dimensional models for the wall region of a turbulent boundary layer. Ph.D. thesis, Cornell University.

Stone, E. and Holmes, P. 1989 Noise induced intermittency in a model of a turbulent boundary layer. *Physica* **37D**, 20-32.

Temam, R. 1988 Indúced trajectories and approximate inertial manifolds. In *Proc. Luminy conf. on infinite dimensional dynamical systems, Marseille, France, 1987.*

Theodorsen, T. 1952 Mechanism of turbulence. In *Proc. 2nd Midwestern Conf. on Fluid Mech.* (Ohio State University, Colombus, Ohio, 1952).

Titi, E. S. 1988 On approximate inertial manifolds to the Navier-Stokes equations, MSI preprint 88-119, Cornell University, Ithaca, New York.

Townsend, A. A. 1956 *The structure of turbulent shear flow.* Cambridge: Univ. Press.

Wallace, J. M., Eckelmann, H. and Brodkey, R. S. 1972 The wall region in turbulent shear flow. *J. Fluid Mech.* **54**, 39-48.

Willmarth, W. W. & Lu, S. S. 1972 Structure of the Reynolds stress near the wall. *J. Fluid Mech.* **55**, 65-92.